MULTISCALE MODELING OF BRITTLE COMPOSITES USING REDUCED ORDER COMPUTATIONAL HOMOGENIZATION

By

Robert D. Crouch Jr.

Dissertation

Submitted to the Faculty of the

Graduate School of Vanderbilt University

in partial fulfillment of the requirements

for the degree of

DOCTOR OF PHILOSOPHY

in

Civil Engineering

August, 2012

Nashville, Tennessee

Approved:

Caglar Oskay

Prodyot Basu

Stephen Clay

Sankaran Mahadevan

Haoxiang Luo

For Dad, Mom, and Rachel

ACKNOWLEDGEMENTS

I would like to provide a special thanks to my advisor Dr. Caglar Oskay. We both have a love of engineering and mathematics which provides a desire to use math in solving challenging engineering problems. Without his advice and support, it would have been impossible to wind my way through the difficulties of this research.

Dr. Stephen Clay, my research sponsor at the Air Force Research Lab, also deserves thanks. Despite his background in experimental mechanics of materials, he was willing to put his faith in someone who preferred theory and who tried to avoid labs as much as possible. Spending my summers at ARFL under Steve's supervision has taught me a great deal about experimental techniques and gave me a practical perspective on the behavior of composite materials.

I would also like to acknowledge the remaining members of my Ph.D. committee Dr. Prodyot Basu, Dr. Sankaran Mahadevan, and Dr. Haoxiang Luo. I thank them for the knowledge they gave me in their courses and for the guidance and time they gave in serving on my committee. I would also like to thank all of the professors and teachers who provided my previous education. I would like to specifically mention Dr. Carroll Wells of the Lipscomb University mathematics department who convinced me that a double major in math and engineering was worth the effort and informed me that I was to get a Ph.D. before I had ever considered it.

Most importantly, I would like to thank my family and friends for their lifelong love and support. I have wonderful grandparents, in-laws, and friends who have done so much to encourage me during this process. Dad and Mom have supported me wholeheartedly in everything I have chosen to pursue only asking that I do my best.

They never attempted to direct or steer my life allowing me to choose my own path. This is such a precious and rare gift. I also thank my wife Rachel for her support and love. She is my best friend, and I cannot fathom life without her.

Finally, I acknowledge the financial support and experimental facilities provided by the Air Vehicles Directorate of the Air Force Research Laboratory (Contract No: F3446-09-46-SC01-01 through General Dynamics Information Technology Inc.).

TABLE OF CONTENTS

LIST OF TABLES

LIST OF FIGURES

CHAPTER 1

INTRODUCTION

1 Motivation

Little disagreement subsists that modeling failure in brittle composites is of great importance to fully realizing the potential gains such materials offer. Brittle composites, such as carbon fiber reinforced polymers, often possess beneficial properties including a high strength to weight ratio and high fatigue durability. These properties lend to the usage of composites in modern, high-performance structures. However, without a capability to model and predict failure, large factors of safety must be incorporated into designs preventing optimum utilization of these materials. This leads to a high demand for a failure modeling capability especially within the aerospace industry where performance gains are paramount.

The creation of a predictive failure model for composite structures presents several challenges. First, a wide variety of failure mechanisms can occur within the microstructure of a composite material. These include diffuse microcracking within the matrix, fiber/matrix debonding, delamination, fiber kinking, fiber buckling, and fiber fracture [56]. This multiplicity of failure mechanisms interact contributing to the ultimate global failure of a composite structure. Second, a size disparity exists between the size scale of constituent materials where failure initiates and grows and the total size of the composite structure. The small scale geometry of the intermingled constituent materials cannot be resolved for an entire composite structure as this would require excessive amounts of computer memory and computational power.

A predictive model for failure in composite structures must address each of these challenging aspects.

One of the main foci of this dissertation is predictive modeling of composite materials when subjected to fatigue loading. Composites are well-known to have high fatigue durability, but they do fail in fatigue [33]. As such, designers must account for fatigue failure which can be both sudden and catastrophic. A predictive model for fatigue failures may aid designers to realize the full performance potential offered by composites. Modeling fatigue failure in composites comes with an additional challenge. Much like the previously discussed spatial scale disparity, the duration of a single loading cycle is often significantly shorter than the total lifetime of a composite structure. If millions of loading cycles are required to induce global failure, explicitly modeling each cycle of loading would be computationally intractable. To model fatigue failure in composites, the computational modeling community must treat the temporal scale disparity alongside the other challenges of composite failure modeling mentioned above.

The field of multiscale modeling addresses each of the stated challenges including both the multiplicity of failure modes and the scale disparities in space and time. Multiscale modeling takes as its aim the development of methodologies that link phenomena occurring at different scales. The previously discussed scale disparity between a composite structure and the small scale interplay of the composite's constituents provides an example of a problem with multiple spatial scales. An effective multiscale method for modeling failure in composites should link the global structural response to the multiplicity of microscale composite failure mechanisms in a computationally tractable manner. If fatigue failure is considered, the scale disparity between a single loading cycle and the lifetime of a structure provides an example of a problem with multiple temporal scales. A tractable multiscale model for fatigue failure in composites must allow prediction of a composite structure's fatigue life without requiring the

resolution of millions of loading cycles. If such a multiscale approach can be developed, multiscale modeling provides a promising research path directly attacking the most difficult aspects of modeling failure in composites.

This dissertation presents a multiple spatial scale methodology and a multiple temporal scale methodology that address the problem of modeling failure in composites subjected monotonic and fatigue loadings. The spatial and temporal multiscale methodologies are designed to operate simultaneously, treating at once the multiple spatio-temporal scale problem. In addition, within the multiple spatial scale methodology, various failure modes can be naturally incorporated including fiber failure, fiber/matrix debonding, matrix cracking, and delamination. To obtain computational tractability, a spatial order reduction and an adaptive time stepping technique is devised. These reductions introduce some error, but high computational efficiency is gained while still maintaining the important features of the problem. These new multiscale methodologies attempt to directly address the challenges of modeling failure in brittle composites.

2 Research Objectives

The research objectives stated below are aligned to provide the basis for the development of a new multiscale tool useful for simulating fatigue in composites within aerospace applications. The primary research objectives for this dissertation are:

1. Devise reduced order spatial multiscale methodology for the simulation of failure in brittle composites undergoing monotonic loading.

2. Devise a temporal multiscale methodology for the simulation of failure in brittle composites undergoing fatigue loading.

3. Apply the new methodologies to modeling carbon fiber reinforced polymers undergoing both monotonic and fatigue loadings.

3 Dissertation Organization

The first research objective was addressed by the development of the symmetric reduced order homogenization methodology discussed in Chapter 2. This method is developed specifically to allow computationally efficient concurrent spatial multiscale modeling of brittle composite materials. In Chapter 2, the symmetric reduced order homogenization method is described and verified against direct numerical simulations of a heterogeneous particle reinforced material. The second research objective was accomplished by the development of a novel multiple spatio-temporal methodology that simultaneously accounts for the multiple spatial and temporal scales present in modeling damage accumulation and failure in composites. A derivation of this multiple spatio-temporal technique is described in Chapter 3 along with numerical and experimental validation of the approach. The final research objective was accomplished by initiating an extensive experimental and computational study of damage accumulation in carbon fiber reinforced polymer composites undergoing both monotonic and fatigue loadings. Advanced non-destructive experimental techniques such as acoustic emission testing, X-ray radiography, and X-ray computed tomography were used to great benefit in understanding damage accumulation in the CFRP materials. The modeling techniques presented in Chapter 2 and Chapter 3 were calibrated using independent experimentation and compared to the results from the experimental study. Chapter 4 provides an in depth description of the experimental program and the model results. Since each chapter contains related but separate topics, an introduction to each chapter provides a review of the relevant literature. Finally, Chapter 5 contains conclusions and future research.

CHAPTER 2

SYMMETRIC REDUCED ORDER COMPUTATIONAL HOMOGENIZATION

1 Introduction

Mathematical homogenization theory provides a rigorous mathematical framework for modeling the response of heterogeneous materials. The mathematical theory was formalized in the seminal works of Babuska [6], Bensoussan [10], Sanchez-Palencia [52] and Suquet [58], among others. Since the development of the computational framework for the mathematical homogenization theory by Guedes and Kikuchi [32], numerous models based on the computational homogenization method (CHM) have been proposed to predict the elastic and inelastic response of heterogeneous materials including material failure.

The distinct feature of the computational homogenization method in modeling the response of heterogeneous materials is in the evaluation of the constitutive response at a material point of a macroscopic (homogenized) medium. In CHM, the constitutive response of the equivalent homogeneous medium is evaluated by solving a microscale boundary value problem defined on a representative volume element (RVE) of the heterogeneous microstructure. This approach decouples the effect of the microstructural topology from the material behavior of the microconstituents, as well as the conditions along the microconstituent interfaces. CHM simplifies the constitutive modeling process since the response of the microconstituents tend to be *simpler* to model, compared to phenomenological modeling of the combined microstructure-material behavior effects. In the case of modeling the failure of heterogeneous mate-

rials, a number of outstanding computational issues remain, including selection of the boundary conditions for the RVE problem in the presence of defects [21, 63], evolution of the RVE domain upon defect formation, size scale effects [27], and spurious mesh dependency [9], among others.

One additional major challenge associated with the computational homogenization method is the computational cost associated with solving nonlinear RVE problems to evaluate the constitutive response of the macroscopic problem. This problem is alleviated by one or a combination of two approaches. The first is the brute-force parallelization of the multiscale problem, in which, the RVE problem evaluations are distributed to a large number of compute nodes and evaluated in parallel [20]. The second approach is reduced-order evaluation of the RVE problem. Fast Fourier transform [40], proper orthogonal decomposition [64], spectral method [1], boundary element method [30], network approximation method [11], and transformation field analysis (TFA) [7, 19], and other TFA-based computational methods [15, 25, 39] have been effective in evaluating the inelastic response at the RVE level in a computationally efficient manner. In a recent study, eigendeformation-based homogenization method (EHM) was proposed [46] to efficiently evaluate the RVE level response using a meso-mechanical model. This method is derived based on a generalization of the transformation field analysis. By this approach, it is possible to account for the interfacial debonding effects, in addition to nonlinear and failure processes within the constituent materials of the heterogeneous microstructure.

This chapter provides a model reduction methodology for efficient evaluation of the microscale boundary value problems of the computational homogenization method. The presented approach addresses three of the main shortcomings of the TFA-based model reduction methods with the the following novel contributions:

1. A new methodology for the determination of the order of the reduced model is presented: The accuracy and efficiency of the reduced models clearly depend on

their order and ability to represent the failure modes within the microstructure. A reduced-order model development strategy is devised to identify the model order and the associated coarse graining at the microscale for accurate and efficient representation of the failure modes.

2. The proposed reduced order model leads to a symmetric formulation: In the presence of interfacial debonding, previous eigendeformation-based homogenization formulations lack symmetry, which increases computational cost.

3. The proposed formulation eliminates the spurious residual stress effect upon failure due to the coarse representation of the inelastic fields. Some of the transformation field analysis based reduced order models (e.g., [25, 46]) lead to spurious residual stress fields upon failure in the microscale. The spurious residual stress fields pollute the macroscale problem by affecting local stress redistributions.

The proposed reduced order methodology is implemented to model the failure response of brittle composite systems, in which the failure is characterized by matrix microcracking, delamination and debonding.

The remainder of this chapter is organized as follows: The statement of the multiscale problem and the associated macroscopic and microscopic boundary value problems are presented in Section 2. In Section 3, formulation of the symmetric reduced order model for the microscale problem is provided. The computational algorithms employed to evaluate the nonlinear reduced order model are discussed in Section 4. Section 5 provides small scale and large scale numerical verification examples conducted on a fiber reinforced matrix composite.

2 Problem Setting

In this section, we present a summary of the microscopic and macroscopic boundary value problems associated with the two-scale asymptotic homogenization method for failure response of a heterogeneous body. The details of two-scale asymptotic homogenization in the presence of inelastic effects are reported in the literature (see e.g., Refs. [62]).

The problem setting and the multiscale heterogeneous body is illustrated in Fig. 1. The heterogeneous domain, denoted by Ω, is parameterized by the macroscopic coordinate vector, $\mathbf{x}$. Ω is composed of the repetition of a small representative volume element, Θ, which is parameterized by the microscopic coordinate vector, $\mathbf{y}$. The size scale ratio, ζ, between the characteristic lengths of the representative volume element, Θ, and the macroscopic body, Ω is assumed to be very small, such that a first order asymptotic decomposition of the displacement field is sufficient to accurately capture the response of the material. The response fields are assumed to be periodic about the representative volume element. The periodicity condition states that the value of the response fields are the same at the opposing faces of a parallelepiped RVE domain.

The following notation is employed throughout the chapter, unless otherwise noted: Subscript roman indices denote 1, 2, or 3. Einstein summation convention is adopted for repeated indices. Subscripts x_i and y_i following a comma denote differentiation with respect to the macroscopic and microscopic coordinate vectors, respectively. Differentiation within parentheses denotes symmetric differentiation with respect to the indices. Bold characters denote tensor notation. Macaulay brackets denote averaging over the RVE:

$$\langle \cdot \rangle = \frac{1}{|\Theta|} \int_{\Theta} (\cdot) d\mathbf{y} \tag{1}$$

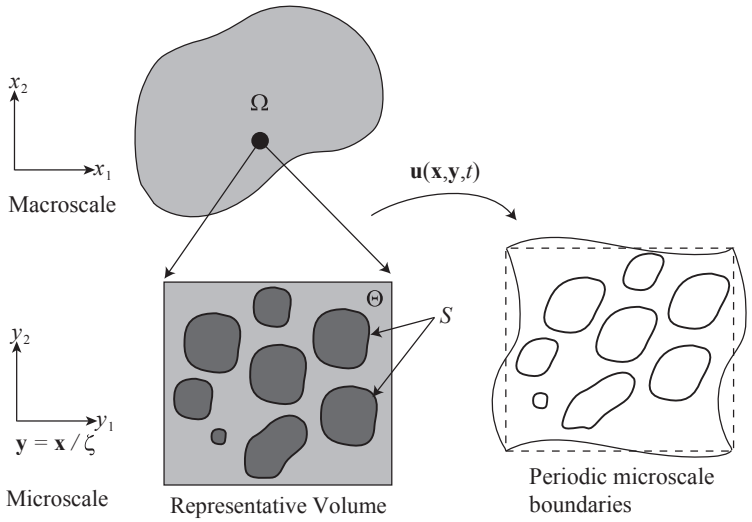

Figure 1: Macro- and microscopic scales.

where, $|\Theta|$ is the volume of the RVE.

The displacement field of the heterogeneous body is expressed using a two-scale asymptotic expansion:

$$u_i\left(\mathbf{x},\mathbf{y},t\right)=\bar{u}_i\left(\mathbf{x},t\right)+\zeta u_i^1\left(\mathbf{x},\mathbf{y},t\right) \tag{2}$$

in which, $\bar{\mathbf{u}}$ is the macroscopic displacement field, and; $\mathbf{u}^1$ is the variation of the displacement field within the RVE.

2.1 Microscale Problem

In the presence of failure processes, $\mathbf{u}^1$ is described by the microscopic equilibrium equation defined over the RVE (i.e., $\mathbf{y}\in\Theta$)

$$\left\{L_{ijkl}\left(\mathbf{y}\right)\left[\bar{\epsilon}_{kl}\left(\mathbf{x},t\right)+u^1_{(k,y_l)}\left(\mathbf{x},\mathbf{y},t\right)-\mu_{kl}\left(\mathbf{x},\mathbf{y},t\right)\right]\right\}_{,y_j}=0 \tag{3}$$

in which, $\mathbf{L}$ is the fourth order tensor of elastic moduli, taken to be symmetric and strongly elliptic, $\bar{\boldsymbol{\epsilon}}=\nabla^s_{\mathbf{x}}\bar{\mathbf{u}}$ the macroscopic strain tensor; $\nabla^s_{\mathbf{x}}(\cdot)\equiv(\cdot)_{(i,x_j)}$ denotes the symmetric gradient operation with respect to macroscopic coordinates; and $\boldsymbol{\mu}$

damage induced inelastic strains. In this work, the damage induced inelastic strains are modeled using a scalar continuous damage mechanics model:

$$\mu_{ij}\left(\mathbf{x},\mathbf{y},t\right)=\omega_{\text{ph}}\left(\mathbf{x},\mathbf{y},t\right)\epsilon_{ij}\left(\mathbf{x},\mathbf{y},t\right) \tag{4}$$

in which, $\omega_{\text{ph}}\in[0,1)$ is a history dependent variable, which represents damage within the microconstituents, and $\boldsymbol{\epsilon}$ is the strain tensor. Using the scaling relations provided by the asymptotic decompositions with multiple spatial scales:

$$\epsilon_{ij}\left(\mathbf{x},\mathbf{y},t\right)=\bar{\epsilon}_{ij}\left(\mathbf{x},t\right)+u^{1}_{(i,y_j)}\left(\mathbf{x},\mathbf{y},t\right) \tag{5}$$

Along the microconstituent interfaces, debonding is considered based on traction-separation laws given as ($\mathbf{y}\in S$)

$$t^{N}\left(\mathbf{x},\mathbf{y},t\right)-\left[1-\omega_{\text{int}}\left(\mathbf{x},\mathbf{y},t\right)\right]k^{N}\left(\mathbf{y}\right)\delta^{N}\left(\mathbf{x},\mathbf{y},t\right)\leq 0;\quad \delta^{N}\left(\mathbf{x},\mathbf{y},t\right)\geq 0 \tag{6}$$

$$\left\{t^{N}\left(\mathbf{x},\mathbf{y},t\right)-\left[1-\omega_{\text{int}}\left(\mathbf{x},\mathbf{y},t\right)\right]k^{N}\left(\mathbf{y}\right)\delta^{N}\left(\mathbf{x},\mathbf{y},t\right)\right\}\delta^{N}\left(\mathbf{x},\mathbf{y},t\right)=0 \tag{7}$$

$$\mathbf{t}^{T}\left(\mathbf{x},\mathbf{y},t\right)=\left[1-\omega_{\text{int}}\left(\mathbf{x},\mathbf{y},t\right)\right]k^{T}\left(\mathbf{y}\right)\boldsymbol{\delta}^{T}\left(\mathbf{x},\mathbf{y},t\right) \tag{8}$$

in which, $\omega_{\text{int}}\in[0,1)$ is a history dependent variable, which represents damage along the interface; t^N and δ^N are the components of the traction and displacement jump normal to the interface, respectively; $k^{N}\left(\mathbf{y}\right)$ and $k^{T}\left(\mathbf{y}\right)$ the initial interface stiffness in the normal and tangential directions, respectively, and; $\mathbf{t}^T$, $\boldsymbol{\delta}^T$ the tangential components of the traction and displacement jump along the interface, respectively. The traction and displacement jump components are expressed in terms of the local coordinate system formed by the normal and tangential directions at the interface point.

The microscale problem, which is a nonlinear boundary value problem is solved to evaluate the microscale displacement field $\mathbf{u}^1$ by imposing periodic boundary con-

ditions along the exterior boundaries of the RVE while restricting the rigid body motion. The microscale boundary value problem is quasi-static as indicated by the lack of inertial terms in the governing equations. The present formulation is limited to the cases for which the characteristic size of the RVE is small compared to the length of the deformation and stress waves.

2.2 Macroscale Problem

The macroscopic displacement field is described by the macroscopic momentum balance equation defined over Ω:

$$\bar{\sigma}_{ij,x_j}(\mathbf{x},t) + \bar{b}_i(\mathbf{x},t) = \bar{\rho}(\mathbf{x},t)\,\ddot{\bar{u}}_i(\mathbf{x},t) \tag{9}$$

in which, double dot over a field denotes twice differentiation in time; $\bar{\boldsymbol{\sigma}}$ denotes the macroscopic stress tensor, evaluated by volume averaging of the stresses over the domain of the RVE

$$\bar{\sigma}_{ij}(\mathbf{x},t) = \langle \sigma_{ij} \rangle \tag{10}$$

The stress field is expressed as:

$$\sigma_{ij}(\mathbf{x},\mathbf{y},t) = L_{ijkl}(\mathbf{y})\left[\bar{\epsilon}_{kl}(\mathbf{x},t) + u^1_{(k,y_l)}(\mathbf{x},\mathbf{y},t) - \mu_{kl}(\mathbf{x},\mathbf{y},t)\right] \tag{11}$$

$\bar{\mathbf{b}}$ and $\bar{\rho}$ denote the RVE-average body force/unit volume and the RVE-average density, respectively:

$$\bar{b}_i(\mathbf{x},t) = \langle b_i \rangle\,; \quad \bar{\rho} = \langle \rho \rangle \tag{12}$$

The boundary and initial conditions of the macroscale initial-boundary value prob-

lem are defined as

$$\bar{u}_i(\mathbf{x},t) = \hat{u}_i(\mathbf{x}); \quad \mathbf{x}\in\Omega; \quad t=0 \tag{13}$$

$$\dot{\bar{u}}_i(\mathbf{x},t) = \hat{v}_i(\mathbf{x}); \quad \mathbf{x}\in\Omega; \quad t=0 \tag{14}$$

$$\bar{u}_i(\mathbf{x},t) = \breve{u}_i(\mathbf{x},t); \quad \mathbf{x}\in\Gamma_u; \quad t\in[0,t_{\mathrm{o}}] \tag{15}$$

$$\bar{\sigma}_{ij}(\mathbf{x},t)\,n_j = \breve{t}_i(\mathbf{x},t); \quad \mathbf{x}\in\Gamma_t; \quad t\in[0,t_{\mathrm{o}}] \tag{16}$$

in which, $\hat{\mathbf{u}}$, $\breve{\mathbf{u}}$ are prescribed initial and boundary displacements, respectively; $\hat{\mathbf{v}}$ prescribed initial velocity, and; $\breve{\mathbf{t}}$ prescribed boundary traction. The prescribed initial and boundary conditions are assumed to be constant with respect to the microscopic coordinate vector $\mathbf{y}$.

3 Reduced Order Modeling of the Microscale Problem

The macroscale problem defined in Section 2.2 is coupled with the microscale problem defined in Section 2.1 through the macroscopic constitutive relationship (Eqs. 10 and 11). The evaluation of the macroscopic stress at each macroscopic material point requires the solution of the microscopic RVE problem associated with that material point. When the finite element method is employed to evaluate the macroscale problem, a nonlinear microscale problem must be evaluated to update the stress at each integration point for each increment and iteration of every time step of the loading history. This is a tremendous computational burden. In this section, a novel reduced order model is derived to efficiently compute the microscopic response. To this extent, the microscale displacement field is decomposed into linear and damage induced components:

$$u_i^1(\mathbf{x},\mathbf{y},t) = H_{ikl}(\mathbf{y})\,\bar{\epsilon}_{kl}(\mathbf{x},t) + \tilde{u}_i(\mathbf{x},\mathbf{y},t) \tag{17}$$

in which, $\mathbf{H}$ is the third order elastic influence function obtained by substituting Eq. 17 into Eq. 3 and solving the microscale problem in the absence of all inelastic processes (i.e., $\omega_{\text{ph}} = \omega_{\text{int}} = 0$). $\tilde{\mathbf{u}}$ is the displacement field induced by the damage processes within the microconstituents and the interface:

$$\tilde{u}_i(\mathbf{x}, \mathbf{y}, t) = \int_{\Theta} h^{\text{ph}}_{ikl}(\mathbf{y}, \hat{\mathbf{y}})\, \mu_{kl}(\mathbf{x}, \hat{\mathbf{y}}, t)\, d\hat{\mathbf{y}} + \int_{S} h^{\text{int}}_{im}(\mathbf{y}, \hat{\mathbf{y}})\, \delta_m(\mathbf{x}, \hat{\mathbf{y}}, t)\, d\hat{\mathbf{y}} \tag{18}$$

in which $\mathbf{h}^{\text{ph}}$ and $\mathbf{h}^{\text{int}}$ are the phase damage and interface damage induced influence functions. $\mathbf{h}^{\text{ph}}$ and $\mathbf{h}^{\text{int}}$ are the particular solutions to the RVE problems obtained by substituting Eq. 17 into Eq. 3 and solving the microscale problem in the presence of phase damage (i.e., $\boldsymbol{\mu}$) and interface damage (i.e., $\boldsymbol{\delta}$), respectively. The governing equations and the discrete approximations of the elastic and damage induced influence functions are provided in Ref. [46] and will not be discussed herein. In this section, we concentrate on the new model reduction methodology based on the microscopic displacement field decomposition provided in Eqs. 17 and 18.

Substituting Eq. 17 into Eq. 3, premultiplying the resulting equation with $\mathbf{h}^{\text{ph}}$, and integrating over the domain of the RVE yields:

$$\int_{\Theta} h^{\text{ph}}_{ipq}(\mathbf{y}, \hat{\mathbf{y}}) \left\{ L_{ijmn}(\mathbf{y}) \left[A_{mnkl}(\mathbf{y})\, \bar{\epsilon}_{kl}(\mathbf{x}, t) + \tilde{\epsilon}_{mn}(\mathbf{x}, \mathbf{y}, t) - \mu_{mn}(\mathbf{x}, \mathbf{y}, t) \right] \right\}_{,y_j} d\mathbf{y} = 0 \tag{19}$$

in which, $\tilde{\boldsymbol{\epsilon}} = \nabla^s_{\mathbf{y}} \tilde{\mathbf{u}}$; $\mathbf{A} = \mathbf{I} + \mathbf{G}$ is the fourth order elastic strain concentration tensor; $\mathbf{I}$ the fourth order identity tensor, and; $\mathbf{G} = \nabla^s_{\mathbf{y}} \mathbf{H}$, the elastic polarization tensor. The use of Eq. 19 secures a symmetric formulation as subsequently derived. This is in contrast with the previous eigendeformation-based reduced order models, which are non-symmetric [46]. Integrating by parts, applying divergence theorem and employing the perodicity of the response fields over the domain of the RVE yields:

$$\int_{\Theta} g^{\text{ph}}_{ijpq}(\mathbf{y}, \hat{\mathbf{y}})\, L_{ijmn}(\mathbf{y}) \left[A_{mnkl}(\mathbf{y})\, \bar{\epsilon}_{kl}(\mathbf{x}, t) + \tilde{\epsilon}_{mn}(\mathbf{x}, \mathbf{y}, t) - \mu_{mn}(\mathbf{x}, \mathbf{y}, t) \right] d\mathbf{y} = 0 \tag{20}$$

where, $\mathbf{g}^{\text{ph}} = \nabla^s_{\mathbf{y}} \mathbf{h}^{\text{ph}}$ is the fourth order phase damage polarization tensor.

A second set of equilibrium equations are obtained by premultiplying the microscale equilibrium equation (Eq. 3) with $\mathbf{h}^{\text{int}}$, and following a similar procedure as described above:

$$\int_{\Theta} g^{\text{int}}_{ijp}(\mathbf{y}, \hat{\mathbf{y}})\, L_{ijmn}(\mathbf{y}) \left[A_{mnkl}(\mathbf{y})\, \bar{\epsilon}_{kl}(\mathbf{x}, t) + \tilde{\epsilon}_{mn}(\mathbf{x}, \mathbf{y}, t) - \mu_{mn}(\mathbf{x}, \mathbf{y}, t)\right] d\mathbf{y} = -t_p(\mathbf{x}, \hat{\mathbf{y}}, t) \tag{21}$$

in which, $\mathbf{g}^{\text{int}} = \nabla^s_{\mathbf{y}} \mathbf{h}^{\text{int}}$ is the third order interface damage polarization tensor. Substituting Eq. 4 into Eqs. 20 and 21 yields:

$$\int_{\Theta} \Big[1 - \omega_{\text{ph}}(\mathbf{x}, \mathbf{y}, t)\Big]\, g^{\text{ph}}_{ijqr}(\mathbf{y}, \hat{\mathbf{y}})\, L_{ijmn}(\mathbf{y}) \cdot \cdot \Big[A_{mnkl}(\mathbf{y})\, \bar{\epsilon}_{kl}(\mathbf{x}, t) + \tilde{\epsilon}_{mn}(\mathbf{x}, \mathbf{y}, t)\Big]\, d\mathbf{y} = 0 \tag{22}$$

$$\int_{\Theta} \Big[1 - \omega_{\text{ph}}(\mathbf{x}, \mathbf{y}, t)\Big]\, g^{\text{int}}_{ijp}(\mathbf{y}, \hat{\mathbf{y}})\, L_{ijmn}(\mathbf{y}) \cdot \cdot \Big[A_{mnkl}(\mathbf{y})\, \bar{\epsilon}_{kl}(\mathbf{x}, t) + \tilde{\epsilon}_{mn}(\mathbf{x}, \mathbf{y}, t)\Big] d\mathbf{y} = -t_p(\mathbf{x}, \hat{\mathbf{y}}, t) \tag{23}$$

We introduce the following discretizations for damage fields ω_{ph} and ω_{int}, and the damage induced fields, $\boldsymbol{\mu}$ and $\boldsymbol{\delta}$ using mesomechanical shape functions

$$\{\omega_{\text{ph}}, \mu_{ij}\}(\mathbf{x}, \mathbf{y}, t) = \sum_{\gamma=1}^{n} N^{(\gamma)}_{\text{ph}}(\mathbf{y}) \left\{\omega^{(\gamma)}_{\text{ph}}, \mu^{(\gamma)}_{ij}\right\}(\mathbf{x}, t) \tag{24}$$

$$\left\{\omega_{\text{int}}, \hat{\delta}_i\right\}(\mathbf{x}, \mathbf{y}, t) = \sum_{\beta=1}^{m} N^{(\beta)}_{\text{int}}(\mathbf{y}) \left\{\omega^{(\beta)}_{\text{int}}, \hat{\delta}^{(\beta)}_i\right\}(\mathbf{x}, t) \tag{25}$$

in which, $\gamma = 1, 2, \ldots, n$ and $\beta = 1, 2, \ldots, m$; n and m denote the level of discretization within the phases and along the interface, respectively. $\hat{\boldsymbol{\delta}}$ denotes the displacement jump vector in the local coordinate system (i.e., $\hat{\delta}^{(\beta)} = \left[\delta^{N(\beta)}\, \boldsymbol{\delta}^{T(\beta)}\right]^T$). The phase, $N^{(\gamma)}_{\text{ph}}$, and interface, $N^{(\beta)}_{\text{int}}$, shape functions have compact support within

subdomains of the phases and the interface

$$N_{\text{ph}}^{(\gamma)}(\mathbf{y}) = 0 \text{ if } \mathbf{y} \notin \Theta^{(\gamma)}; \quad \Theta^{(\gamma)} \subset \Theta \tag{26}$$

$$N_{\text{int}}^{(\beta)}(\mathbf{y}) = 0 \text{ if } \mathbf{y} \notin S^{(\beta)}; \quad S^{(\beta)} \subset S \tag{27}$$

Employing Eqs. 24 and 25, $\tilde{\boldsymbol{\epsilon}}$ is expressed in terms of the damage induced strain and displacement jump coefficients:

$$\tilde{\epsilon}_{ij}(\mathbf{x}, \mathbf{y}, t) = \sum_{\gamma} \tilde{P}_{ijkl}^{(\gamma)}(\mathbf{y}) \, \mu_{kl}^{(\gamma)}(\mathbf{x}, t) + \sum_{\beta} \tilde{R}_{ijp}^{(\beta)}(\mathbf{y}) \, \hat{\delta}_{p}^{(\beta)}(\mathbf{x}, t) \tag{28}$$

in which, the coefficient tensors $\tilde{\mathbf{P}}$ and $\tilde{\mathbf{R}}$ are:

$$\tilde{P}_{ijkl}^{(\gamma)}(\mathbf{y}) = \int_{\Theta^{(\gamma)}} g_{ijkl}^{\text{ph}}(\mathbf{y}, \check{\mathbf{y}}) \, N_{\text{ph}}^{(\gamma)}(\check{\mathbf{y}}) \, d\check{\mathbf{y}} \tag{29}$$

$$\tilde{R}_{ijp}^{(\beta)}(\mathbf{y}) = \int_{S^{(\beta)}} g_{ijq}^{\text{int}}(\mathbf{y}, \check{\mathbf{y}}) \, N_{\text{int}}^{(\beta)}(\check{\mathbf{y}}) \, \hat{\mathbf{e}}_q(\check{\mathbf{y}}) \, d\check{\mathbf{y}} \tag{30}$$

where $\hat{\mathbf{e}}_q$ denotes the transformation vector between the global and local coordinate systems along the interface.

Substituting Eqs. 24 and 25 into Eq. 22, premultiplying the resulting equation with $N_{\text{ph}}^{(\eta)}(\hat{\mathbf{y}})$, and integrating over the domain of the RVE yields ($\eta = 1, 2, \ldots, n$):

$$\sum_{\Delta=1}^{n} \left\{ \left[1 - \omega_{\text{ph}}^{(\Delta)}(\mathbf{x}, t)\right] \int_{\Theta^{(\Delta)}} N_{\text{ph}}^{(\Delta)}(\mathbf{y}) \, \tilde{P}_{ijqr}^{(\eta)}(\mathbf{y}) \, L_{ijmn}(\mathbf{y}) \right.$$
$$\left. [A_{mnkl}(\mathbf{y}) \, \bar{\epsilon}_{kl}(\mathbf{x}, t) + \tilde{\epsilon}_{mn}(\mathbf{x}, \mathbf{y}, t)] d\mathbf{y} \right\} = 0 \tag{31}$$

Similarly, substituting Eqs. 24 and 25 into Eq. 23, premultiplying the resulting equation with $N_{\text{int}}^{(\alpha)}(\hat{\mathbf{y}})$ and integrating over the domain of the RVE yields ($\alpha =$

$1, 2, \ldots, m$):

$$\sum_{\Delta=1}^{n} \left\{ \left[1 - \omega_{\mathrm{ph}}^{(\Delta)}(\mathbf{x}, t)\right] \int_{\Theta^{(\Delta)}} N_{\mathrm{ph}}^{(\Delta)}(\mathbf{y})\, \tilde{R}_{ijp}^{(\alpha)}(\mathbf{y})\, L_{ijmn}(\mathbf{y}) \right.$$
$$\left. \left[A_{mnkl}(\mathbf{y})\, \bar{\epsilon}_{kl}(\mathbf{x}, t) + \tilde{\epsilon}_{mn}(\mathbf{x}, \mathbf{y}, t)\right] d\mathbf{y} \right\} = -\hat{t}_p^{(\alpha)}(\mathbf{x}, t) \tag{32}$$

Substituting Eq. 28 into Eqs. 31 and 32 results in

$$\sum_{\Delta=1}^{n} \left\{ \left[1 - \omega_{\mathrm{ph}}^{(\Delta)}(\mathbf{x}, t)\right] \left[C_{ijkl}^{(\eta\Delta)} \bar{\epsilon}_{kl}(\mathbf{x}, t) + \sum_{\gamma=1}^{n} F_{ijkl}^{(\eta\Delta\gamma)} \mu_{kl}^{(\gamma)}(\mathbf{x}, t) \right.\right.$$
$$\left.\left. + \sum_{\beta=1}^{m} J_{ijp}^{(\eta\Delta\beta)} \hat{\delta}_p^{(\beta)}(\mathbf{x}, t) \right] \right\} = 0 \tag{33}$$

$$\sum_{\Delta} \left\{ \left[1 - \omega_{\mathrm{ph}}^{(\Delta)}(\mathbf{x}, t)\right] \left[D_{pkl}^{(\alpha\Delta)} \bar{\epsilon}_{kl}(\mathbf{x}, t) + \sum_{\gamma=1}^{n} J_{klp}^{(\gamma\Delta\alpha)} \mu_{kl}^{(\gamma)}(\mathbf{x}, t) \right.\right.$$
$$\left.\left. + \sum_{\beta=1}^{m} M_{pq}^{(\alpha\Delta\beta)} \hat{\delta}_p^{(\beta)}(\mathbf{x}, t) \right] \right\} = -\hat{t}_p^{(\alpha)}(\mathbf{x}, t) \tag{34}$$

where,

$$C_{ijkl}^{(\eta\Delta)} = \int_{\Theta^{(\Delta)}} \tilde{P}_{qrij}^{(\eta)}(\mathbf{y})\, L_{qrmn}(\mathbf{y})\, A_{mnkl}(\mathbf{y})\, N_{\mathrm{ph}}^{(\Delta)}(\mathbf{y})\, d\mathbf{y} \tag{35}$$

$$D_{pkl}^{(\alpha\Delta)} = \int_{\Theta^{(\Delta)}} \tilde{R}_{ijp}^{(\alpha)}(\mathbf{y})\, L_{ijmn}(\mathbf{y})\, A_{mnkl}(\mathbf{y})\, N_{\mathrm{ph}}^{(\Delta)}(\mathbf{y})\, d\mathbf{y} \tag{36}$$

$$F_{ijkl}^{(\eta\Delta\gamma)} = \int_{\Theta^{(\Delta)}} \tilde{P}_{qrij}^{(\eta)}(\mathbf{y})\, L_{qrmn}(\mathbf{y})\, \tilde{P}_{mnkl}^{(\gamma)}(\mathbf{y})\, N_{\mathrm{ph}}^{(\Delta)}(\mathbf{y})\, d\mathbf{y} \tag{37}$$

$$J_{ijp}^{(\eta\Delta\beta)} = \int_{\Theta^{(\Delta)}} \tilde{P}_{qrij}^{(\eta)}(\mathbf{y})\, L_{qrmn}(\mathbf{y})\, \tilde{R}_{mnp}^{(\beta)}(\mathbf{y})\, N_{\mathrm{ph}}^{(\Delta)}(\mathbf{y})\, d\mathbf{y} \tag{38}$$

$$M_{pq}^{(\alpha\Delta\beta)} = \int_{\Theta^{(\Delta)}} \tilde{R}_{ijp}^{(\alpha)}(\mathbf{y})\, L_{ijmn}(\mathbf{y})\, \tilde{R}_{mnq}^{(\beta)}(\mathbf{y})\, N_{\mathrm{ph}}^{(\Delta)}(\mathbf{y})\, d\mathbf{y} \tag{39}$$

in which, $\mathbf{C}^{(\eta\Delta)}$, $\mathbf{D}^{(\alpha\Delta)}$, $\mathbf{F}^{(\eta\Delta\gamma)}$, $\mathbf{J}^{(\eta\Delta\beta)}$ and $\mathbf{M}^{(\alpha\Delta\beta)}$ are coefficient tensors. The inter-

face traction coefficient, $\hat{\mathbf{t}}^{(\alpha)}$ is:

$$\hat{t}_i^{(\alpha)}(\mathbf{x},t) = \int_{S^{(\alpha)}} N_{\text{int}}^{(\alpha)}(\mathbf{y})\,\hat{t}_i(\mathbf{x},\mathbf{y},t)\,d\mathbf{y} \tag{40}$$

The relationship between the interface traction and the displacement jump is nonlinear. It is, therefore, not possible to derive explicit expressions for the relationship between the traction and displacement jump coefficients. In this section, the relationship between the pointwise tractions and displacement jumps are adopted to represent the relationship between the traction and displacement jump coefficients. This approach has also been employed in a number of previous investigations (e.g., [39]). The unilateral contact and adhesion conditions are expressed as

$$\delta^{N(\alpha)}(\mathbf{x},t) \geq 0 \tag{41}$$

$$t^{N(\alpha)}(\mathbf{x},t) - \left[1-\omega_{\text{int}}^{(\alpha)}(\mathbf{x},t)\right] k_N^{(\alpha)} \delta^{N(\alpha)}(\mathbf{x},t) \leq 0 \tag{42}$$

$$\left\{t^{N(\alpha)}(\mathbf{x},t) - \left[1-\omega_{\text{int}}^{(\alpha)}(\mathbf{x},t)\right] k_N^{(\alpha)} \delta^{N(\alpha)}(\mathbf{x},t)\right\} \delta^{N(\alpha)}(\mathbf{x},t) = 0 \tag{43}$$

The tangential adhesion condition is also written in a similar form as

$$t_\rho^{T(\alpha)}(\mathbf{x},t) - \left[1-\omega_{\text{int}}^{(\alpha)}(\mathbf{x},t)\right] k_T^{(\alpha)} \delta_\rho^{T(\alpha)}(\mathbf{x},t) = 0 \tag{44}$$

Similar to the interface traction-separation conditions, the nonlinear evolution of the phase and interface damage coefficients, $\omega_{\text{ph}}^{(\gamma)}$ and $\omega_{\text{int}}^{(\alpha)}$, are expressed in terms of the field coefficients:

$$\omega_{\text{ph}} = \omega_{\text{ph}}(\sigma_{ij},\epsilon_{ij},q_a) \rightarrow \omega_{\text{ph}}^{(\gamma)} = \omega_{\text{ph}}^{(\gamma)}\left(\sigma_{ij}^{(\gamma)},\epsilon_{ij}^{(\gamma)},q_a^{(\gamma)}\right) \tag{45}$$

$$\omega_{\text{int}} = \omega_{\text{int}}\left(t_i,\delta_i,q_a^{\text{int}}\right) \rightarrow \omega_{\text{int}}^{(\alpha)} = \omega_{\text{int}}^{(\alpha)}\left(t_i^{(\alpha)},\delta_i^{(\alpha)},q_a^{\text{int}(\alpha)}\right) \tag{46}$$

in which, $\mathbf{q}$ and $\mathbf{q}^{\text{int}}$ are state variables defining the evolution of the phase and interface damage variables, respectively, and;

$$[\cdot]^{(\gamma)}(\mathbf{x},t)=\int_{\Theta^{(\gamma)}} N_{\text{ph}}^{(\gamma)}(\mathbf{y})\,[\cdot](\mathbf{x},\mathbf{y},t)\,d\mathbf{y};\quad [\cdot]^{(\alpha)}(\mathbf{x},t)=\int_{S^{(\alpha)}} N_{\text{int}}^{(\alpha)}(\mathbf{y})\,[\cdot](\mathbf{x},\mathbf{y},t)\,d\mathbf{y} \tag{47}$$

Equilibrium equations (Eqs. 33 and 34), in addition to the interface conditions provided by Eqs 41-44, and the evolution equations for the phase and interface damage coefficients form the reduced order model. The reduced order model is solved to obtain the unknown coefficients $\boldsymbol{\mu}^{(\gamma)}$ and $\hat{\boldsymbol{\delta}}^{(\alpha)}$.

The macroscopic stress tensor is expressed in terms of $\boldsymbol{\mu}^{(\gamma)}$, $\hat{\boldsymbol{\delta}}^{(\alpha)}$, and the macroscopic strain tensor by substituting Eq. 17 and 18 into Eq. 11 and using Eqs. 24 and 25 to obtain

$$\bar{\sigma}_{ij}(\mathbf{x},t)=\sum_{\Delta}\Big[1-\omega_{\text{ph}}^{(\Delta)}(\mathbf{x},t)\Big]\Big[\bar{L}_{ijkl}^{(\Delta)}\bar{\epsilon}_{kl}(\mathbf{x},t)+\sum_{\gamma}\bar{P}_{ijkl}^{(\Delta\gamma)}\mu_{kl}^{(\gamma)}(\mathbf{x},t)+\sum_{\beta}\bar{R}_{ijp}^{(\Delta\beta)}\hat{\delta}_{p}^{(\beta)}(\mathbf{x},t)\Big] \tag{48}$$

where, the coefficient tensors $\bar{\mathbf{L}}^{(\Delta)}$, $\bar{\mathbf{P}}^{(\Delta\gamma)}$ and $\bar{\mathbf{R}}^{(\Delta\beta)}$ are expressed as

$$\bar{L}_{ijkl}^{(\Delta)} = \frac{1}{\mid\Theta\mid}\int_{\Theta^{(\Delta)}} N_{\text{ph}}^{(\Delta)}(\mathbf{y})\,L_{ijmn}(\mathbf{y})\,A_{mnkl}(\mathbf{y})\,d\mathbf{y} \tag{49}$$

$$\bar{P}_{ijkl}^{(\Delta\gamma)} = \frac{1}{\mid\Theta\mid}\int_{\Theta^{(\Delta)}} N_{\text{ph}}^{(\Delta)}(\mathbf{y})\,L_{ijmn}(\mathbf{y})\,\tilde{P}_{mnkl}^{(\gamma)}(\mathbf{y})\,d\mathbf{y} \tag{50}$$

$$\bar{R}_{ijp}^{(\Delta\beta)} = \frac{1}{\mid\Theta\mid}\int_{\Theta^{(\Delta)}} N_{\text{ph}}^{(\Delta)}(\mathbf{y})\,L_{ijmn}(\mathbf{y})\,\tilde{R}_{mnp}^{(\beta)}(\mathbf{y})\,d\mathbf{y} \tag{51}$$

4 Computational Aspects

The implementation of the proposed reduced-order multiscale model is conducted in two stages. The *preprocessing* stage consists of determining the model order, partitioning of the RVE based upon the model order, and computing the coefficient tensors associated with the reduced order model. The *macroscopic analysis* stage consists of

evaluating the macroscale problem described in Section 2.2 using a numerical method. In this study, the macroscopic analyses are conducted using the finite element method. The commercially available finite element analysis program, Abaqus, is employed. Reduced order multiscale models and direct numerical simulations for the verification of the proposed approach are conducted using the user supplied subroutine capabilities. The remainder of this section discusses a novel strategy for selection of the model order and partitioning of the RVE domain, as well as the numerical evaluation of the reduced order model.

4.1 Reduced-Order Model Development Strategy

The proper partitioning of the RVE domain is critical to the efficiency and the accuracy of the proposed reduced order modeling approach. The partitioning of the RVE consists of the selection of the number of phase (n) and interface (m) partitions, as well as the domain of each phase ($\Theta^{(\gamma)}$) and interface ($S^{(\beta)}$) partition. Theoretically, as the number of partitions, n and m, increase, the accuracy of the reduced model increases at the expense of additional computational cost. The accuracy of the reduced order model is also strongly affected by the selection of the partition domains, $\Theta^{(\gamma)}$ and $S^{(\beta)}$ for a given number of phase and interface partitions. Previous and current investigations found significant variability in the performance of a reduced order model based on the partitioning strategy. It is possible to adaptively select the order of the reduced-order model based on a-priori error measures associated with the state of the failure processes during the macroscopic simulations. Such a dynamic partitioning strategy was proposed in Ref. [46]. The dynamic strategy resembles h-version adaptive finite element modeling with goal oriented mesh adaptivity [43], or multilevel-multiscale modeling, in which the heterogeneity within the process zones are adaptively resolved [28]. The dynamic partitioning strategy, while rigorous, comes with a significant increase in computational cost. The additional computational cost

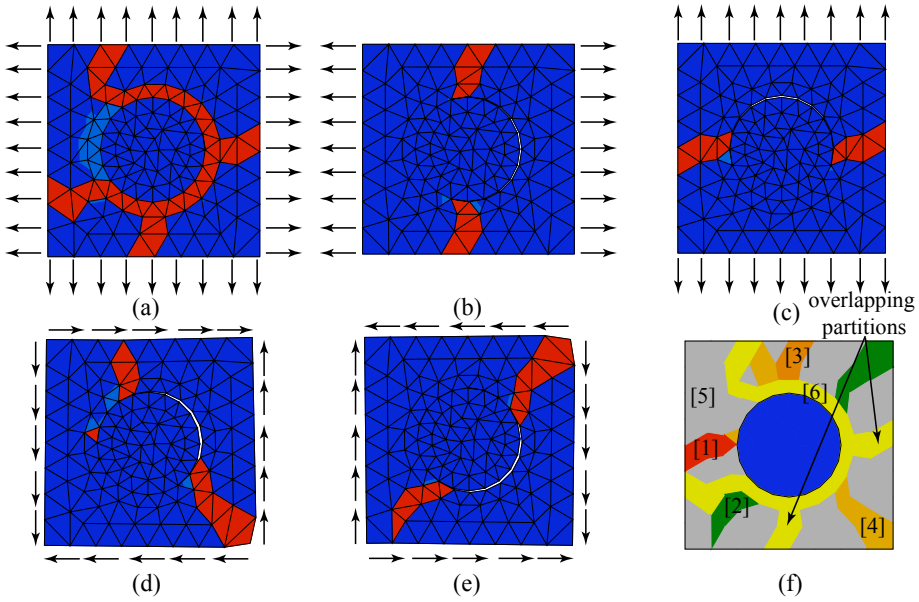

Figure 2: The partitioning and model reduction strategy. Failure profiles within the RVE subjected to (a) uniform biaxial loading; (b) uniaxial in the lateral direction; (c) uniaxial loading in the vertical direction; (d) shear loading along the positive direction; (e) shear loading along the negative direction; (f) resultant partitions.

is due to error assessment and recomputation of the coefficient tensors during the macroscopic analysis.

In this section, a novel static partitioning strategy is presented, in which, the RVE domain partitions and the model order is identified prior to the macroscopic analysis. The present approach provides a model selection strategy capable of accounting for the failure modes within the microstructure using a small number of domain partitions. The model selection strategy consists of identification of the failure paths within the microstructure when subjected to a number of loading modes, and partitioning the domain of the RVE as well as the interfaces by selecting each failure path as a partition. The failure paths within the microstructure are identified by conducting detailed RVE-level simulations. The RVE is subjected to uniform macroscopic strain modes (e.g., uniaxial tensile or compression and shear). Figure 2 illustrates the identification of the failure paths in a 2-D particle reinforced matrix under uniform macroscopic axial and shear strains. The failure path due to each loading condition

is marked as an individual partition as shown in Fig. 2e. RVE-level simulations were conducted by applying Dirichlet conditions along the boundaries when determining the failure paths. This, along with the unstructured finite element mesh leads to unsymmetric failure paths despite symmetry in the RVE geometry. Periodic boundary conditions are maintained along the RVE boundaries in the multiscale model.

The failure paths associated with different loading modes intersect each other as demonstrated in Fig. 2. Hence, the phase partitions are allowed to overlap. The phase shape functions, are selected to accommodate such an overlap. Let the domain of the RVE be partitioned into n possibly intersecting subdomains, denoted by $\Theta^{(\gamma)}$, $\gamma = 1, 2, \ldots, n$. The union of the subdomains spans the domain of the RVE:

$$\Theta \equiv \bigcup_{\gamma=1}^{n} \Theta^{(\gamma)} \tag{52}$$

The intersection between two partitions are denoted as $\Theta^{(\gamma\eta)} \equiv \Theta^{(\gamma)} \cap \Theta^{(\eta)}$. A material point within the RVE may lie in all n partitions or less. The intersections between multiple partitions are defined by repetitive Greek superscripts: $\Theta^{(\gamma\eta\nu\ldots)} \equiv \Theta^{(\gamma)} \cap \Theta^{(\eta)} \cap \Theta^{(\nu)} \ldots$. The shape functions for the reduced order model, $N_{\text{ph}}^{(\gamma)}$, are chosen as:

$$N_{\text{ph}}^{(\gamma)}(\mathbf{y}) = \begin{cases} \dfrac{1}{i} & \text{if} \quad \mathbf{y} \in \Theta_i^{(\gamma)} \\ 0 & \text{elsewhere} \end{cases} \tag{53}$$

in which, $i = 1, 2, \ldots, n$, and;

$$\Theta_1^{(\gamma)} \equiv \Theta^{(\gamma)} \setminus \bigcup_{\eta=1}^{n} \Theta^{(\gamma\eta)} \tag{54}$$

$$\Theta_2^{(\gamma)} \equiv \bigcup_{\eta=1}^{n} \left[\Theta^{(\gamma\eta)} \setminus \bigcup_{\nu=1}^{n} \Theta^{(\gamma\eta\nu)} \right] \tag{55}$$

The expressions for $\Theta_3^{\gamma} \ldots \Theta_n^{\gamma}$ are derived analogously. The shape functions defined in

Eq. 53 allow the possibility of intersecting shape functions, and satisfy the partition of unity property:

$$\sum_{\gamma=1}^{n} N_{\text{ph}}^{(\gamma)}(\mathbf{y}) = 1; \;\; \mathbf{y} \in \Theta \tag{56}$$

The interface shape functions are continuous across the partitions to satisfy the continuity of tractions and displacement jumps across the interface partitions. Consider the partitioning of the interface S into m overlapping subdomains $S^{(\alpha)}$. The interface shape function, $N_{\text{int}}^{(\alpha)}$, is a linear combinations of standard finite element shape functions corresponding to the nodes along the interface partition, $S^{(\alpha)}$ [46]

$$N_{\text{int}}^{(\alpha)}(\mathbf{y}) = \sum_{a \in S^{(\alpha)}} N_a(\mathbf{y}); \quad \mathbf{y} \in S \tag{57}$$

in which, N_a is the standard finite element shape function associated with the microscopic finite element mesh node a.

4.2 Numerical Evaluation of the Reduced-Order Model

The evaluation of the reduced order model for the microscale problem constitutes the macroscopic stress update at a macroscopic point. The reduced order model is evaluated using the active set strategy to account for the contact conditions at the interfaces.

Given: At a macroscopic material point $\mathbf{x}$ and at time t, the equilibrium state defined by the macroscopic strain tensor ${}_t\bar{\boldsymbol{\epsilon}}$; the inelastic strain and displacement jump coefficients, ${}_t\boldsymbol{\mu}^{(\gamma)}$ and ${}_t\hat{\boldsymbol{\delta}}^{(\alpha)}$, respectively, where $\gamma = 1, 2, \ldots, n$ and $\alpha = 1, 2, \ldots, m$; state variables ${}_t\mathbf{q}^{(\gamma)}$ and ${}_t\mathbf{q}_{\text{int}}{}^{(\alpha)}$, which define the evolution of the phase and interface damage state, ${}_t\omega_{\text{ph}}^{(\gamma)}$ and ${}_t\omega_{\text{int}}^{(\alpha)}$, respectively; as well as the change in the macroscopic strain state, $\Delta\bar{\boldsymbol{\epsilon}}$ (taking an assumed strain approach in the numerical evaluation of the macroscopic boundary value problem).

Compute: The current values (at time: $t+\Delta t$) of the inelastic strain and displacement

coefficients, $\boldsymbol{\mu}^{(\gamma)}$ and $\hat{\boldsymbol{\delta}}^{(\alpha)}$, respectively; the current damage state, $\omega_{\text{ph}}^{(\gamma)}$ and $\omega_{\text{int}}^{(\alpha)}$; state variables, $\mathbf{q}^{(\gamma)}$ and $\mathbf{q}_{\text{int}}{}^{(\alpha)}$ and the macroscopic stress, $\bar{\boldsymbol{\sigma}}$.

In this section, we will employ vector notation using the classical index contractions (e.g., $\mathbf{L} = \{L_{IJ}\}) \leftarrow \{L_{ijkl}\}$). A left subscript t indicates the value of the function at time t. A left superscript denotes iteration count. The eigendeformation vector is defined as:

$$\mathbf{d} = \left\{ \boldsymbol{\mu}^{(1)}, ..., \boldsymbol{\mu}^{(n)}, \hat{\boldsymbol{\delta}}^{(1)}, ..., \hat{\boldsymbol{\delta}}^{(m)} \right\}^T \tag{58}$$

The active set is defined as the set of all interface partitions in which normal displacement jump coefficients are zero:

$$\mathcal{A} = \left\{ \alpha \mid \alpha \in \{1, ..., m\} ;\ \delta^{N(\alpha)} = 0 \right\} \tag{59}$$

We define the discrete system of nonlinear equations, Ψ, based on reduced order model as:

$$\Psi\left(\mathbf{d}\right) = \mathbf{K}\left(\omega_{\text{ph}}^{(\gamma)}, \omega_{\text{int}}^{(\alpha)}\right)\mathbf{d} + \mathbf{f}\left(\omega_{\text{ph}}^{(\gamma)}\right) \tag{60}$$

in which,

$$\mathbf{K}\left(\omega_{\text{ph}}^{(\gamma)}, \omega_{\text{int}}^{(\alpha)}\right) = \mathbf{K_t}\left(\omega_{\text{int}}^{(\alpha)}\right) + \sum_{\Delta=1}^{n}\left[1 - \omega_{\text{ph}}^{(\Delta)}\right]\mathbf{K}^{(\Delta)} \tag{61}$$

and,

$$\mathbf{K}^{(\Delta)} = \begin{bmatrix} \mathbf{F}^{(1\Delta 1)} & \dots & \mathbf{F}^{(1\Delta n)} & \mathbf{G}^{(1\Delta 1)} & \dots & \mathbf{G}^{(1\Delta m)} \\ \vdots & \ddots & \vdots & \vdots & \ddots & \vdots \\ \mathbf{F}^{(n\Delta 1)} & \dots & \mathbf{F}^{(n\Delta n)} & \mathbf{G}^{(n\Delta 1)} & \dots & \mathbf{G}^{(n\Delta m)} \\ \hat{\mathbf{G}}^{(1\Delta 1)} & \dots & \hat{\mathbf{G}}^{(1\Delta n)} & \mathbf{H}^{(1\Delta 1)} & \dots & \mathbf{H}^{(1\Delta m)} \\ \vdots & \ddots & \vdots & \vdots & \ddots & \vdots \\ \hat{\mathbf{G}}^{(m\Delta 1)} & \dots & \hat{\mathbf{G}}^{(m\Delta n)} & \mathbf{H}^{(m\Delta 1)} & \dots & \mathbf{H}^{(m\Delta m)} \end{bmatrix} \tag{62}$$

$\mathbf{K}^{(\Delta)}$ are *symmetric* matrices since $\hat{\mathbf{G}}^{(\alpha\Delta\eta)} = \mathbf{G}^{T(\eta\Delta\alpha)}$, $\mathbf{F}^{(\eta\Delta\gamma)} = \mathbf{F}^{T(\gamma\Delta\eta)}$ and $\mathbf{H}^{(\alpha\Delta\beta)} =$

$\mathbf{H}^{T(\beta\Delta\alpha)}$. K^t_{trac} is defined as

$$\mathbf{K_t} = \begin{bmatrix} 0 & \cdots & 0 & 0 & \cdots & 0 \\ \vdots & \ddots & \vdots & \vdots & \ddots & \vdots \\ 0 & \cdots & 0 & 0 & \cdots & 0 \\ 0 & \cdots & 0 & \hat{\mathbf{k}}^{(1)} & \cdots & 0 \\ \vdots & \ddots & \vdots & \vdots & \ddots & \vdots \\ 0 & \cdots & 0 & 0 & \cdots & \hat{\mathbf{k}}^{(m)} \end{bmatrix}; \quad \hat{\mathbf{k}}^{(\alpha)} = \left(1 - \omega^{(\alpha)}_{\text{int}}\right) \begin{bmatrix} k^{(\alpha)}_N & 0 & 0 \\ 0 & k^{(\alpha)}_T & 0 \\ 0 & 0 & k^{(\alpha)}_T \end{bmatrix} \tag{63}$$

The symmetry of $\mathbf{K}$ leads to this formulation being denoted as a *symmetric formulation*. The solution of $\Psi = 0$ is evaluated by symmetric nonlinear solvers rather than unsymmetric ones as has been the case in previous formulations. $\mathbf{f}$ is defined as

$$\mathbf{f}\left(\omega^{(\gamma)}_{\text{ph}}\right) = \sum_{\Delta=1}^{n} \left[1 - \omega^{(\Delta)}_{\text{ph}}\right] \mathbf{f}^{(\Delta)} \tag{64}$$

and,

$$\mathbf{f}^{(\Delta)} = \left\{\mathbf{C}^{(1\Delta)}, ..., \mathbf{C}^{(n\Delta)}, \mathbf{D}^{(1\Delta)}, ..., \mathbf{D}^{(m\Delta)}\right\}^T \bar{\boldsymbol{\epsilon}} \tag{65}$$

In the case of tensile loading throughout the interface, the active set is empty ($\mathcal{A} = \emptyset$), $\Psi(\mathbf{d}) = 0$ solves the reduced order model. When $\mathcal{A} \neq \emptyset$ a reduced system of equations is defined:

$$\Psi_{\mathcal{A}}(\mathbf{d}) = \mathbf{K}_{\mathcal{A}}\mathbf{d}_{\mathcal{A}} + \mathbf{f}_{\mathcal{A}} \tag{66}$$

in which, $\mathbf{d}_{\mathcal{A}}$ and $\mathbf{f}_{\mathcal{A}}$ is constructed by removing each row which corresponds to $\delta^{(\alpha)}_N$ for each partition α in $\mathcal{A}$, from $\mathbf{d}$ and $\mathbf{f}$, respectively. $\mathbf{K}_{\mathcal{A}}$ is constructed by removing each row and column, which corresponds to $\delta^{(\alpha)}_N$ for each partition α in $\mathcal{A}$, from $\mathbf{K}$. The rows removed from Eq. 60 form:

$$\Psi_{\bar{\mathcal{A}}}(\mathbf{d}) = \mathbf{K}_{\bar{\mathcal{A}}}\mathbf{d}_{\bar{\mathcal{A}}} + \mathbf{f}_{\bar{\mathcal{A}}} \tag{67}$$

The reduced order model is evaluated by ensuring $\Psi_{\mathcal{A}}(\mathbf{d}) = 0$ and $\Psi_{\bar{\mathcal{A}}}(\mathbf{d}) \geq 0$ are satisfied. The latter condition is necessary to ensure negative tractions upon compressive loading along the interfaces. The computational algorithm to evaluate the reduced order problem based on the active set strategy is provided in Box 1. The algorithm is initiated by setting the working set, which approximates the active set at $(t + \Delta t)$, to the active set at time t, as well as setting the eigendeformation vector to ${}_t\mathbf{d}$ (Step 1). Within each iteration k, the test eigendeformation vector, ${}^k\hat{\mathbf{d}}$ is evaluated by a standard nonlinear root finding algorithm, such as Newton-Raphson or quasi-Newton methods (Step 2a). In this chapter, a quasi-Newton SR1 method [42] is employed to compute the roots of $\Psi_{{}^k\mathcal{W}}$. In this method, a symmetric-rank-one matrix is added to an approximation of the Jacobian of $\Psi_{{}^k\mathcal{W}}$ at each iteration of the nonlinear solver. In practice, this update has been shown to provide very good approximations of the Jacobian resulting in superlinear convergence. The advantages of quasi-Newton methods are that they do not require an explicit formula for the Jacobian and that the update can be performed on the inverse Jacobian alleviating the need to solve a linear system of equations at each iteration. In this paper, the algorithm is initialized with a finite difference approximation to the Jacobian. If the computed normal displacement jump coefficients violate the impenetrability condition (Steps 2b-c), the partition with the most severe violation is added to the working set.

1. Initialize the algorithm by setting the initial guess for the eigendeformation vector and for the active set:

$$k = 1; \quad {}^{0}\mathbf{d} = {}_{t}\mathbf{d}; \quad {}^{1}\mathcal{W} = {}_{t}\mathcal{A}$$

in which, ${}^{k}\mathcal{W}$ denotes the *working set*. The working set is an approximation to the active set at iteration k.

2. Loop over the iterations k:

   (a) Compute ${}^{k}\hat{\mathbf{d}}$ by evaluating $\Psi_{{}^{k}\mathcal{W}}\left(\hat{\mathbf{d}}\right) = 0$ using a standard nonlinear root finding algorithm.

   (b) Loop over each interface partition, α, which is not in the working set (i.e., $\alpha \notin {}^{k}\mathcal{W}$):

      i. If the impenetrability condition at partition α is violated (i.e., ${}^{k}\hat{\delta}_{N}^{(\alpha)} < 0$), compute the step size $0 < \lambda^{(\alpha)} < 1$ for each interface partition violating the impenetrability condition as:

$$\lambda^{(\alpha)} = \frac{{}^{k-1}\delta_{N}^{(\alpha)}}{{}^{k}\hat{\delta}_{N}^{(\alpha)} - {}^{k-1}\delta_{N}^{(\alpha)}}$$

   (c) If the step size is reduced (i.e., $\left\{\lambda^{(\alpha)}\right\} \neq \emptyset$):

      i. Compute $\beta = \arg\min\left\{\lambda^{(\alpha)}\right\}$
      ii. Update the working set: ${}^{k+1}\mathcal{W} = {}^{k}\mathcal{W} \cup \{\beta\}$
      iii. $k \leftarrow k + 1$
      iv. ${}^{k}\mathbf{d} = \lambda^{(\beta)}\left({}^{k}\hat{\mathbf{d}} - {}^{k-1}\mathbf{d}\right) + {}^{k-1}\mathbf{d}$
      v. Return to the beginning of the iteration loop

   (d) Check if the unilateral conditions are violated in any partition within the working set: (i.e., If any component of $\Psi_{{}^{k}\bar{\mathcal{W}}}(\mathbf{d}) < 0$)

      i. Compute $\beta = \arg\min\left(\Psi_{{}^{k}\bar{\mathcal{W}}}\right)$
      ii. Update the working set: ${}^{k+1}\mathcal{W} = {}^{k}\mathcal{W} - \{\beta\}$,
      iii. $k \leftarrow k + 1$
      iv. ${}^{k}\mathbf{d} = {}^{k}\hat{\mathbf{d}}$
      v. Return to the beginning of the iteration loop

   (e) Update the eigendeformation vector: $\mathbf{d} = {}^{k}\mathbf{d}$

   (f) Update the active set: $\mathcal{A} = {}^{k}\mathcal{W}$

   (g) Exit the algorithm

   End iteration loop

Box 1: The active set algorithm for evaluation of the reduced order model with unilateral contact constraints.

When the computed normal displacement jump coefficients do not violate the impenetrability condition, the unilateral contact constraints are checked within the active set. If the unilateral contact conditions are violated (i.e., if the computed interface traction coefficients are positive at partitions within the working set), the partition with the most severe violation (largest positive interface traction coefficient) is removed from the active set (Step 2d). When the unilateral contact constraints are satisfied, the active set, the eigendeformation vector, the associated internal state variables, and damage variables are updated (Steps 2e-g).

4.3 Two-Order Reduced Modeling

Reduced-order models fail to accurately capture the post-failure response of the representative volume element. The failure is defined as the loss of load carrying capacity along at least one loading direction. For instance, full damage within any one of the failure paths along with interface debonding in the RVE illustrated in Fig. 2 cause failure along the associated load direction. The reduced order models exhibit spurious residual stiffness upon failure, which prohibits proper redistribution of the stresses at the macroscopic scale. While increasing the model order diminishes the spurious residual stiffness, this approach increases the computational cost.

We propose a two-order modeling scheme to eliminate the residual-stress fields upon failure without significantly compromising the computational efficiency. In this approach, the stresses are computed based on a high order model, whereas the damage coefficients are evaluated using the low-order reduced-order model described in Section 4.1. The stress-update procedure for the two-order reduced model is as follows:

1. Evaluate the eigendeformation vector, $\mathbf{d}_{\text{low}}$, and damage coefficients, $\omega_{\text{ph}}^{(\gamma)}$; $\gamma = 1, 2, \ldots, n_{\text{low}}$ and $\omega_{\text{int}}^{(\alpha)}$; $\alpha = 1, 2, \ldots, m_{\text{low}}$ for the low-order model using the numerical procedure described in Section 4.2. n_{low} and m_{low} are the orders for

the low-order model selected by the reduced-order model development strategy described in Section 4.1.

2. Map the damage coefficients of the low-order model onto the high-order model partitions. The mapping of the damage coefficients onto the high-order model partitions is trivial when the high-order model is constructed by hierarchical subpartitioning of the low-order model. In this study, each finite element within the RVE domain constitutes a partition for the high-order model.

3. Evaluate the eigendeformation vector, $\mathbf{d}_{\text{high}}$, for the high order model by solving the *linear* system:

$$\mathbf{d}_{\text{high}} = \mathbf{K}_{\text{high}}^{-1}\mathbf{f}_{\text{high}} \tag{68}$$

4. Compute macroscopic stress (Eq. 48), using the eigendeformation vector of the high-order model.

5 Numerical Verification

The capabilities of the proposed reduced order modeling methodology are verified against direct finite element simulations. The verification study consists of (1) analysis of an RVE response and assessment of the reduced order model predictions, and (2) a three-point bending problem to assess the capabilities of the reduced order model in capturing the overall failure response of macroscopic structures.

5.1 RVE Analysis

The multiscale methodology described in the previous sections is applied to develop a meso-mechanical model for a 2-D composite matrix with a circular inclusion. Figure 2 illustrates the geometry of the microstructure. The evolution of damage within the matrix and along the interface is modeled based on continuous damage mechanics

models proposed in [46] for brittle composite constituents. The reinforcement is assumed to behave elastically within the range of applied loads.

The capabilities of the proposed multiscale model in capturing the failure modes for a range of loading conditions are verified by comparing the model simulations to direct numerical simulation of the representative volume element. The finite element mesh employed in these simulations is shown in Fig. 2. The characteristic material length scale associated with the matrix constituent is assumed to be 1/8 of the RVE size. The finite element mesh of the RVE is designed to have an average size of 1/8 of the RVE length scale to avoid numerical errors associated with mesh-sensitivity. The multiscale model is developed based on the reduced order model development strategy described in Section 4.1. The reduced order model is developed using the biaxial tension, uniaxial tension and shear loading modes. The partitioning of the reduced order model is shown in Fig. 2. The matrix phase and the interface are modeled using 6 and 4 partitions, respectively. This model is referred to as SBU-4-6 in the remainder of this chapter.

The performance of model SBU-4-6 is compared to the results of the direct numerical simulations for the biaxial, uniaxial and shear loading cases. The force displacement diagrams in addition to the damage evolution in the interface and phase partitions are shown in Figs. 3-5. In biaxial loading, the failure along the interface is uniform and precedes the failure within the matrix phase. Upon interface debonding, the failure within the matrix propagates in the vertical and lateral directions. The evolution of damage within the matrix partitions and the interface clearly show that the failure modes are accurately captured by SBU-4-6. A similar trend is observed in model predictions when subjected to uniaxial (Fig. 5) and shear (Fig. 4) loading conditions. The failure mechanisms are captured with good accuracy when compared to the reference direct numerical simulations of the RVE.

Figure 6 illustrates the capability of the proposed reduced-order model in elimi-

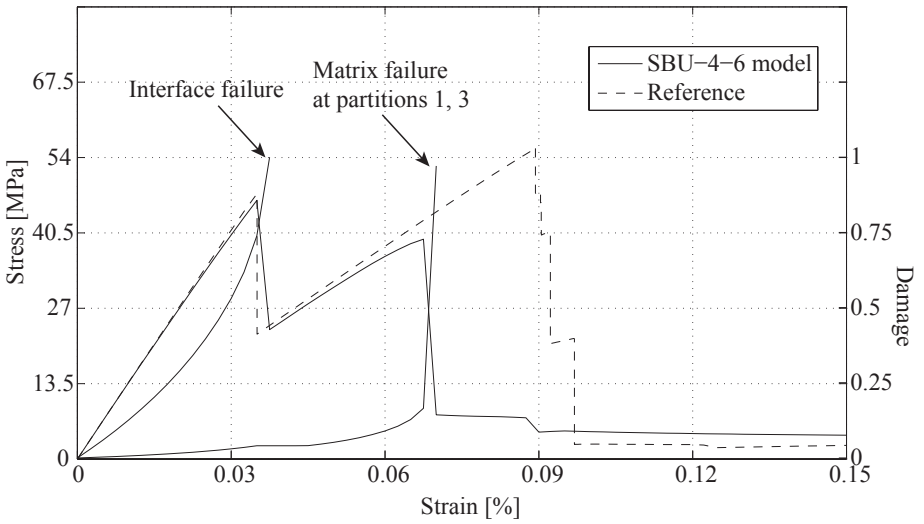

Figure 3: Stress-strain response and damage evolution within the RVE when subjected to uniform biaxial loading.

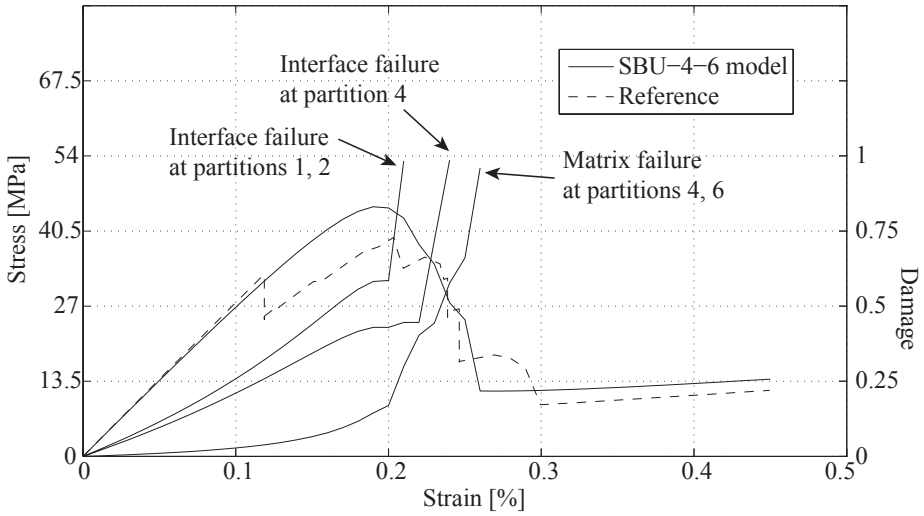

Figure 4: Stress-strain response and damage evolution within the RVE when subjected to shear loading.

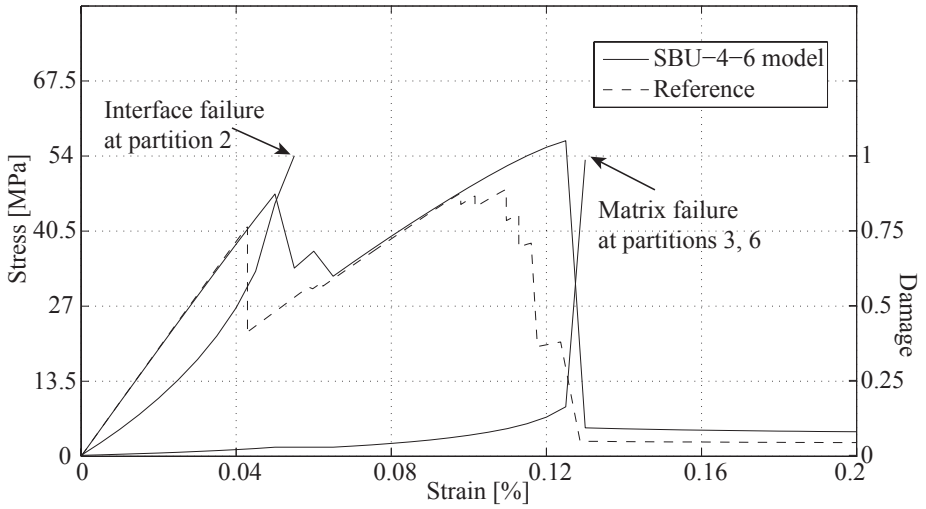

Figure 5: Stress-strain response and damage evolution within the RVE when subjected to uniaxial tensile loading in the lateral direction.

nating the spurious residual stresses in the post-failure regime. The spurious residual stresses present due to the modeling errors associated with reduction of the model order typically pollute the post-failure stress fields in the macroscopic analyses, since this effect partially constrains stress redistribution. Figure 6 compares the predictions of the proposed model along with the predictions of an eigendeformation-based homogenization model (EHM (0+1) point model) proposed in Ref. [46] along with the direct numerical simulations when subjected to uniform biaxial tension. The matrix-reinforcement interface is assumed to remain continuously bonded throughout the simulation. A 1-partition reduced order model, SBU-0-1, is adopted. The predictions of the EHM (0+1) point model clearly demonstrate a residual strength upon failure of the matrix partition, while SBU-0-1 eliminates the spurious residual stresses.

The values of the model parameters used in the reduced order model are different than those of the direct numerical simulations. The objective of the proposed reduced order model is to capture the failure mechanisms within the heterogeneous material in a computationally efficient and accurate manner. The simulations conducted in this section demonstrate that the main failure mechanisms are captured with reasonable accuracy with the reduced order model. The model parameters for the reduced order

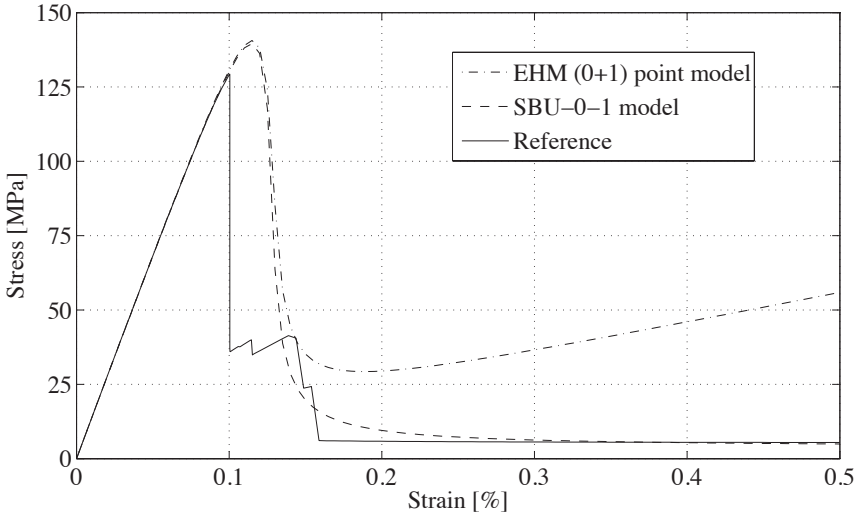

Figure 6: Stress-strain response when subjected to uniform biaxial tensile loading. The post-failure spurious residual stresses are eliminated with the proposed reduced order model.

model are computed by minimizing the discrepancy between the ultimate strength predicted by the proposed reduced order model and the direct numerical simulations in a least square sense. From the validation perspective, the reduced order model can be adopted to predict the response of heterogeneous systems by calibrating the material parameters of the damage models directly, based on experimental observations. A general discussion and methodologies for calibration and validation procedures for multiscale models are discussed in Ref. [47].

5.2 Crack Propagation in a Beam Subjected to Three-Point Bending

We consider a three-point bending of a cracked composite plate. The predictions of the SBU-4-6 model are compared to a fine scale finite element model, which consists of 256 RVEs described in Section 5.1. The macroscale mesh for the multiscale model consists of 256 4-noded quadrilaterals. The volume fraction of the circular inclusions is 30%. The circular inclusions are assumed to be isotropic and linear elastic with $E = 200$GPa and $\nu = 0.3$. Damage processes are considered within the central third, and the matrix material is assumed to be linear elastic in the remainder of the plate.

The elastic properties of the matrix material are $E = 60$GPa and $\nu = 0.3$. The initial vertical matrix crack is assumed to extend 1/8th of the plate width.

Figures 7a and 7b illustrate the propagation of the initial matrix crack and damage within the matrix as predicted by the direct numerical simulation and the SBU-4-6 model. In these simulations, the interface between the matrix and the inclusions are assumed to remain fully bonded for the duration of the loading. The propagation of the initial crack is arrested approximately halfway through the plate thickness when shear cracks develop at the edges of the applied loading. Figure 7a shows the damage state within the third phase partition depicted in Fig. 2b. A comparison of the reaction force-applied displacement curves of the numerical simulation and the proposed multiscale model is shown in Fig. 8. The reduced-order model slightly over-predicts the strength of the composite plate. The errors associated with the SBU-4-6 are due to the blunting of the response fields across the failure paths within the microstructure by the model-reduction methodology. SBU-4-6 successfully captures the propagation and arrest of the initial crack and subsequent shear crack formation with reasonable accuracy.

Figures 10a and 10b show the failure of the three-point bending plate in the presence of interface effects. The direct numerical simulation with the fine mesh shows that the path of crack propagation is significantly altered when the inclusion-matrix debonding is considered. The path of crack propagation displays a more jagged pattern with interaction between the matrix and interface cracks. Figure 10a displays the state of interface damage across the macroscale. The extent of interface damage is predicted by the SBU-4-6 model with reasonable accuracy. The comparison of the applied force-deflection curve predicted with the proposed multiscale model and the direct numerical simulations is shown in Fig. 9. The degradation effect of interface debonding on the overall performance of the plate is predicted by the proposed multiscale model with good accuracy.

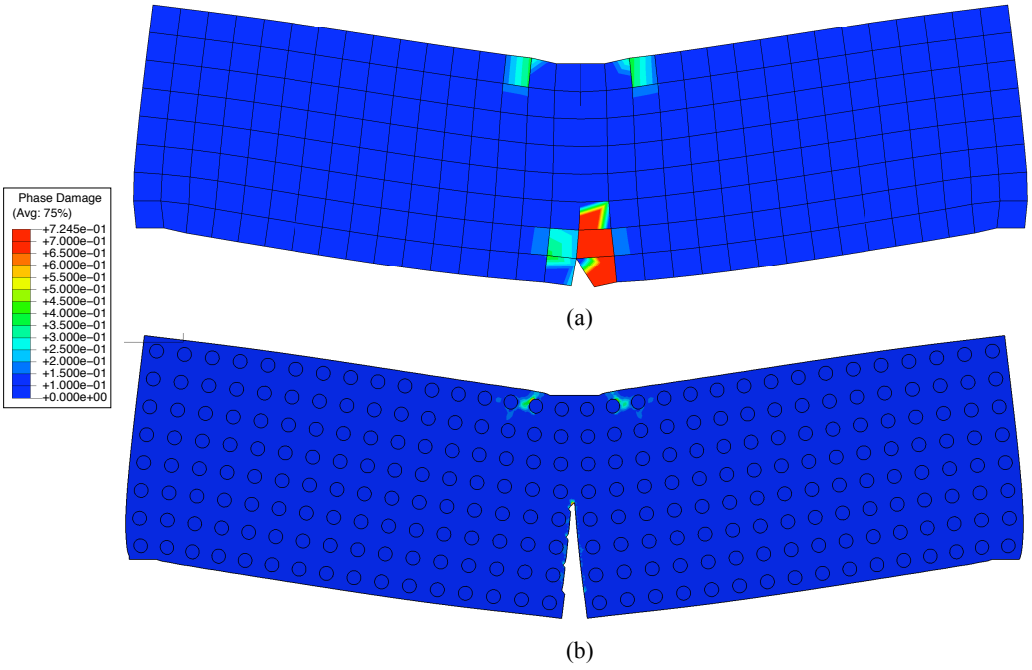

Figure 7: Damage profile of the 3-point bending beam specimen at the onset of shear fracture in the absence of interface debonding effects: (a) The prediction of the SBU-4-6 model. The contour represents the state of damage at phase partition 3; (b) Damage distribution predicted by the direct numerical simulation.

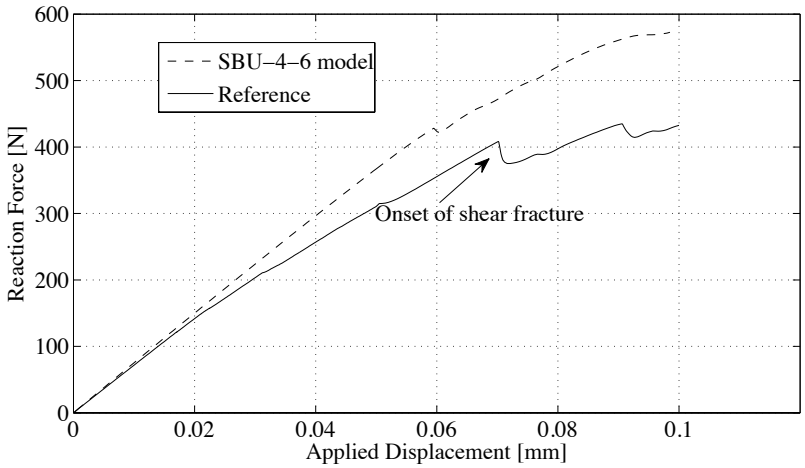

Figure 8: Comparison of the load-deflection curve between the multiscale SBU-4-6 model and the direct numerical simulation in the absence of interface debonding effects.

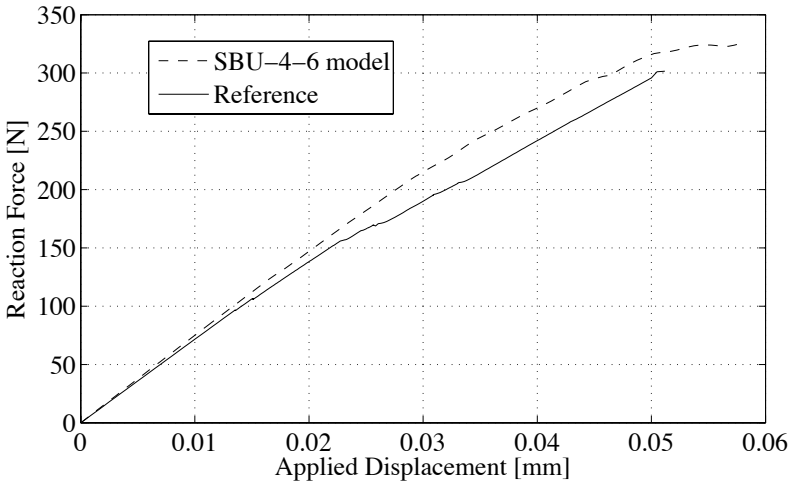

Figure 9: Comparison of the load-deflection curve between the multiscale SBU-4-6 model and the direct numerical simulation in the presence of interface debonding effects.

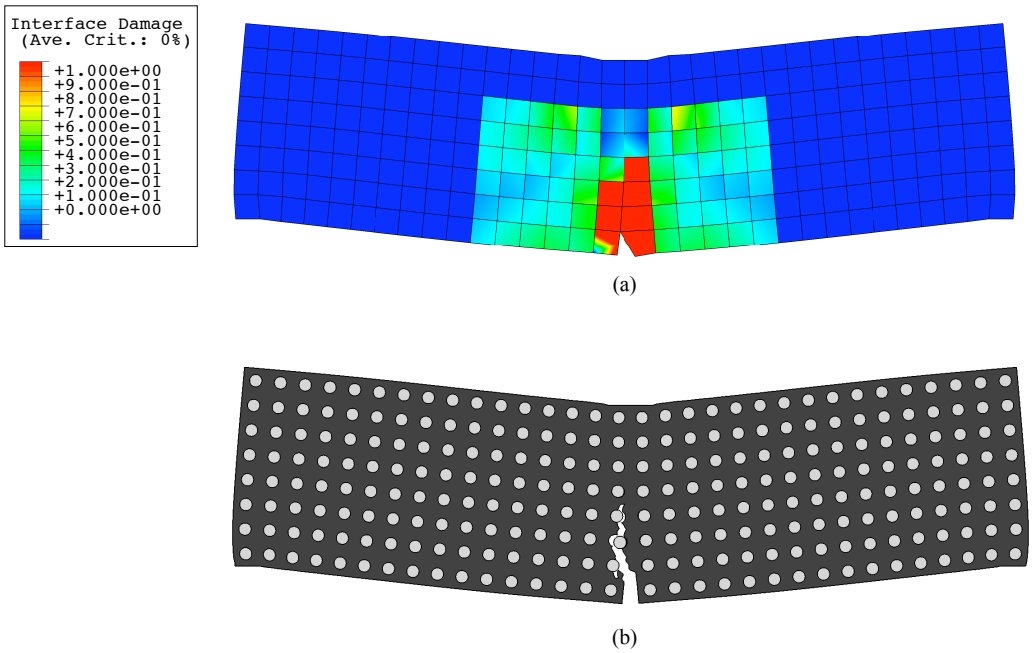

Figure 10: The deformed configuration of the 3-point bending beam specimen in the presence of interface debonding effects: (a) The prediction of the SBU-4-6 model. The contour represents the state of interface damage; (b) Crack profile predicted by the direct numerical simulation.

It is important to ascertain the reduced order model's computational performance, but one should note that a running time comparison between the reduced order model and the direct numerical simulation depends highly on the specific features of the problem. In this case, the direct numerical simulation had a mesh containing approximately 90,000 elements. With this configuration, the direct numerical simulation ran over several hours in comparison to the SBU-4-6 model which ran in several minutes. If the RVEs had more complex geometry requiring higher mesh density, the direct numerical simulation would have had many more elements and thus a slower running time. However, if the same number of failure paths were used in constructing a reduced-order model for the more complex microstructural geometry, the running time of the reduced order model would remain more or less the same. In general, increasing the number of elements required in meshing a single RVE increases the relative performance of the reduced order model. Though even here, with such a simple RVE, the performance was increased by an order of magnitude.

CHAPTER 3

MULTIPLE SPATIO-TEMPORAL SCALE MODELING OF COMPOSITES SUBJECTED TO CYCLIC LOADING

1 Introduction

A plethora of experimental investigations in the past few decades have shed light into the failure mechanisms in fiber reinforced composites subjected to cyclic loading (e.g., [16, 31], among many others). From the modeling perspective, continuum damage mechanics and fracture mechanics models are typically employed to describe failure under cyclic loading. Fracture mechanics based approaches rely on incorporation of distinct cracks at the scale of the structure [41], at the scale of the constituents [50], or both [9]. A fracture mechanics based crack propagation criteria (e.g., Paris law) and a numerical methodology for crack propagation such as mesh refinement [35], virtual crack closure [37], cohesive zone [38], or the extended finite element method [36] are employed to describe fracture events within the composite material. In the continuum damage mechanics approach, failure is described as the initiation and growth of diffuse damage (e.g., microcrack density) typically represented using internal state variables. The evolution of diffuse damage as a function of loading history is modeled within the nonlinear, path-dependent constitutive modeling context by employing micromechanically-informed damage evolution models such as the critical element model [51, 60] and others [2, 53, 55].

Modeling complex failure mechanisms and their interactions in composite structures subjected to cyclic loading is a multiscale problem in space and time. Multiple spatial scales exist since many failure mechanisms initiate and grow at the scale

of the composite constituents defined by the representative volume of the composite, whereas the overall failure is assessed at the scale of the structure or structural component. Multiple temporal scales exist because of the disparity between the characteristic loading period, which may be on the order of seconds, and the overall life of the structure which may be on the order of years. The computational homogenization method [32, 62] based on mathematical homogenization theory [6, 10, 52, 58] is a powerful multiscale modeling approach, which has been applied to nonlinear solid mechanics problems involving multiple spatial scales including the failure of composite materials.

Straightforward application of the computational homogenization-based modeling to evaluate the cyclic response of composite structures is prohibitive due to the tremendous computational cost associated with solving a two-scale nonlinear problem in space for large number of time steps necessary to evaluate life under cyclic loading. This difficulty is addressed using two approaches: (a) by introducing reduced order (meso-mechanical) models that can represent the small-scale response at a fraction of the cost without significantly compromising the solution accuracy; and, (b) by introducing cycle-stepping methodologies that eliminate the need to resolve to resolve each load cycle throughout the life of the structure or structural component. Reduced-order models based on transformation field analysis [19], proper orthogonal decomposition [64], eigenstrains [23], and others [1, 29, 40] have brought significant progress to reduced-order modeling in the presence of multiple spatial scales. The previous chapter along with the recent work of Oskay and coworkers [17, 46] propose a reduced order computational homogenization framework based on the eigendeformation idea which provides (a) the ability to model multiple failure mechanisms at the microstructure including matrix and fiber cracking, and interfacial debonding; and, (b) a hierarchy of reduced order models that can be adapted to meet accuracy needs. The tyranny of temporal scales is addressed by employing cycle-jump technique [48] or

computational homogenization-based temporal multiscale modeling [22, 44, 45] that has been employed in the context of single spatial scale continuum damage mechanics and damage-plasticity models. More recently, Fish and coworkers applied cycle-jump techniques to investigate the fatigue life of composites [24, 26]. Despite progress, computational multiple spatio-temporal scale modeling for accurate, efficient and reliable prediction of failure in composite structures subjected to cyclic loading conditions remains to be a challenge.

In this chapter, a new multiple spatio-temporal scale model for prediction of cyclic failure in composite materials is presented. The capabilities of the proposed model are demonstrated using a suite of experiments conducted on graphite fiber reinforced epoxy composites. The proposed model is devised using the computational homogenization theory with multiple spatial and temporal scales. The idea of almost periodicity of the response fields at the temporal scales [44] is employed to account for the presence of irreversible damage fields that violate the commonly assumed periodicity conditions of the response fields. The proposed model employs a reduced order modeling approach at the spatial domain using the eigendeformation based homogenization with symmetric coefficients, and an adaptive time stepping strategy based on the modified multistep method to efficiently evaluate the response of a structural component by resolving only a fraction of the total number of cycles to failure. The proposed multiscale model is calibrated based on a suite of experiments conducted on graphite fiber reinforced epoxy (IM7/977-3) composite specimens under monotonic and cyclic loads, and validated against an independent set of experiments. The novel contributions found in this chapter are two-fold: To the best of the authors' knowledge, this is the first attempt to concurrently employ computational homogenization method with multiple temporal and spatial scales for failure modeling of heterogeneous materials subjected to cyclic loading. The second-order adaptive time stepping methodology proposed for adaptive error control in time provides improvements in

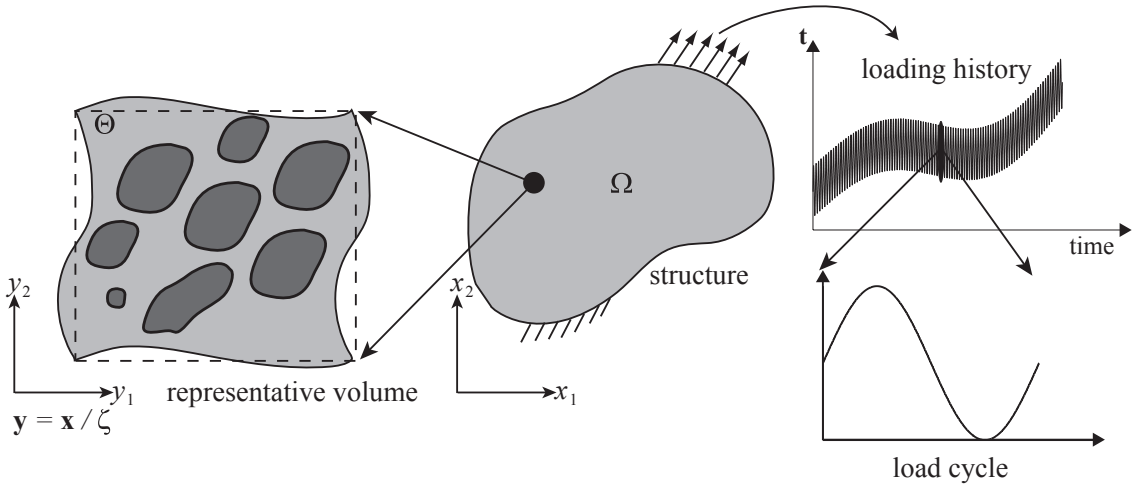

Figure 11: Multiple spatial and temporal scales.

accuracy compared to the first order time stepping approaches commonly employed in the context of cycle jump and temporal homogenization.

The remainder of this chapter is organized as follows: Section 3.2 describes the multiple spatio-temporal problem setting. In Section 3.3, the computational approach used modeling cyclic failure behavior of composites is formulated. Section 3.4 and 3.5 provide the implementation details and the verification of the proposed modeling approach, respectively. Section 3.6 describes the experiments for calibration and validation of the computational approach, the calibration procedure of the material parameters based on the experimental data, and the validation of the model.

2 Problem Statement

We consider the progressive failure of a composite structure subjected to cyclic loading conditions. Let $\Omega \subset \mathbb{R}^d$ be the domain of a heterogeneous body, where $d = 1, 2$ or 3 denotes the number of space dimensions. Ω is composed of the repetition of a small periodic representative volume element (RVE), $\theta \subset \mathbb{R}^d$, composed of two or more distinct constituent materials as illustrated in Fig. 11. The governing equations

describing the failure of the heterogeneous body are defined as ($\mathbf{x} \in \Omega$ and $t \in [0, t_f]$):

$$\nabla \cdot \boldsymbol{\sigma}^{\zeta\eta}(\mathbf{x}, t) + \mathbf{b}^{\zeta}(\mathbf{x}) = 0 \tag{69}$$

$$\boldsymbol{\sigma}^{\zeta\eta}(\mathbf{x}, t) = \left[1 - \omega^{\zeta\eta}(\mathbf{x}, t)\right] \mathbf{L}^{\zeta}(\mathbf{x}) : \boldsymbol{\epsilon}^{\zeta\eta}(\mathbf{x}, t) = \mathbf{L}^{\zeta}(\mathbf{x}) : \left[\boldsymbol{\epsilon}^{\zeta\eta}(\mathbf{x}, t) - \boldsymbol{\mu}^{\zeta\eta}(\mathbf{x}, t)\right] \tag{70}$$

$$\boldsymbol{\epsilon}^{\zeta\eta}(\mathbf{x}, t) = \nabla^{s} \mathbf{u}^{\zeta\eta}(\mathbf{x}, t) \tag{71}$$

$$\dot{\omega}^{\zeta\eta}(\mathbf{x}, t) = f^{\zeta\eta}\left(\boldsymbol{\sigma}^{\zeta\eta}, \boldsymbol{\epsilon}^{\zeta\eta}, \mathbf{s}^{\zeta\eta}\right) \tag{72}$$

where, $\mathbf{u}^{\zeta\eta}$ denotes displacement field; $\boldsymbol{\sigma}^{\zeta\eta}$ the Cauchy stress; $\boldsymbol{\epsilon}^{\zeta\eta}$ the total strain; $\omega^{\zeta\eta} \in [0, 1)$ the scalar damage variable; $\boldsymbol{\mu}^{\zeta\eta} = \omega^{\zeta\eta}\boldsymbol{\epsilon}^{\zeta\eta}$ the inelastic strain tensor; $\mathbf{b}^{\zeta}$ the body force; and $\mathbf{L}^{\zeta}$ the tensor of elastic moduli obeying the conditions of symmetry and positivity. The evolution of $\omega^{\zeta\eta}$ is typically nonlinear and history-dependent, and is provided in the functional form as a function of strain, stress and additional state variables, $\mathbf{s}^{\zeta\eta}$. A superposed dot denotes the material time derivative; $\mathbf{x}$ the position vector parameterizing the domain of the structure; t the time coordinate; and, $\nabla \cdot (\cdot)$, $\nabla(\cdot)$ and $\nabla^{s}(\cdot)$ the divergence, gradient and symmetric gradient operators, respectively. The boundary conditions prescribed on the body consist of slowly varying and oscillating components as illustrated in Fig. 11.

$$\mathbf{u}_i^{\zeta\eta}(\mathbf{x}, t) = \hat{\mathbf{u}}^{\eta}(\mathbf{x}, t); \quad \mathbf{x} \in \Gamma_u; \quad t \in [0, t_{\mathrm{o}}] \tag{73}$$

$$\boldsymbol{\sigma}^{\zeta\eta} \cdot \mathbf{n} = \hat{\mathbf{t}}^{\eta}(\mathbf{x}, t); \quad \mathbf{x} \in \Gamma_t; \quad t \in [0, t_{\mathrm{o}}] \tag{74}$$

where, $\hat{\mathbf{u}}$ and $\hat{\mathbf{t}}$ are the prescribed displacements and tractions on the boundaries Γ_u and Γ_t, respectively ($\Gamma = \Gamma_u \cup \Gamma_t$ and $\Gamma_u \cap \Gamma_t = \emptyset$); and, $\mathbf{n}$ is the unit normal to Γ_t. The period of oscillations is taken to be slow enough that inertial forces are insignificant and the response remains quasi-static. The superscripts ζ and η indicate that the response fields fluctuate in space and time, respectively. Double superscript indicates a response field that fluctuates in both time and space. The

spatial fluctuations arise due to the fluctuating material properties within the RVE, whereas temporal fluctuations are due to the fast oscillatory component of the loading. The fluctuating spatio-temporal response is represented by introducing microscopic and microchronological scales parameterized by $\mathbf{y} = \mathbf{x}/\zeta$ and $\tau = t/\eta$, respectively; and, $0 < \zeta \ll 1$ and $0 < \eta \ll 1$ are scaling parameters. The original response fields that fluctuate in space and time are expressed as:

$$\phi^{\zeta\eta}(\mathbf{x}, t) = \phi(\mathbf{x}, \mathbf{y}(\mathbf{x}), t, \tau(t)) \tag{75}$$

where, ϕ denotes an arbitrary response field. The macroscopic spatial derivatives of a response field are obtained through the chain rule:

$$\nabla\phi^{\zeta}(\mathbf{x}) = \nabla_{\mathbf{x}}\phi(\mathbf{x}, \mathbf{y}) + \frac{1}{\zeta}\nabla_{\mathbf{y}}\phi(\mathbf{x}, \mathbf{y}) \tag{76}$$

in which, $\nabla_{\mathbf{x}}(\cdot)$ and $\nabla_{\mathbf{y}}(\cdot)$ are gradient operators with respect to macroscopic and microscopic coordinates, respectively. All response fields are assumed to be locally periodic with respect to the microscopic coordinates within the RVE throughout the deformation process: $\phi(\mathbf{x}, \mathbf{y}) = \phi(\mathbf{x}, \mathbf{y} + \mathbf{k}\hat{\mathbf{y}})$, where, $\hat{\mathbf{y}}$ denotes the periods of the microstructure; and $\mathbf{k}$ is a $d \times d$ diagonal matrix with integer components. We consider the following spatial homogenization operator:

$$\bar{\phi} \equiv \langle\phi\rangle_{\mathbf{y}} = \frac{1}{|\Theta|}\int_{\Theta}\phi\, d\mathbf{y} \tag{77}$$

where, $|\Theta|$ denotes the volume of the RVE.

The macrochronological derivative of a response field is expressed using the chain rule as:

$$\dot{\phi}^{\eta}(t) = \dot{\phi}(t, \tau) = \phi_{,t}(t, \tau) + \frac{1}{\eta}\phi_{,\tau}(t, \tau) \tag{78}$$

where, a comma followed by a subscript variable t and τ denotes the partial time

derivative with respect to the macrochronological and microchronological coordinates, respectively. In contrast to spatial variability, local periodicity is not a valid assumption for the response fields that vary in time. This is due to the presence of irreversible mechanisms associated with damage accumulation during a load cycle. The response fields are therefore assumed to be almost periodic, which implies that at neighboring points in a temporal domain homologous by the load period, the change in the value of a response function is small but does not vanish [22, 45]. Let:

$$\langle \phi \rangle_{\tau} = \frac{1}{\tau_0} \int_0^{\tau_0} \phi(\mathbf{x}, \mathbf{y}, t, \tau)\, d\tau \tag{79}$$

denote the temporal averaging operator; and, τ_0 denote the period of scaled cyclic load ($\tau \in [0, \tau_0]$). In the rate form, the almost periodic temporal homogenization operator is [44]:

$$\dot{\tilde{\phi}}(t) \equiv \mathcal{M}(\phi)_{,t} = \tilde{\phi}_{,t}(t) + \phi_{\text{ap}}(t) \tag{80}$$

which satisfies the weak convergence property with respect to an arbitrary homogenization operator, $\tilde{(\cdot)}$; and, $\phi_{\text{ap}} = \langle \phi_{,\tau} \rangle_{\tau} / \eta$. Following the ideas of spatial homogenization theory, the natural choice for the temporal homogenization operator is the temporal averaging operator provided in Eq. 79. From the computational perspective, it is more convenient to choose a fixed-point operator that has the distributive property (i.e., $\phi = \psi\xi \rightarrow \tilde{\phi} = \tilde{\psi}\tilde{\xi}$) as evidenced by the ensuing formulation. In this study, $\tilde{\phi}(\mathbf{x}, \mathbf{y}, t) = \phi(\mathbf{x}, \mathbf{y}, t, 0)$ is adopted.

3 Computational Model

This section describes the multiscale spatio-temporal modeling approach to evaluate the failure response of heterogeneous bodies subjected to cyclic loading governed by Eqs. 69-74. The eigendeformation-based homogenization method with symmetric coefficients [17] is employed to address the multiple spatial scales, whereas temporal

homogenization with almost periodic fields is employed to efficiently predict the life of a structure without resorting to full cycle-by-cycle analysis. The cyclic damage evolution law employed to idealize the failure response of composite constituents is presented.

3.1 Multiple Scale Model

We start by expressing the displacement field of the heterogeneous body using a two-scale asymptotic expansion:

$$\mathbf{u}\left(\mathbf{x},\mathbf{y},t,\tau\right)=\bar{\mathbf{u}}\left(\mathbf{x},t,\tau\right)+\zeta\mathbf{u}^{1}\left(\mathbf{x},\mathbf{y},t,\tau\right) \tag{81}$$

in which, $\bar{\mathbf{u}}$ and $\mathbf{u}$ are the macroscopic and microscopic displacement fields, respectively. The governing equations are decomposed into macroscopic and microscopic problems through asymptotic analysis of the governing equations, which consists of substituting Eq. 81 into Eqs. 69-74, and collecting the same order terms of the resulting decompositions. The two leading order equilibrium equations are:

$$O(\zeta^{-1}) \quad : \quad \nabla_{\mathbf{y}}\cdot\boldsymbol{\sigma}\left(\mathbf{x},\mathbf{y},t,\tau\right)=0 \tag{82}$$

$$O(1) \quad : \quad \nabla_{\mathbf{x}}\cdot\boldsymbol{\sigma}\left(\mathbf{x},\mathbf{y},t,\tau\right)+\nabla_{\mathbf{y}}\cdot\boldsymbol{\sigma}^{1}\left(\mathbf{x},\mathbf{y},t,\tau\right)+\mathbf{b}\left(\mathbf{x},\mathbf{y}\right)=0 \tag{83}$$

where, $\nabla_{\mathbf{x}}\cdot(\cdot)$ and $\nabla_{\mathbf{y}}\cdot(\cdot)$ are divergence operators with respect to macroscopic and microscopic spatial coordinates, respectively; and, the body forces are assumed to remain constant in time for simplicity. The first and second order stress fields are:

$$\boldsymbol{\sigma}\left(\mathbf{x},\mathbf{y},t,\tau\right) = \left[1-\omega\left(\mathbf{x},\mathbf{y},t,\tau\right)\right]\mathbf{L}\left(\mathbf{y}\right):\left[\bar{\boldsymbol{\epsilon}}\left(\mathbf{x},t,\tau\right)+\nabla_{\mathbf{y}}^{s}(\mathbf{u}^{1})\left(\mathbf{x},\mathbf{y},t,\tau\right)\right] \tag{84}$$

$$\boldsymbol{\sigma}^{1}\left(\mathbf{x},\mathbf{y},t,\tau\right) = \left[1-\omega\left(\mathbf{x},\mathbf{y},t,\tau\right)\right]\mathbf{L}\left(\mathbf{y}\right):\left[\nabla_{\mathbf{x}}^{s}(\mathbf{u}^{1})\left(\mathbf{x},\mathbf{y},t,\tau\right)\right] \tag{85}$$

in which, $\nabla^s_{\mathbf{x}}(\cdot)$ and $\nabla^s_{\mathbf{y}}(\cdot)$ are symmetric gradient operators with respect to the macroscopic and microscopic spatial coordinates, respectively; and, $\bar{\boldsymbol{\epsilon}} = \nabla^s_{\mathbf{x}}(\bar{\mathbf{u}})$ is the macroscopic strain tensor.

Applying Eq. 78 to the damage evolution equations and collecting the same order terms yield:

$$O(\eta^{-1}) \quad : \quad \omega_{,\tau} = f^0\left(\boldsymbol{\sigma}, \boldsymbol{\epsilon}, \mathbf{s}\right) \tag{86}$$

$$O(1) \quad : \quad \omega_{,t} = f^1\left(\boldsymbol{\sigma}, \boldsymbol{\epsilon}, \mathbf{s}\right) \tag{87}$$

where, the evolution functions f^0 and f^1 are derived based on the prescribed evolution law f.

The boundary data applied to the heterogeneous body is composed of a slowly varying and a periodic oscillatory component:

$$\hat{\mathbf{u}}^\eta\left(\mathbf{x}, t\right) = \hat{\mathbf{u}}^0\left(\mathbf{x}, t\right) + \hat{\mathbf{u}}^1\left(\mathbf{x}, \tau\right) \tag{88}$$

$$\hat{\mathbf{t}}^\eta\left(\mathbf{x}, t\right) = \hat{\mathbf{t}}^0\left(\mathbf{x}, t\right) + \hat{\mathbf{t}}^1\left(\mathbf{x}, \tau\right) \tag{89}$$

Applying spatial averaging (Eq. 77) to the $O(1)$ equilibrium equation (Eq. 83), exploiting the local periodicity of the stress fields in space, and applying the almost periodic temporal homogenization operator yields the macroscale equilibrium equation. The resulting equilibrium equation along with the spatio-temporally homogenized first order stress field, and the boundary conditions provide the macrochronological-macroscopic boundary value problem.

Macrochronological - Macroscopic Problem: Given: average body force, $\bar{\mathbf{b}}$, boundary data $\hat{\mathbf{u}}^0$ and $\hat{\mathbf{t}}^0$, and the solution of the macrochronological-microscopic

problem; Find the macroscopic displacement field, $\tilde{\tilde{\mathbf{u}}}$, such that ($t \in [0, t_f]$):

$$\nabla_{\mathbf{x}} \cdot \tilde{\tilde{\boldsymbol{\sigma}}}\left(\mathbf{x}, t\right) + \bar{\mathbf{b}}\left(\mathbf{x}\right) = \mathbf{0}; \quad \mathbf{x} \in \Omega \tag{90a}$$

$$\tilde{\tilde{\boldsymbol{\sigma}}}\left(\mathbf{x}, t\right) = \left\langle (1 - \tilde{\omega})\, \mathbf{L}\left(\mathbf{y}\right) : \left[\tilde{\tilde{\boldsymbol{\epsilon}}} + \nabla^s_{\mathbf{y}}(\tilde{\mathbf{u}}^1)\right]\right\rangle_{\mathbf{y}}; \quad \mathbf{x} \in \Omega \tag{90b}$$

$$\tilde{\tilde{\mathbf{u}}} = \hat{\mathbf{u}}^0(\mathbf{x}, t); \quad \mathbf{x} \in \Gamma_u \tag{90c}$$

$$\tilde{\tilde{\boldsymbol{\sigma}}}(\mathbf{x}, t) \cdot \mathbf{n} = \hat{\mathbf{t}}^0(\mathbf{x}, t); \quad \mathbf{x} \in \Gamma_t \tag{90d}$$

Applying the temporal homogenization operator to the $O(\zeta^{-1})$ equilibrium equations (Eq. 82) along with the constitutive equation for the leading order stress (Eq. 84), and employing periodic boundary conditions for the microscale displacement field, the macrochronological-microscopic boundary value problem is obtained.

Macrochronological-Microscopic Problem: At a fixed macroscale material point $\breve{\mathbf{x}} \in \Omega$; Given: macroscale strain, $\tilde{\tilde{\boldsymbol{\epsilon}}}$, and the tensor of elastic moduli, $\mathbf{L}$; Find the displacement field, $\tilde{\mathbf{u}}^1$, such that:

$$\nabla_{\mathbf{y}} \cdot \left\{(1 - \tilde{\omega})\, \mathbf{L}\left(\mathbf{y}\right) : \left[\tilde{\tilde{\boldsymbol{\epsilon}}} + \nabla^s_{\mathbf{y}}(\tilde{\mathbf{u}}^1)\right]\right\} = \mathbf{0}; \quad \mathbf{y} \in \theta \tag{91a}$$

$$\dot{\tilde{\omega}}(\breve{\mathbf{x}}, t) = f^1\left(\tilde{\boldsymbol{\sigma}}, \tilde{\boldsymbol{\epsilon}}, \tilde{\mathbf{s}}\right) + \omega_{\mathrm{ap}}(\breve{\mathbf{x}}, t); \quad \mathbf{y} \in \theta \tag{91b}$$

$$\tilde{\mathbf{u}}^1 \text{ periodic on } \mathbf{y} \in \partial\theta \tag{91c}$$

The macro- and microscopic problems associated with the fast time scale at a fixed slow time coordinate, t, are obtained based on similar algebra, but without applying the temporal homogenization operator to the governing equations and considering the damage evolution equation with respect to the fast time scale (i.e., Eq. 86). The resulting microchronological - macroscopic and microchronological - microscopic problems are stated as follows:

Microchronological - Macroscopic Problem: At a fixed macrochronological time

$\breve{t} \in [0, t_f]$, Given: average body force, $\bar{\mathbf{b}}$, boundary data, $\hat{\mathbf{u}}$ and $\hat{\mathbf{t}}$, and the solution of the microchronological-microscopic problem; Find the macroscopic displacement field, $\bar{\mathbf{u}}$, such that ($\tau \in [0, \tau_0]$):

$$\nabla_{\mathbf{x}} \cdot \bar{\boldsymbol{\sigma}} \left(\mathbf{x}, \breve{t}, \tau\right) + \bar{\mathbf{b}} \left(\mathbf{x}\right) = \mathbf{0}; \quad \mathbf{x} \in \Omega \tag{92a}$$

$$\bar{\boldsymbol{\sigma}} = \left\langle (1-\omega)\, \mathbf{L}\left(\mathbf{y}\right) : \left[\bar{\boldsymbol{\epsilon}} + \nabla^s_{\mathbf{y}}(\mathbf{u}^1)\right] \right\rangle_{\mathbf{y}}; \quad \mathbf{x} \in \Omega \tag{92b}$$

$$\bar{\mathbf{u}} = \hat{\mathbf{u}}(\mathbf{x}, \breve{t}, \tau); \quad \mathbf{x} \in \Gamma_u \tag{92c}$$

$$\bar{\boldsymbol{\sigma}} \cdot \mathbf{n} = \hat{\mathbf{t}}(\mathbf{x}, \breve{t}, \tau); \quad \mathbf{x} \in \Gamma_t \tag{92d}$$

Microchronological-Microscopic Problem: At a fixed macroscale material point $\breve{\mathbf{x}} \in \Omega$ and a fixed macrochronological time $\breve{t} \in [0, t_f]$; Given: macroscopic strain, $\bar{\boldsymbol{\epsilon}}$, and the tensor of elastic moduli, $\mathbf{L}$; Find the microscopic displacement field, $\mathbf{u}^1$, such that:

$$\nabla_{\mathbf{y}} \cdot \left\{ (1-\omega)\, \mathbf{L}\left(\mathbf{y}\right) : \left[\bar{\boldsymbol{\epsilon}} + \nabla^s_{\mathbf{y}}(\mathbf{u}^1)\right] \right\} = \mathbf{0}; \quad \mathbf{y} \in \theta \tag{93a}$$

$$\omega_{,\tau}(\breve{\mathbf{x}}, \mathbf{y}, \breve{t}, \tau) = f^0\left(\boldsymbol{\sigma}, \boldsymbol{\epsilon}, \mathbf{s}\right); \quad \mathbf{y} \in \theta \tag{93b}$$

$$\mathbf{u}^1 \text{ periodic on } \mathbf{y} \in \partial\theta \tag{93c}$$

The macrochronological and microchronological problems are coupled through the almost periodic rate operator that defines the evolution of the temporally homogenized response fields (i.e., Eq. 91b). Therefore, the evolution of the macrochronological fields at each macrochronological time coordinate requires the solution of the microchronological problem associated with that time coordinate. The macroscale problems at the macrochronological and microchronological time scales are coupled with the respective microscale problems through the constitutive relationship (Eq. 92b). The evaluation of the macroscopic stress at each macroscopic material point requires the solution of the microscopic RVE problem associated with that material point.

When the finite element method is employed to evaluate the macroscale problem, a nonlinear microscale problem must be evaluated to update the stress at each integration point for each increment and iteration of every time step of the loading history. This is a significant computational burden.

Reduced Order Spatial Homogenization

We employ the eigendeformation-based reduced order homogenization method with symmetric coefficients (sEHM) to reduce the computational cost associated with evaluating the coupled nonlinear micro- and macroscopic problems. sEHM is introduced in chapter 2 and a brief summary is provided herein. The premise of sEHM is to devise a low-cost approximation to the nonlinear microscale boundary value problem defined over the representative volume elements based on the idea of precomputing certain microstructural information (e.g., concentration tensors, localization operators, influence functions) through linear elastic simulations prior to the analysis of the macroscale structure.

The microscale displacement field is expressed as:

$$\mathbf{u}^1(\mathbf{x},\mathbf{y},t,\tau) = \mathbf{H}(\mathbf{y}) : \bar{\boldsymbol{\epsilon}}(\mathbf{x},t,\tau) + \int_\Theta \mathbf{h}(\mathbf{y},\hat{\mathbf{y}}) : \boldsymbol{\mu}(\mathbf{x},\hat{\mathbf{y}},t,\tau)\, d\hat{\mathbf{y}} \tag{94}$$

in which, $\mathbf{H}$ is the elastic influence function (a third-order tensor) obtained by substituting Eq. 94 into the microscale problem, and evaluating the microscale problem in the absence of damage; and $\mathbf{h}$ is the phase damage induced influence function provided by the particular solutions to the RVE problems obtained by substituting Eq. 94 into the microscale problem, and solving the microscale problem in the presence of phase damage (i.e., $\boldsymbol{\mu}$). The governing equations and the discrete approximations of the elastic and phase damage induced influence functions are provided in Ref. [46]. Meso-mechanical shape functions are employed to discretize damage and

damage induced inelastic strain fields:

$$\{\omega, \boldsymbol{\mu}\}(\mathbf{x}, \mathbf{y}, t) = \sum_{\gamma=1}^{n} N^{(\gamma)}(\mathbf{y}) \left\{\omega^{(\gamma)}, \boldsymbol{\mu}^{(\gamma)}\right\}(\mathbf{x}, t, \tau) \tag{95}$$

in which, $N^{(\gamma)}$ are the phase shape functions. We consider a partitioning of the RVE domain into n non-overlapping subdomains, $\theta^{(\gamma)}$, such that $\theta^{(\gamma)} \cap \theta^{(\Delta)} = \emptyset$ if $\gamma \neq \Delta$. The phase shape functions are taken to be piecewise constant functions forming a partition of unity within the RVE:

$$N_{\text{ph}}^{(\gamma)}(\mathbf{y}) = \begin{cases} 1 \text{ if } \mathbf{y} \in \theta^{(\gamma)} \\ 0 \text{ elsewhere} \end{cases} \tag{96}$$

and, $\omega^{(\gamma)}$ and $\boldsymbol{\mu}^{(\gamma)}$ are damage variable and inelastic strains averaged over the partition, $\theta^{(\gamma)}$. Substituting Eqs. 94-96 into the microscale problem (Eqs. 93), and considering variational arguments (see Ref. [17]), the governing equation of the microscale problem is reduced to the following algebraic form:

$$\sum_{\Delta=1}^{n} \left\{ \left[1 - \omega^{(\Delta)}\right] \left[\hat{\mathbf{A}}^{(\alpha\Delta)} : \bar{\boldsymbol{\epsilon}} + \sum_{\gamma=1}^{n} \hat{\mathbf{B}}^{(\alpha\Delta\gamma)} : \boldsymbol{\mu}^{(\gamma)} \right] \right\} = \mathbf{0} \quad \forall \alpha = 1, 2, \ldots, n \tag{97}$$

in which, $\hat{\mathbf{A}}^{(\alpha\Delta)}$ and $\hat{\mathbf{B}}^{(\alpha\Delta\gamma)}$ are coefficient tensors computed as a function of the influence functions, $\mathbf{H}$ and $\mathbf{h}$ as well as the elastic properties, $\mathbf{L}$. The expressions for $\hat{\mathbf{A}}^{(\alpha\Delta)}$ and $\hat{\mathbf{B}}^{(\alpha\Delta\gamma)}$ are found in Eqs. 35 and 37 where $(\hat{\mathbf{A}}^{(\alpha\Delta)})_{ijkl} = C_{ijkl}^{(\alpha\Delta)}$ and $(\hat{\mathbf{B}}^{(\alpha\Delta\gamma)})_{ijkl} = F_{ijkl}^{(\alpha\Delta\gamma)}$ in this case. The macroscopic stress tensor is expressed in terms of the partition average damage variable and inelastic strains as:

$$\bar{\boldsymbol{\sigma}} = \sum_{\Delta=1}^{n} \left[1 - \omega^{(\Delta)}\right] \left[\bar{\mathbf{L}}^{(\Delta)} : \bar{\boldsymbol{\epsilon}} + \sum_{\alpha=1}^{n} \bar{\mathbf{P}}^{(\Delta\alpha)} : \boldsymbol{\mu}^{(\alpha)} \right] \tag{98}$$

in which, $\bar{\mathbf{L}}^{(\Delta)}$ and $\bar{\mathbf{P}}^{(\Delta\alpha)}$ are coefficient tensors whose expressions are found in Eqs. 49-

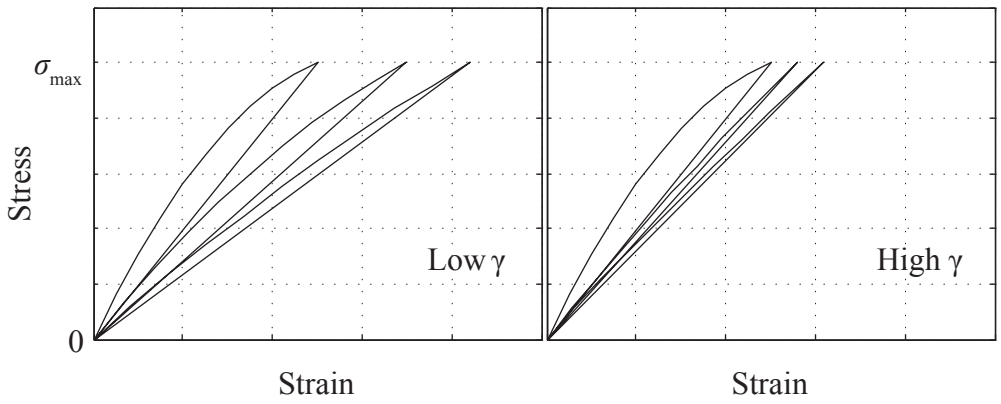

Figure 12: Effect of the cyclic damage sensitivity parameter, p, on the cyclic stress-strain relationship.

50. The macrochronological counterparts of the reduced order microscopic equilibrium and macroscopic stress are obtained by applying the almost periodic temporal homogenization operator to Eqs. 97 and 98.

3.2 Cyclic Damage Model

Continuum damage mechanics (CDM) is employed to describe the evolution of damage within a phase partition (i.e., $\omega^{(\gamma)}$). In contrast to monotonic CDM models, the evolution law is allowed to accumulate damage at subcritical loading levels to permit sensitivity to cyclic loading. Such a model previously employed in Refs. [24, 44], is adopted in this study:

$$\dot{\omega}^{(\gamma)} = g^p \frac{d\Phi\left(\upsilon^{(\gamma)}\right)}{d\upsilon^{(\gamma)}} \left\langle \dot{\upsilon}^{(\gamma)} \right\rangle_+ \quad \text{where} \quad 0 \leq g = \frac{\Phi\left(\upsilon^{(\gamma)}\right)}{\omega^{(\gamma)}} \leq 1; \quad \gamma = 1, 2, \ldots, n \tag{99}$$

where, p is the cyclic damage sensitivity parameter; $\langle \cdot \rangle_+$ denotes MacCauley brackets; Φ the damage evolution law under monotonically increasing loads; and $\upsilon^{(\gamma)}$ the damage equivalent strain:

$$\upsilon^{(\gamma)} = \sqrt{\frac{1}{2} \boldsymbol{\epsilon}^{(\gamma)} : \mathbf{L}^{(\gamma)} : \boldsymbol{\epsilon}^{(\gamma)}} \tag{100}$$

in which, $\mathbf{L}^{(\gamma)}$ is the tensor of elastic moduli of the constituent occupying $\theta^{(\gamma)}$; and, $\boldsymbol{\epsilon}^{(\gamma)}$ is the average strain within partition, γ. The damage evolution under monotonic conditions is idealized based on a smooth evolution law:

$$\Phi\left(\upsilon^{(\gamma)}\right) = \frac{\arctan\left(a^{(\gamma)}\upsilon^{(\gamma)} - b^{(\gamma)}\right) + \arctan\left(b^{(\gamma)}\right)}{\frac{\pi}{2} + \arctan\left(b^{(\gamma)}\right)} \tag{101}$$

where, $a^{(\gamma)}$ and $b^{(\gamma)}$ are material parameters associated with the constituent occupying domain $\theta^{(\gamma)}$.

The cyclic damage sensitivity parameter, p, which controls the rate of damage accumulation with respect to a load cycle as illustrated in Fig. 12, is taken to be of the form:

$$p^{(\gamma)} = c_0^{(\gamma)} + c_1^{(\gamma)}\upsilon_{\max}^{(\gamma)} + c_2^{(\gamma)}(\upsilon_{\max}^{(\gamma)})^2 \tag{102}$$

$c_0^{(\gamma)}$, $c_1^{(\gamma)}$, and $c_2^{(\gamma)}$ are parameters that account for the sensitivity of fatigue strength to the maximum applied loading. A quadratic form is chosen to model the fatigue behavior observed in the experiments. $\upsilon_{\max}^{(\gamma)}$ is the maximum value of the damage equivalent strain during the history of the material point as defined below.

$$\upsilon_{\max}^{(\gamma)}(t) = \max_{T}\left\{\upsilon^{(\gamma)}(T) \mid 0 \leq T \leq t\right\} \tag{103}$$

Applying the chain rule in the time domain (Eq. 78) to the damage evolution equation (Eq. 99), collecting the terms based on the order of the temporal scaling parameter, η, and applying the temporal homogenization operator to the $O(1)$ equation yields:

$$\omega_{,\tau}^{(\gamma)} = f^0 = g^p \frac{d\Phi\left(\upsilon^{(\gamma)}\right)}{d\upsilon^{(\gamma)}} \left\langle \upsilon_{,\tau}^{(\gamma)} \right\rangle_+ \tag{104}$$

$$\tilde{\omega}_{,t}^{(\gamma)} = f^1 = g^p \frac{d\Phi\left(\tilde{\upsilon}^{(\gamma)}\right)}{d\tilde{\upsilon}^{(\gamma)}} \left\langle \tilde{\upsilon}_{,t}^{(\gamma)} \right\rangle_+ \tag{105}$$

Microchronological Problem:
Given: Coefficient tensors, $\bar{\mathbf{L}}^{(\Delta)}$, $\bar{\mathbf{P}}^{(\Delta\alpha)}$, $\hat{\mathbf{A}}^{(\alpha\Delta)}$ and $\hat{\mathbf{B}}^{(\alpha\Delta\gamma)}$; average body force, $\bar{\mathbf{b}}$, boundary data $\hat{\mathbf{u}}$ and $\hat{\mathbf{t}}$
Find: at a fixed macrochronological time $\breve{t} \in [0, t_f]$ the macroscopic displacement field, $\bar{\mathbf{u}}$, which satisfies ($\tau \in [0, \tau_0]$):

$$\text{Equilibrium}: \quad \nabla_{\mathbf{x}} \cdot \bar{\boldsymbol{\sigma}}\left(\mathbf{x}, \breve{t}, \tau\right) + \bar{\mathbf{b}}\left(\mathbf{x}\right) = \mathbf{0}; \quad \mathbf{x} \in \Omega$$

$$\text{Constitutive Equation}: \quad \bar{\boldsymbol{\sigma}} = \sum_{\Delta=1}^{n} \left[1 - \omega^{(\Delta)}\right] \left[\bar{\mathbf{L}}^{(\Delta)} : \bar{\boldsymbol{\epsilon}} + \sum_{\alpha=1}^{n} \bar{\mathbf{P}}^{(\Delta\alpha)} : \boldsymbol{\mu}^{(\alpha)}\right]$$

$$\sum_{\Delta=1}^{n} \left\{ \left[1 - \omega^{(\Delta)}\right] \left[\hat{\mathbf{A}}^{(\alpha\Delta)} : \bar{\boldsymbol{\epsilon}} + \sum_{\gamma=1}^{n} \hat{\mathbf{B}}^{(\alpha\Delta\gamma)} : \boldsymbol{\mu}^{(\gamma)}\right] \right\} = \mathbf{0} \quad \forall \alpha = 1, 2, \ldots, n$$

$$\text{Damage Evolution}: \quad \omega_{,\tau}^{(\gamma)} = f^0 = g^p \frac{d\Phi\left(\upsilon^{(\gamma)}\right)}{d\upsilon^{(\gamma)}} \left\langle \upsilon_{,\tau}^{(\gamma)} \right\rangle_+$$

$$\text{Boundary conditions}: \quad \bar{\mathbf{u}} = \hat{\mathbf{u}}(\mathbf{x}, \breve{t}, \tau); \quad \mathbf{x} \in \Gamma_u$$

$$\bar{\boldsymbol{\sigma}} \cdot \mathbf{n} = \hat{\mathbf{t}}(\mathbf{x}, \breve{t}, \tau); \quad \mathbf{x} \in \Gamma_t$$

Box 2: The microchronological system of equations for evaluation of a single load cycle.

4 Computational Implementation

Boxes 2 and 3 summarize the microchronological- and macrochronological-reduced order multiscopic problems, respectively. Given the coupling terms, the micro- and macrochronological problems are evaluated using the nonlinear finite element method. A commercial finite element software (Abaqus) along with the user material subroutine utility (UMAT) is employed to solve these problems. In this section, we focus on the implementation details of the coupling between the micro- and macrochronological problems. The proposed solution strategy is implemented with an adaptive macrochronological time stepping methodology.

Macrochronological Problem:
Given: coefficient tensors, $\bar{\mathbf{L}}^{(\Delta)}$, $\bar{\mathbf{P}}^{(\Delta\alpha)}$, $\hat{\mathbf{A}}^{(\alpha\Delta)}$ and $\hat{\mathbf{B}}^{(\alpha\Delta\gamma)}$; average body force, $\bar{\mathbf{b}}$, boundary data, $\hat{\mathbf{u}}^0$ and $\hat{\mathbf{t}}^0$; the almost periodic damage function, ω_{ap}.
Find: the displacement field, $\tilde{\tilde{\mathbf{u}}}$, which satisfies ($t \in [0, t_f]$):

$$\text{Equilibrium}: \quad \nabla_{\mathbf{x}} \cdot \tilde{\tilde{\boldsymbol{\sigma}}}\left(\mathbf{x}, t\right) + \bar{\mathbf{b}}\left(\mathbf{x}\right) = \mathbf{0}; \quad \mathbf{x} \in \Omega$$

$$\text{Constitutive Equation}: \quad \tilde{\tilde{\boldsymbol{\sigma}}} = \sum_{\Delta=1}^{n} \left[1 - \tilde{\omega}^{(\Delta)}\right] \left[\bar{\mathbf{L}}^{(\Delta)} : \tilde{\tilde{\boldsymbol{\epsilon}}} + \sum_{\alpha=1}^{n} \bar{\mathbf{P}}^{(\Delta\alpha)} : \tilde{\boldsymbol{\mu}}^{(\alpha)}\right]$$

$$\sum_{\Delta=1}^{n} \left\{ \left[1 - \tilde{\omega}^{(\Delta)}\right] \left[\hat{\mathbf{A}}^{(\alpha\Delta)} : \bar{\boldsymbol{\epsilon}} + \sum_{\gamma=1}^{n} \hat{\mathbf{B}}^{(\alpha\Delta\gamma)} : \tilde{\boldsymbol{\mu}}^{(\gamma)}\right] \right\} = \mathbf{0} \quad \forall \alpha = 1, 2, \ldots, n$$

$$\text{Damage Evolution}: \quad \dot{\tilde{\omega}}(\mathbf{x}, t) = f^1 + \omega_{\text{ap}} = g^p \frac{d\Phi\left(\tilde{v}^{(\gamma)}\right)}{d\tilde{v}^{(\gamma)}} \left\langle \tilde{v}^{(\gamma)}_{,t} \right\rangle_+ + \omega_{\text{ap}}(\mathbf{x}, t); \quad \mathbf{y} \in \theta$$

$$\text{Boundary conditions}: \quad \tilde{\tilde{\mathbf{u}}} = \hat{\mathbf{u}}^0(\mathbf{x}, t); \quad \mathbf{x} \in \Gamma_u$$

$$\tilde{\tilde{\boldsymbol{\sigma}}}(\mathbf{x}, t) \cdot \mathbf{n} = \hat{\mathbf{t}}^0(\mathbf{x}, t); \quad \mathbf{x} \in \Gamma_t$$

Box 3: The macrochronological system of equations for evaluation of a macroscale time step.

The overall solution strategy for the evaluation of the coupled multiscale system is illustrated in Fig. 13. Consider a discretization of the macrochronological time domain, $\{t_0 = 0, \ldots, t_{i-1}, t_i, t_{i+1}, \ldots, t_k = t_f\}$ in which t_i denotes the i^{th} macrochronological time step:

$$t_i = \sum_{j=1}^{i} \Delta t_j \leq t_f \tag{106}$$

where, $\Delta t_i = t_i - t_{i-1}$ and $t_0 = 0$. A driver program (implemented in the Python programming language for compatibility with Abaqus) controls the execution of the solution procedure. At each macrochronological time step, the time step size as well as the almost periodic damage field are estimated and passed to the macrochronological - multiscopic problem, which is evaluated for macrochronological response fields. The macrochronological response fields provide the initial state of the microchronological - multiscopic problem at fixed time t_i due to the particular choice of the temporal homogenization operator. The point-wise value of the almost periodic damage field, $\omega^{(\gamma)}_{\text{ap}}$, at the current time step is computed and passed to the driver routine for

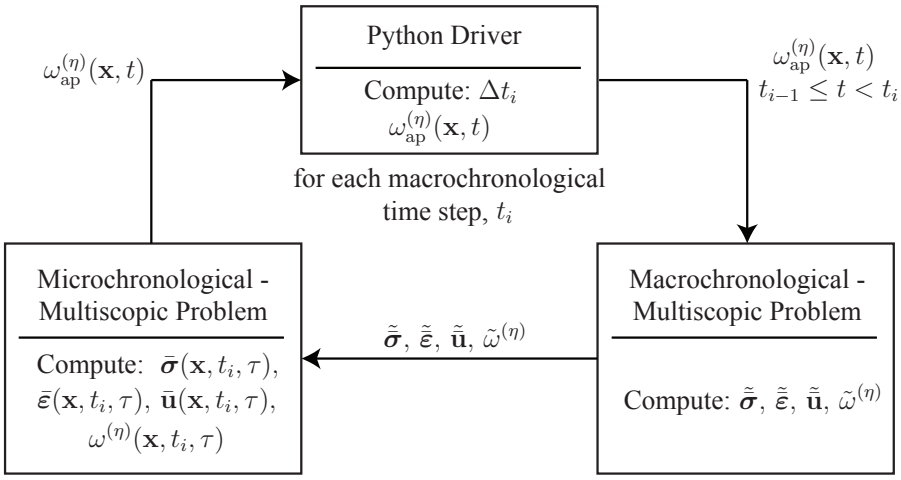

Figure 13: Implementation strategy of the coupled micro- and macro-chronological problems.

computation of the next time step size.

4.1 Adaptive Macrochronological Time Stepping

The proposed solution algorithm outlined in Fig. 13 requires the resolution of k cycles throughout the loading history, which are evaluated by the microchronological problem (Box 2). The accuracy and efficiency of the proposed approach is based on the appropriate selection of the macrochronological time steps, as well as the accurate approximation of the evolution of the almost periodic component of the damage field. In this study, the almost periodic damage fields are approximated based on a modified quadratic multistep method [13], whereas the macrochronological time step size is chosen adaptively based on a maximum damage accumulation criterion. It is assumed that damage accumulation is primarily due to cyclic loading and slow loading component remain smooth during the loading history.

Let $\mathbf{D}'(t)$ be a matrix of almost periodic damage rate fields:

$$\mathbf{D}'(t) = \begin{bmatrix} \omega_{\text{ap}}^{(1)}(\mathbf{x}_1, t) & \cdots & \omega_{\text{ap}}^{(n)}(\mathbf{x}_1, t) \\ \vdots & \ddots & \vdots \\ \omega_{\text{ap}}^{(1)}(\mathbf{x}_{n_g}, t) & \cdots & \omega_{\text{ap}}^{(n)}(\mathbf{x}_{n_g}, t) \end{bmatrix} \tag{107}$$

in which, n_g denotes the total number of integration points within the macroscopic domain; $\mathbf{x}_g$ denotes the value of the function at integration point g. Considering a smooth damage growth between macrochronological steps $i-1$ and $i+1$, the evolution of $\mathbf{D}'(t)$ is approximated by a linear function around t_i:

$$\mathbf{D}'(t_i + \Delta t) \approx \mathbf{P}_i(\Delta t) \equiv \mathbf{b}_i + \mathbf{c}_i \Delta t; \quad \Delta t \in [-\Delta t_i, \Delta t_{i+1}] \tag{108}$$

The coefficients of the linear approximations are obtained by imposing the following conditions on $\mathbf{P}_i$:

$$\mathbf{P}_i(0) = \mathbf{D}'(t_i) \tag{109}$$

$$\mathbf{P}_i(-\Delta t_i) = \mathbf{D}'(t_{i-1}) \tag{110}$$

Substituting Eqs. 109, and 110 into Eq. 108, the rate of the almost periodic damage fields is obtained as:

$$\mathbf{D}'(t_{i+1}) \approx \mathbf{P}(\Delta t_{i+1}) = \mathbf{D}'(t_i) + \frac{\Delta t_{i+1}}{\Delta t_i} \left(\mathbf{D}'(t_i) - \mathbf{D}'(t_i - 1) \right) \tag{111}$$

Let $\Delta \mathbf{D}_{i+1}$ define the matrix of cyclic loading induced damage accumulated between time t_i and t_{i+1}. Employing the linear approximation provided by Eq. 108 yields:

$$\Delta \mathbf{D}_{i+1} \approx \int_0^{\Delta t_{i+1}} \mathbf{P}_i(\Delta t) d\Delta t = \Delta t_{i+1} \mathbf{D}'(t_i) + \frac{\Delta t_{i+1}^2}{2\Delta t_i} \left(\mathbf{D}'(t_i) - \mathbf{D}'(t_i - 1) \right) \tag{112}$$

The macrochronological step size (Δt_{i+1}) is chosen such that the maximum damage accumulation within a step does not exceed a threshold value:

$$\|\Delta \mathbf{D}_{i+1}\|_{\max} \leq \Delta D_{\max} \tag{113}$$

where, $\Delta D_{\max}$ is the damage accumulation threshold, and $\|\cdot\|_{\max}$ denotes the matrix max norm.

The loss of load carrying capacity during a microchronological problem following a long macrochronological step indicates a possible underestimation of damage accumulation during the macrochronological time step. This is due to the deviation of the damage accumulation from the piecewise quadratic approximation within the time step. When failure is observed, the previous macrochronological step size is shortened, and the previous macrochronological time step is repeated. The time step shortening is repeated until desired accuracy of the time-to-failure is achieved. The overall algorithm is presented below:

1. Initialize algorithm: $i = 0$.
2. Evaluate macrochronological step (Box 3).
3. Evaluate microchronological problem at $t = 0$ (Box 2).
4. Set $i = 1$; $\Delta t_1 = \eta\tau_0$, where $\eta\tau_0$ is the duration of one load cycle; $\mathbf{D}'(t_1) = \mathbf{D}'(0)$.
5. Evaluate macrochronological step.
6. Evaluate microchronological problem at $t = t_1$.
7. Set $i = 2$
8. While $i \leq k$:
   (a) Calculate Δt_i using Eq. 113.
   (b) Calculate $\mathbf{D}'(t_i)$ using Eq. 111.
   (c) Evaluate macrochronological step.
   (d) Evaluate microchronological problem at $t = t_i$.
   (e) If {failure event & $\Delta t_i/t_i \geq tol$ }:

i. $\Delta t_i \leftarrow \max(\eta\tau_0, c\Delta t_i)$ and go to step (b).

(f) Else if {failure event & $\Delta t_i/t_i < tol$ }:

i. Structural failure: Stop algorithm.

(g) $i \leftarrow i + 1$

9. End.

The proposed algorithm is initiated by evaluating two macrochronological time steps and two microchronological problems that corresponds to the first two load cycles, noting that a single load period is denoted by $\eta\tau_0$. The almost periodic field is taken to vary linearly between the first and second load cycles, and quadratically between the remaining macrochronological time steps. $0 < c < 1$ is the step cutback factor when a failure event is detected. The failure event is defined as a loss of load carrying capacity of the structure, detected as lack of convergence that occurs during the evaluation of the microchronological problem. The macrochronological time step size cannot be smaller than a single load period ($= \eta\tau_0$). Structural failure is taken to occur when the failure event is detected, and the ratio of the current macrochronological time step size and the current macrochronological time is less than a specified tolerance (tol) value. The cutback iterations when a failure event is detected are controlled by the Python driver program, which employs the restart capability of Abaqus to iterate the evaluation of macro- and micro-chronological problems until convergence.

4.2 Improved Adaptive Stepping Criterion

An improved adaptive step size criterion can be developed by considering adaptive Runge-Kutta methods used in solving initial value problems. Adaptive Runge-Kutta methods estimate the truncation error by comparing an order n method to an order $n-1$ method while adapting the step size according to this estimate. In similar manner, we consider a smooth damage growth between macrochronological steps i

and $i+1$ of one order less than Eq. 108 (i.e. a constant function).

$$\mathbf{D}'(t_i + \Delta t) \approx \mathbf{P}_i(\Delta t) \equiv \mathbf{b}_i; \quad \Delta t \in [0, \Delta t_{i+1}) \tag{114}$$

$\mathbf{b}_i$ is attained by imposing Eq. 109 on Eq. 114.

$$\mathbf{P}_i(0) = \mathbf{D}'(t_i) = \mathbf{b}_i \tag{115}$$

We reach an expression for $\mathbf{P}_i$.

$$\mathbf{P}_i(\Delta t) = \mathbf{D}'(t_i) \tag{116}$$

In parallel with Eq. 112, the matrix of cyclic loading induced damage accumulated between times t_i and t_{i+1} is approximated by integrating Eq. 116 from 0 to Δt_{i+1}.

$$\Delta \mathbf{D}_{i+1} \approx \int_0^{\Delta t_{i+1}} \mathbf{P}_i(\Delta t)\, \mathrm{d}\Delta t = \mathbf{D}'(t_i)\Delta t_{i+1} \tag{117}$$

Let $\Delta \mathbf{D}^2_{i+1}$ be the second order approximation to $\Delta \mathbf{D}_{i+1}$ in Eq. 112 and $\Delta \mathbf{D}^1_{i+1}$ be the order one approximation of $\Delta \mathbf{D}_{i+1}$ in Eq. 117. The step size is adaptively chosen so that the difference between $\Delta \mathbf{D}^2_{i+1}$ and $\Delta \mathbf{D}^1_{i+1}$ is less or equal to a tolerance denoted tol.

$$\mathrm{tol} \geq \left\| \Delta \mathbf{D}^2_{i+1} - \Delta \mathbf{D}^1_{i+1} \right\|_{\max} = \frac{\Delta t^2_{i+1}}{2\Delta t_i} \left\| \mathbf{D}'(t_i) - \mathbf{D}'(t_{i-1}) \right\|_{\max} \tag{118}$$

Assuming equality in Eq. 118, a closed form expression is reached for the step size Δt_{i+1}.

$$\Delta t_{i+1} = \sqrt{\frac{2\,\mathrm{tol}\,\Delta t_i}{\left\| \mathbf{D}'(t_i) - \mathbf{D}'(t_{i-1}) \right\|_{\max}}} \tag{119}$$

To utilize the new adaptive stepping criterion within the previously stated algorithm, replace Eq. 113 in step 8a with Eq. 119. Eq. 119 is ill-defined if $\left\| \mathbf{D}'(t_i) - \mathbf{D}'(t_{i-1}) \right\|_{\max} = 0$. Therefore, if $\left\| \mathbf{D}'(t_i) - \mathbf{D}'(t_{i-1}) \right\|_{\max} < \varepsilon$, Eq. 113 is solved instead to determine

Δt_{i+1}. ε is a small numerical parameter.

5 Model Verification

The proposed adaptive macrochronological time stepping strategy is verified by comparing the performance with direct cycle-by-cycle simulations. In the direct cycle-by-cycle analysis, each load cycle throughout the loading is resolved, without resorting to the multiple temporal scale strategy. The simulations were conducted on a unidirectionally fiber-reinforced matrix unit cell. The fiber is taken to remain elastic throughout the loading period, whereas the damage accumulates within the matrix as a function of loading cycles. The failure response in the matrix phase is approximated using a 4-partition reduced-order model. A uniform tensile strain is applied transverse to the reinforcement direction. The strain amplitude is varied between zero and the maximum strain throughout the loading history.

Figure 14 illustrates the variation of the damage variables within the unit cell as a function of applied loading cycles. Only two of the four matrix partitions show appreciable damage. The proposed model simulations are conducted by setting $\Delta D_{\max}$ = 0.5%, 1%, and 2%. A cutback factor of 0.5 is employed ($c = 0.5$). The proposed adaptive time stepping strategy required 109, 68, and 43 resolved microchronological load cycles for $\Delta D_{\max}$ = 0.5%, 1%, and 2%, respectively, compared to 900 cycles resolved in the direct cycle-by-cycle approach. The proposed model captures the failure response with reasonable accuracy, with excellent accuracy observed for $\Delta D_{\max}$ = 0.5%.

The efficiency of the proposed approach is further illustrated by conducting simulations when the unit cell is subjected to a slightly smaller loading amplitude . In this analysis, the cycle-to-failure of the first partition is 677 (in contrast to 377 of the previous simulations). The simulations are conducted for 1800 cycles. Figure 15 illustrates the variation of damage variables within the unit cell as a function of applied loading

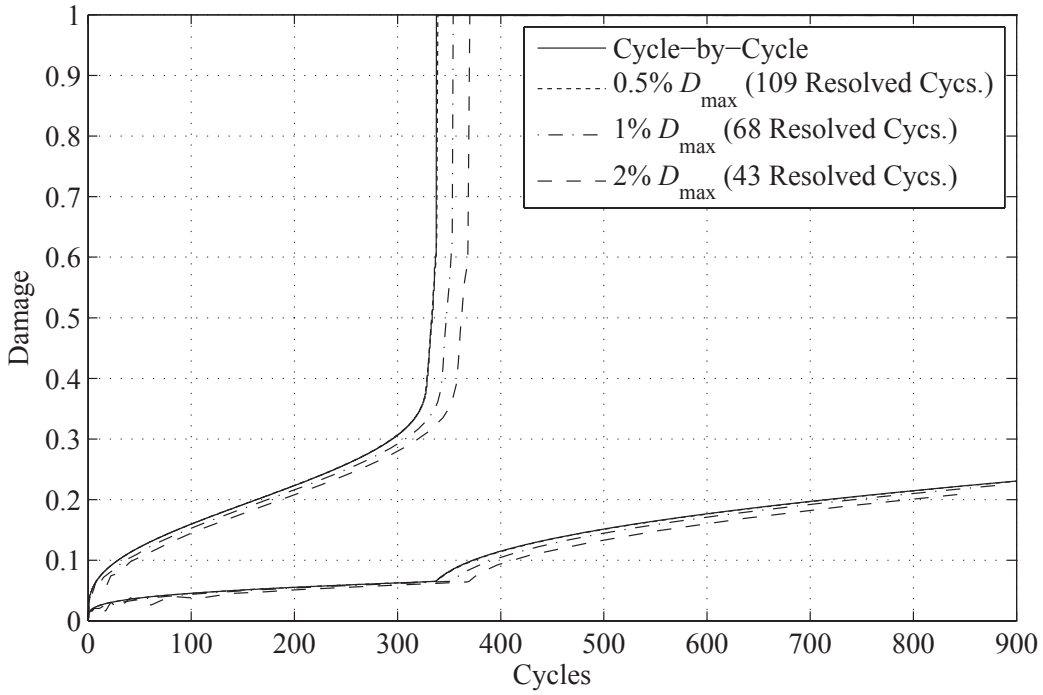

Figure 14: Comparison of the cyclic damage accumulation computed using the direct cycle-by-cycle approach and proposed multiscale model with adaptive time stepping.

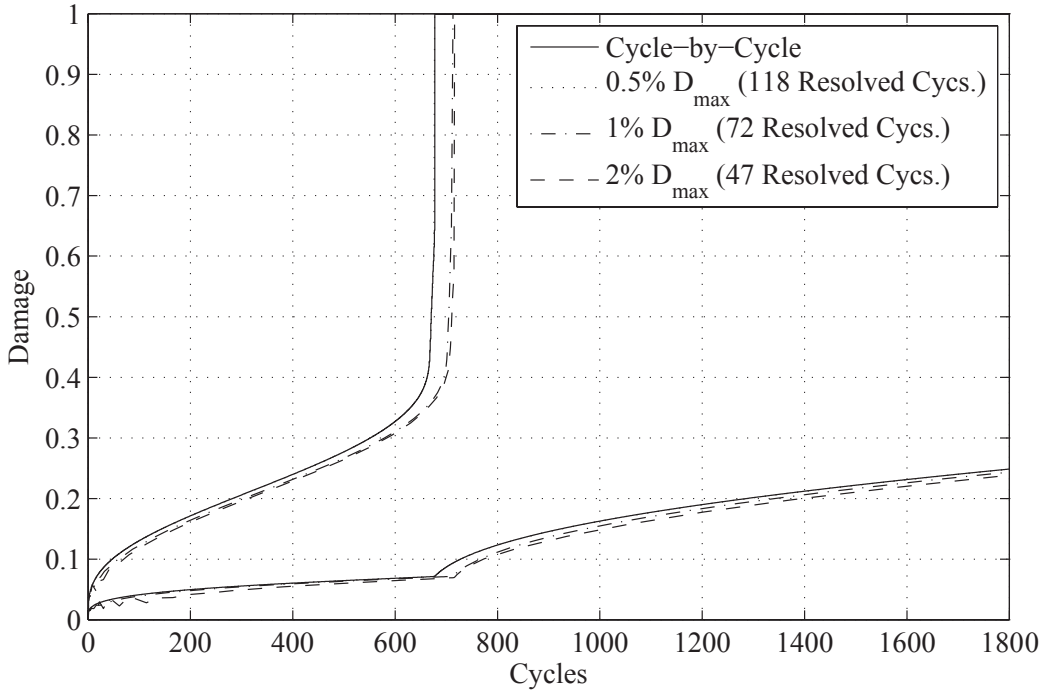

Figure 15: Comparison of the cyclic damage accumulation computed using the direct cycle-by-cycle approach and proposed multiscale model with adaptive time stepping with smaller loading amplitude.

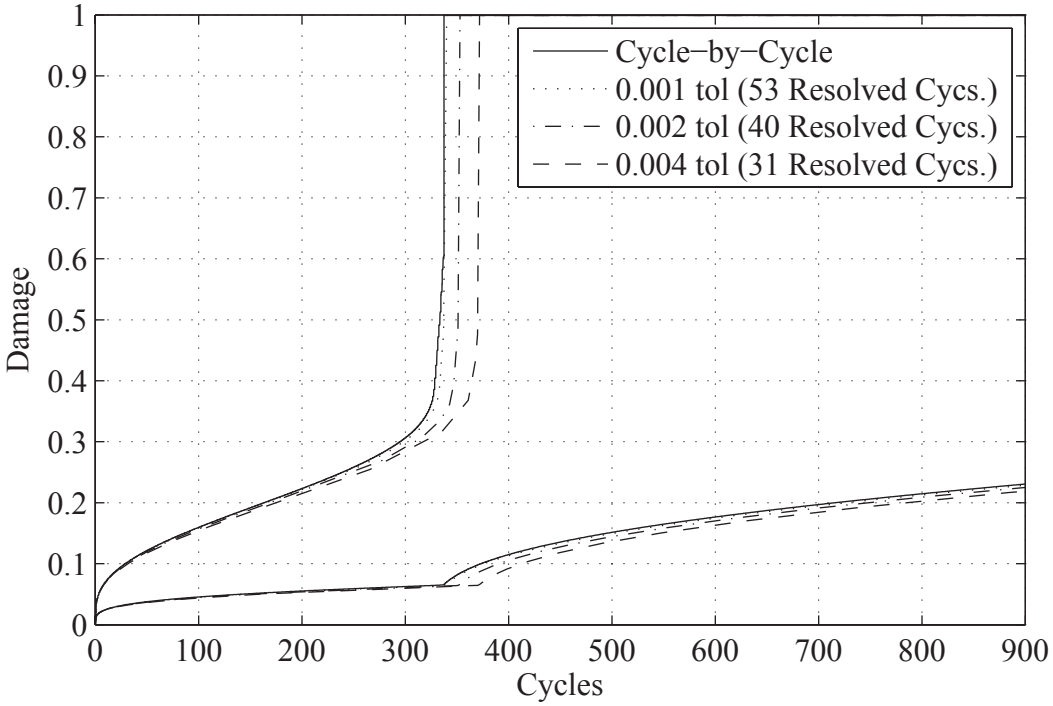

Figure 16: Comparison of the cyclic damage accumulation computed using the direct cycle-by-cycle approach and the multiscale model with improved adaptive time stepping.

cycles as computed by the reference simulations and the multiple spatio-temporal model with adaptive time stepping methodology. The total resolved cycles of the proposed adaptive time stepping strategy remain largely the same ($\Delta D_{\max} = 0.5\%$, 1%, and 2% are 118, 72 and 47 respectively), pointing to significant computational advantage in high cycle failure conditions.

5.1 Improved Adaptive Stepping Criterion Verification

In Fig. 16, the improved adaptive stepping criterion is verified by comparing three different values of tol to a direct cycle-by-cycle simulation for the same loading case used in Fig. 14. The three values of tol were chosen to produce similar accuracy to the three values of $\Delta D_{\max}$ in Fig. 14 (i.e. 0.5%, 1%, and 2%). The selected tol values were 0.001, 0.002, and 0.004, respectively. When comparing the new adaptive time stepping criterion with tol = 0.001 to $\Delta D_{\max} = 0.5\%$, the same accuracy was maintained while

resolving only 53 loading cycles as compared to resolving 109 loading cycles with the previous adaptive stepping criterion, a significant computational savings.

6 Cyclic Response of IM7/977-3 Composites

The capabilities of the proposed multiple spatio-temporal methodology are assessed through the investigation of graphite fiber-reinforced epoxy composites (i.e., IM7/977-3) subjected to cyclic loading. This section presents the experiments conducted to study the cyclic response of the composite; calibration of the model parameters based on monotonic and cyclic experiments, and; validation of model predictions based on acoustic emission testing.

6.1 Experiments

A suite of experiments was conducted to calibrate the material parameters and assess the validity of the proposed multiscale model. Composite specimens with three separate layups of unidirectional laminae were tested under uniaxial monotonic and cyclic loading conditions: (a) Zero degree specimens consist of eight unidirectional plies with fibers oriented parallel to the loading direction; (b) Ninety degree specimens consist of sixteen unidirectional plies with the fibers oriented perpendicular to the loading direction; and (c) Quasi-isotropic specimens with the layup of $[+45, 0, -45, 90]_{2s}$. Specimen configurations are summarized in Table 2. The mean fiber volume fraction of the specimens is 65.6%, which was determined based on acid digestion testing. The results of experiments conducted on zero and ninety degree specimens are employed in the calibration of the parameters of the proposed multiscale model, whereas the quasi-isotropic specimens are employed in the validation analyses.

Acoustic emission (AE) was used to detect failure events within the quasi-isotropic layups. In-situ AE activity was recorded on a Micro-II Digital AE System produced by Physical Acoustics Corporation. In the AE technique, the stress waves produced

Table 1: IM7/977-3 specimen dimensions

Fiber Orientation	Number Of Plies	Length [mm]	Width [mm]	Thickness [mm]
0°	8	250	13	1
90°	16	177	25	2
Quasi-Iso.	16	250	25	2

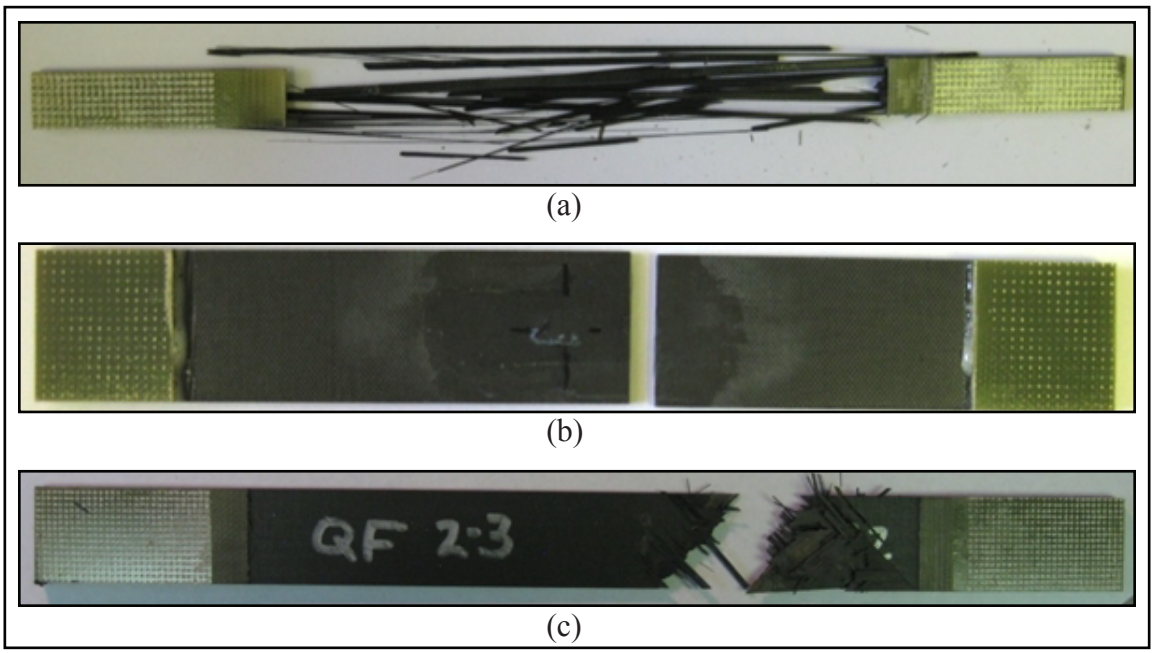

Figure 17: Failure profiles when subjected to monotonic loading. (a) Zero-degree specimens; (b) ninety degree specimens; (c) quasi-isotropic specimens.

by the sudden release of strain energy during localized failure events are identified and recorded as *hits*. Appropriate signal conditioning parameters are identified based on an AE calibration study prior to testing. A threshold wave amplitude of 48 dB enables the separation of all valid failure events from ambient noise.

The first set of experiments conducted is on unidirectional unnotched tension specimens tested under monotonic displacement control on an MTS universal testing machine according to ASTM Standard D3039 [3]. A grip pressure of 500 psi was applied to prevent slipping without crushing the composite. One axial and one transverse strain gage were mounted on each specimen to determine Poisson's ratio. A one-inch extensometer was used to accurately measure the axial stiffness. All mono-

Table 2: Calibrated elastic parameters of the composite constituents; observed and simulated elastic parameters of the overall composite.

Layup	Young's Modulus, E [GPa]	Failure Strength, σ_f [MPa]
0°	158 (13)[1]	2,841 (296)
90°	8.644 (0.712)	63 (14)
Quasi-isotropic	60.7 (2.2)	872 (30)

[1] standard deviation in parantheses.

tonic tests were conducted at a constant displacement rate of 1.27 mm/min. Thirteen zero degree specimens, seventeen ninety degree specimens, and seven quasi-isotropic specimens were subjected to uniaxial tension up to failure to ensure repeatibility. A moderate degree of modulus and strength scatter is observed in the experiments. Figure 17 illustrates the failure patterns, which show destructive fiber failure in the zero degree specimens, matrix-dominated failure in the ninety degree specimens, and combined matrix and fiber failure in the quasi-isotropic specimens. All non-zero plies in the quasi-isotropic specimens showed matrix-dominated failure, while the zero degree plies showed fiber failure. The elastic and strength properties observed in the experiments are summarized in Table 2. A Poisson's ratio of 0.316 with a standard deviation of 0.039 was observed by placing a strain gage perpendicular to the loading on the 0° specimens. The shear modulus, G_{12}, was determined to be 4.66 MPa with a standard deviation of 0.61 using additional tension experiments conducted on composite specimens with a +/-45° layup according to the procedure described in ASTM D3518 [5].

The next set of experiments consisted of constant amplitude load-controlled cyclic tests that were conducted according to ASTM D3479 [4]. Cyclic testing was performed with a constant maximum stress amplitude, an R-ratio of 0.1, and a loading frequency of 5 Hz. The maximum applied stress amplitude for the 90° specimens was varied between 45% and 55% of the average monotonic ultimate stress of the layup configuration. The 90° specimens failed by matrix cracking across the width of

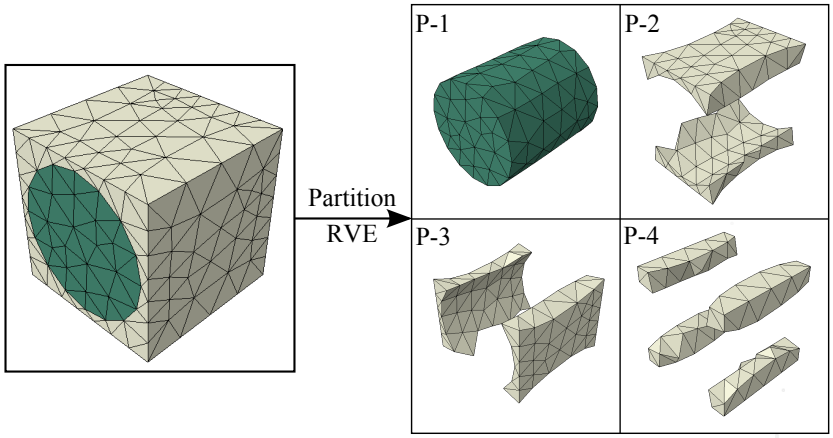

Figure 18: RVE and partition structure for IM7/977-3.

the specimen. The quasi-isotropic layup was tested with a maximum applied stress amplitude of 17% of the ultimate stress of the corresponding layup.

6.2 Model Calibration

The domain of the microscopic problem (i.e., RVE) is a unidirectionally fiber reinforced matrix as illustrated in Fig. 18. The diameter of the fiber is set to ensure that the volume fraction in the RVE equals the experimentally measured volume fraction of 65.6%. We employ a 4-partition reduced order model to evaluate the failure response within the composite constituents. The matrix is represented using three partitions, whereas the fiber response is idealized using a single partition. The domains of each partition within the RVE are illustrated in Fig. 18.

The elastic response of the 977-3 resin is taken to be isotropic, with the Young's modulus and the Poisson's ratio of the material denoted by E^{m} and ν^{m}, respectively. The IM7 fiber is taken to be transversely isotropic with five elastic parameters: E_1^{f}, E_2^{f}, G_{12}^{f}, ν_{12}^{f}, and ν_{23}^{f}, where the 1-direction is along the fiber length. The Poisson's ratios were obtained from the literature (ν_{12}^{f} and ν_{23}^{f} from [12] and ν^{m} from [31]). The remaining elastic parameters (i.e., E_1^{f}, E_2^{f}, G_{12}^{f}, and E^{m}) were calibrated against the linear regions of the stress-strain curves recorded in the monotonic experiments. The

Table 3: Elastic parameter optimization

E^{m} [GPa]	E_1^{f} [GPa]	E_2^{f} [GPa]	G_{12}^{f} [GPa]	ν^{m}	ν_{12}^{f}	ν_{23}^{f}
3.55	263.00	13.00	27.50	0.35	0.32	0.20
	E_1^{c} [GPa]	E_2^{c} [GPa]	G_{12}^{c} [GPa]	ν_{12}^{c}		
Experiment	158.00	8.64	4.66	0.316		
Model	158.00	8.64	4.66	0.33		

Superscript c indicates a composite material property.

calibrated elastic parameters of the composite constituents and the experimentally observed and simulated elastic parameters of the overall composite are summarized in Table 3.

The damage model employed in this study includes seven parameters. Four of the seven parameters (i.e., α^{m}, β^{m}, α^{f}, and β^{f}) determine the evolution of damage when subjected to monotonic loading conditions, whereas the remaining three parameters (i.e., c_0^{m}, c_1^{m} and c_2^{m}) determine the sensitivity of damage evolution to cyclic loading. Experiments conducted under cyclic tensile conditions indicate that failure initiates within the matrix. Fibers are taken to be insensitive to cyclic failure at the loading amplitudes considered in this work. The superscripts m and f denote matrix and fiber phases respectively. The matrix parameters are employed in modeling failure in the three matrix partitions, whereas the fiber parameters are employed in modeling the fiber partition.

α^{m} and α^{f} are regularization parameters that control the abruptness of the ultimate failure within the matrix and fiber phases, respectively. The values of α^{m} and α^{f} are chosen to avoid numerical difficulties associated with sudden failure events, while accurately capturing the characteristics of the stress-strain response. β^{m} and β^{f} are material parameters that control the ultimate strength of the matrix and fiber, respectively. The experimentally observed stress-strain response of the zero and ninety degree specimens are employed in the calibration process. The failure in the zero degree specimens is dominated by fiber failure, whereas matrix cracking dominates

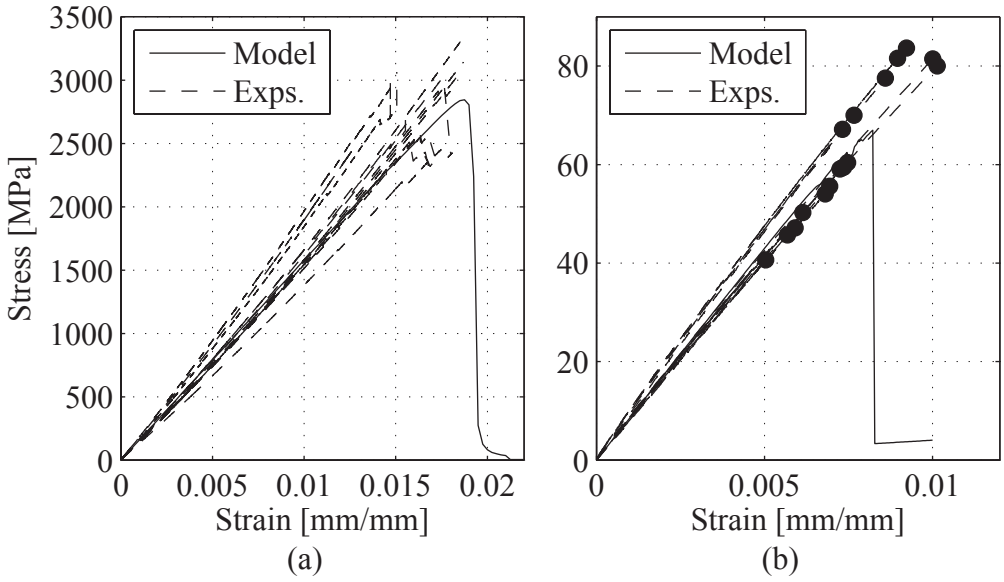

Figure 19: The tension experiments are compared to the calibrated model response.

failure in the ninety degree specimens subjected to monotonic loading. β^{m} and β^{f} are identified by minimizing the discrepancy between the experimental and simulated stress-strain curves. The calibrated model parameters are $\alpha^{\mathrm{m}} = 0.05$, $\beta^{\mathrm{m}} = 32.0$, $\alpha^{\mathrm{f}} = 0.05$, and $\beta^{\mathrm{f}} = 340.0$. Figure 19 illustrates the experimentally observed and simulated stress-strain curves based on calibrated material parameters for zero degree and ninety-degree specimens. The mean ultimate strength and strain-at-failure for zero degree specimens based on experiments are 2841 MPa and 0.0180, respectively. The mean ultimate strength and strain-at-failure for ninety degree specimens based on experiments are 63 MPa and 0.00728, respectively. The calibrated model yields 2846 MPa and 0.0186 for zero degree loadings and 67 MPa and 0.00822 for ninety degree loadings, which are in close agreement with the experiments.

The cyclic failure of the matrix is characterized by the three remaining parameters: c_0^{m}, c_1^{m} and c_2^{m}. The calibration of the cyclic loading sensitivity parameters is conducted by employing the stress-life curves obtained from experiments in which ninety degree specimens are subjected to cyclic loading in the tensile direction. In the experiments, the maximum amplitude of the cyclic loading was varied between 360 MPa

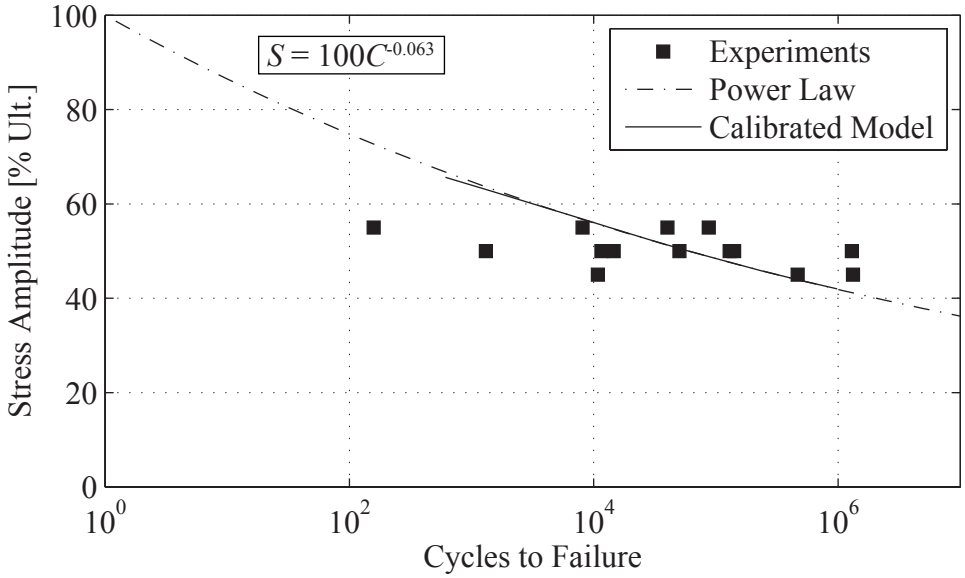

Figure 20: Experimentally observed and simulated stress-life curves of the ninety degree specimens.

and 520 MPa, while keeping the R-ratio constant (=0.1). The three parameters are calibrated by minimizing the discrepancy between the experimental and simulated cycles to failure under three different loading amplitudes. A least squares nonlinear optimization algorithm is employed in the identification of the optimal parameters. The calibrated values of c_0, c_1, and c_2 are 8.243, -2.227×10^{-2}, and 2.192×10^{-5}, respectively. Figure 20 illustrates the experimentally observed and simulated life curves. The calibrated model is in close agreement with the experimentally observed mean stress-life curve, which is expressed in terms of a power law fit. We note that the experiments display a substantial scatter around the power law fit for this material.

6.3 Model Validation

The capabilities of the proposed multiple spatio-temporal modeling approach are validated by comparing the predictions of the calibrated model with experiments conducted on quasi-isotropic specimens subjected to monotonic and cyclic loading conditions. A quarter of the specimen geometry is discretized due to symmetry with top eight plies explicitly modeled.

Figure 21 illustrates the experimental and simulated stress-strain response of the quasi-isotropic specimens subjected to monotonic tensile loading. The experimentally-observed mean strength and strain-to-failure are 872 MPa and 0.0144, respectively. The proposed multiscale model predictions of the strength and strain-to-failure are 872 MPa and 0.0151, which are in excellent agreement with each other. The simulations revealed progressive failure within the matrix of individual off-axis plies as a function of loading. The ultimate failure is due to fiber failure in the 0° plies. The predicted failure pattern is in close agreement with the experimental observations. Figure 22 shows the results of the acoustic emission testing of a monotonically loaded specimen in terms of hits as a function of applied stress magnitude. The acoustic emission data shown is indicative of the response of a typical specimen. The distinct failure events predicted by our simulations are indicated as well. The orientation of the ply in which the failure event occurs is also shown in Figure 22. All of the failure events were in the matrix with the exception of the final event. Since the proposed multiscale model is calibrated to the mean response of all specimens, the provided comparison is qualitative. Despite variations, the progressive nature of the matrix damage accumulation, as well as the initiation of damage is well captured by the proposed multiscale model.

We further assessed the validity of the proposed model by comparing the model predictions to experiments on quasi-isotropic specimens subjected to cyclic loading conditions. A sinusoidal load with a peak magnitude of 17% of the mean ultimate failure load of the quasi-isotropic specimens (872 MPa) and an R-ratio of 0.1 is applied. The objective of the investigation is to assess the capability of the proposed model in capturing the distinct failure events that occur within the matrix material as a function of the applied load cycles. In our simulations, the first four distinct failure events occurred at 11766, 27794, 38817 and 46694 cycles, respectively. Each of these failure events was an individual off-axis ply losing load carrying capacity due

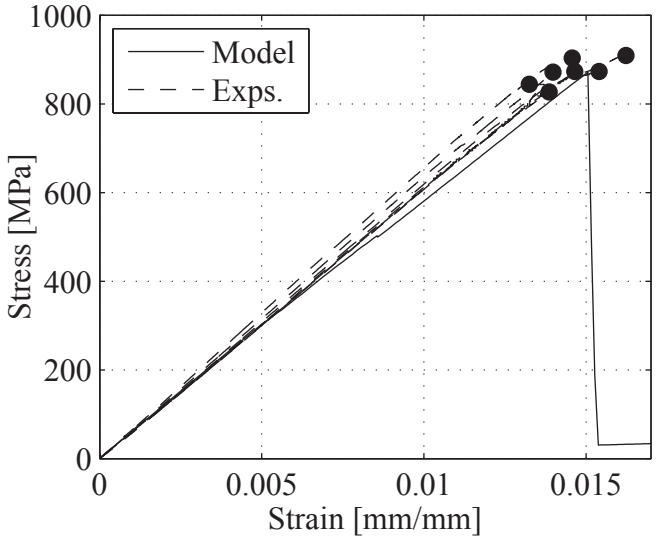

Figure 21: Comparison of experimental and predicted stress-strain curves of the quasi-isotropic specimens subjected to monotonic tensile loading.

to a matrix crack extending the entire width of the specimen. The first failure event was in a ninety degree ply, the second and third events were in fourty-five degree plies, and the fourth event was in a minus fourty-five degree ply. Figure 23a shows the acoustic emission testing results in terms of total hits as a function of the number of loading cycles. The failure events predicted by the proposed multiscale model are indicated in Fig. 23a. Figure 23b plots the numerical derivative of total hits with respect to the total number of accumulated load cycles. The figures illustrate that the time-to-failure for major recorded failure events coincide with those predicted by the simulations. Despite close correlation with the acoustic emission testing, the predictive capability of the proposed model is qualitative. Additional experimental investigations that quantitatively link the failure events that occur during the cyclic loading are needed to fully assess the validity of the proposed approach.

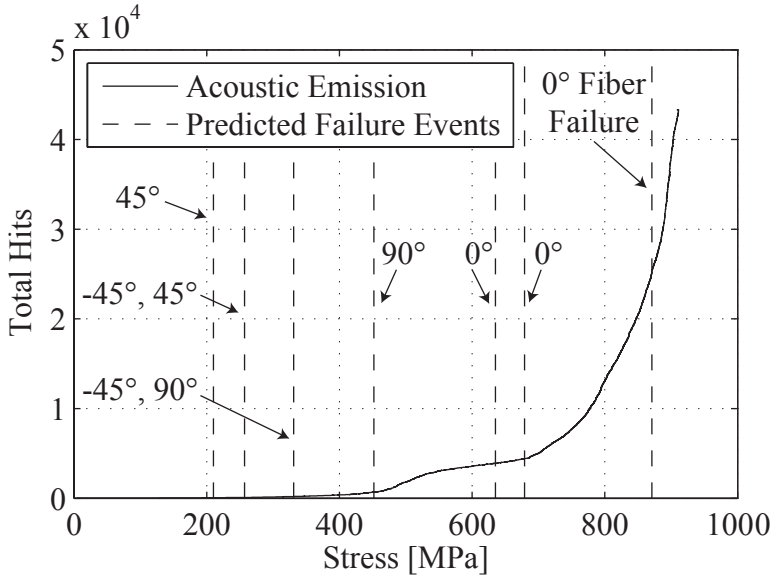

Figure 22: Predicted failure events compared to acoustic emission data of a quasi-isotropic specimen subjected to monotonic tensile loading. The ply in which the failure occurs is indicated. All predicted failure events are in the matrix unless indicated otherwise.

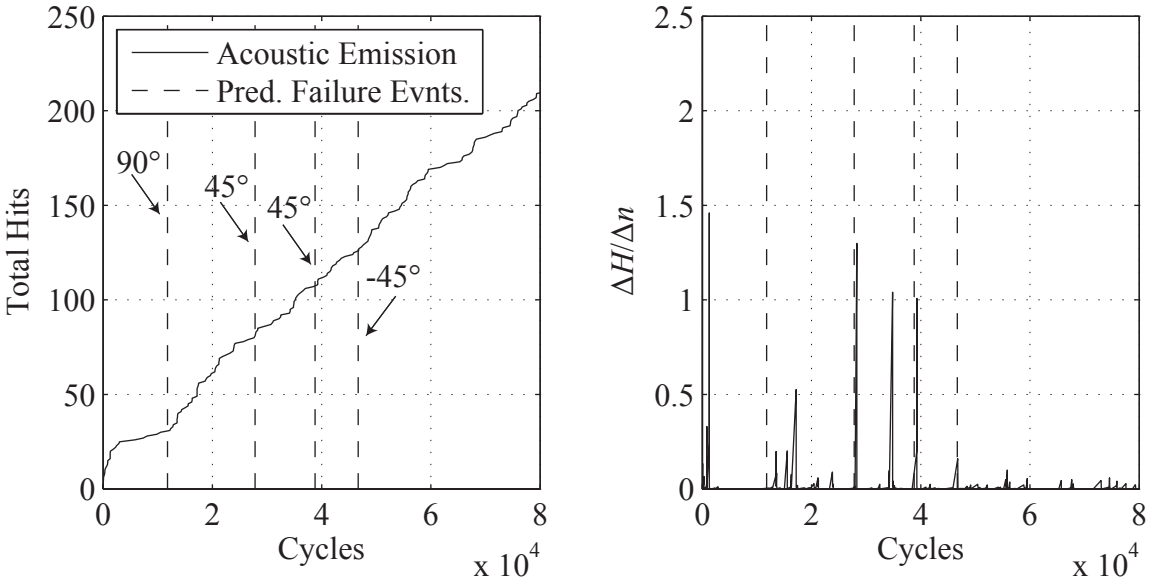

Figure 23: Predicted failure events compared to acoustic emission data of a quasi-isotropic specimen subjected to cyclic loading. (a) Hits vs. loading cycles; (b) numerical derivative of hits vs. loading cycles.

CHAPTER 4

EXPERIMENTAL AND COMPUTATIONAL INVESTIGATION OF PROGRESSIVE DAMAGE ACCUMULATION IN CFRP COMPOSITES

1 Introduction

Damage and failure prediction cannot be achieved using computational modeling alone since such models rely on experiments for parameter calibration and validation. Several in-situ and post-mortem nondestructive inspection (NDI) methods, such as acoustic emission testing (AE), X-ray radiography, and X-ray computed tomography (CT), are instrumental in characterizing some aspects of damage progression and model validation. AE uses piezoelectric sensors to passively detect acoustic signals emitted by the material during damage propagation [34, 49]. The most advantageous characteristic of AE is that the sensors detect damage during testing in a range that cannot be distinguished by typical instrumentation such as load cells, strain gauges, and displacement transducers. X-ray radiography is a common NDI method, in which a two dimensional image is recorded on an imaging plate as energy is passed through a stationary material [56, 61]. In-plane delaminations can be easily detected due to the variation of X-ray absorption between the material and the void. The difficulty with X-ray radiography is the inability to characterize damage as a function of specimen thickness. X-ray computed tomography provides an ultra-high resolution three dimensional image through the thickness of a material [57]. As X-ray CT equipment has become more readily available, this technique is being used for nondestructive evaluation of composites [54]. The primary advantage of X-ray CT for composite materials is that delaminations, transverse matrix cracks, and fiber fracture can all

be adequately characterized [18, 59].

This chapter presents a two-part study on the progressive damage accumulation in carbon fiber reinforced polymer (CFRP) composites. The first part details failure under monotonic loading conditions. The second part of the study addresses fatigue loadings. A multiscale computational homogenization model [17] is employed to numerically characterize the progressive damage mechanisms of fiber fracture, matrix cracking, and delaminations as a function of loading. An experimental program using the combination of AE, X-ray radiography and X-ray CT techniques are employed to experimentally characterize the progression of damage throughout the loading history and assess the validity of the model predictions. A key contribution is that the sequencing and rate of failure at each ply of laminated composite specimens up to the sub-microstructure scale are established based on the combined experimental and computational investigation.

The remainder of this chapter is organized as follows: Section 4.2 details the experimental program including the material fabrication, testing procedures and the NDI methods. Section 4.3 describes the investigation of monotonic loads. Section 4.4 presents the investigation of fatigue loadings.

2 Experimental Procedures

A series of monotonic and fatigue tension tests were conducted on the graphite fiber reinforced epoxy, IM7/977-3. In-situ acoustic emission monitoring was conducted in order to characterize damage propagation with increasing load. X-ray radiography and X-ray computed tomography were used periodically to visually inspect the type, location, and extent of internal damage.

2.1 Material Fabrication

Quasi-isotropic panels were hand laid from unidirectional preimpregnated IM7/977-3 graphite epoxy. They were cured in an autoclave at a temperature of 177°C and a pressure of 689 kPa. After cure, the panels were cut into multiple test specimens with nominal dimensions of 25.4 mm x 2 mm x 254 mm. The specimens consisted of 16 plies with $[+45, 0, -45, 90]_{2s}$ layup. The mean and standard deviation of the fiber volume fraction were determined to be 66.6% and 2.5%, respectively, by acid digestion testing.

2.2 Testing

Two sets of monotonic tension tests were conducted on an MTS universal testing machine according to ASTM D3039 [3]. The first set was conducted at a constant displacement rate of 1.27 mm/min to obtain the average mechanical properties of 0° and 90° unidirectional composite specimens. The second set of tests was conducted on a quasi-isotropic specimen in order to thoroughly characterize the quantity and location of damage progression as a function of load. The specimen was instrumented with one 25 mm extensometer and two piezoelectric acoustic emission sensors. The specimen was loaded and unloaded six times (at 300 MPa, 400 MPa, 620 MPa, 710 MPa, 845 MPa and failure) such that each loading was higher in magnitude than the previous loadings. Non-destructive imaging was used to evaluate the damage accumulation after each loading. The final loading caused complete failure of the specimen. A low displacement rate of 0.127 mm/min was used to better capture acoustic emission events as a function of time.

Tension tests with fatigue loading were conducted on an MTS universal testing machine according to ASTM D3479 [4]. The tests were conducted on three quasi-isotropic specimens in order to thoroughly characterize the quantity and location of damage progression as a function of the number of loading cycles. The tests were

conducted at a loading frequency of 5 Hz, an r-ratio of 0.1, and a maximum stress amplitude of 143 MPa. 143 MPa is 18% of the maximum strength (795 MPa) of an independently tested quasi-isotropic specimen.

2.3 Acoustic Emission

Acoustic emission (AE) testing was used to detect failure events within the composite material. In-situ AE activity was recorded on a Micro-II Digital AE System produced by Physical Acoustics Corporation. When a material experiences local failure, it releases strain energy which produces a stress wave in the specimen. The AE system detects this acoustic energy and records it as a *hit*. Prior to testing, an AE calibration study was performed to define the appropriate signal conditioning parameters. It was found that an amplitude threshold of 48 dB enabled the detection of all valid material failure events without recording ambient noise. As recommended by the equipment manufacturer, the AE timing parameters used for this study were Peak Definition Time = 400 μs, Hit Definition Time = 800 μs, Hit Lockout Time = 200 μs, and Maximum Duration = 100 ms.

2.4 X-ray Radiography

The monotonically loaded quasi-isotropic specimen was loaded to ultimate failure in increments. Once each load level was achieved, the specimen was unloaded and examined using a 160 kV Philips X-ray system (0.4 mm focal spot) and General Electric CR Tower Computed Radiography system using IPS imaging plates and 50 micron sampling. The imaging parameters were 26 kV, 3 mA, and 30 s, with a source-to-detector distance of 48 inches. Prior to X-ray examination, the edges of the specimen were exposed to zinc iodide, an opaque penetrant, which was absorbed into all cracks and voids adjacent to the specimen edge. The optimum view of damage was achieved using the General Electric Rhythm image processing software where a level

III contrast enhancement filter was applied to each X-ray image using noise reduction and latitude correction.

X-ray radiography was also used to evaluate the state of damage accumulation for the fatigue loadings at 1500, 25000, 50000, and 100000 loading cycles. Once the chosen number of loading cycles was reached, the specimen was removed from the tensile testing machine and examined using the Philips X-ray system with the previously described procedures and settings.

2.5 X-ray Computed Tomography

For the monotonically loaded specimens, once the planar X-ray showed a significant amount of damage, the specimen was also examined using an X-Tek HMX160 CT system. The main components included an X-ray source, a rotation stage on which the sample was fixed, and an X-ray detector. The maximum resolution, at highest magnification, was approximately 5 μm. A Molybdenum target was used. The source voltage and the source current were 90 kV and 90 μA, respectively. The specimen was clamped vertically approximately 33 cm from the X-ray source. The sample translates and rotates over 360° with a step size of 0.5°. Averages of eight projection images (1024 x 1024 pixels) were collected at each position. The raw image data was reconstructed using CT Pro software. A three dimensional structure of the damaged specimen was visualized in order to evaluate the damage through the thickness of the specimen using 3D surface rendering techniques.

3 Investigation of CFRP Composites Under Monotonic Loadings

3.1 Computational Model

The geometry, finite element discretization, and boundary conditions considered in the macroscale specimen model are illustrated in Fig. 24. The length, width, and thickness of the numerical model were 6 mm, 25 mm, and 1 mm, respectively. The

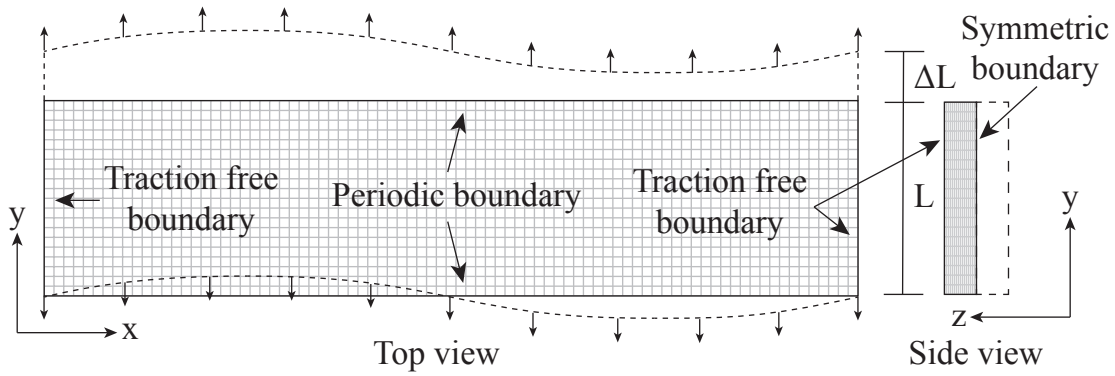

Figure 24: Quasi-isotropic virtual specimen.

discretization of the model consisted of 26,560 trilinear hexahedral elements. Each ply was explicitly modeled along the thickness direction with 16 elements discretizing the thickness of the specimen layup. Only the top half of the specimen was discretized due to symmetry of the specimen. A small part of the specimen along the length (L=6 mm) was modeled to reduce the computational cost of the failure simulation. Periodic boundary conditions were imposed along the y-direction to eliminate spurious boundary effects due to submodeling. The numerical specimen was chosen long enough to avoid the interaction of damage effects between the top and bottom edges. The specimen was loaded by increasing the average distance between the top and bottom edges using constraints. The magnitude of the applied stress was taken to be the total constraint force required to maintain the specified average distance between the specimen ends divided by the cross sectional area of the specimen.

3.2 Multiscale Failure Modeling

Computational homogenization (CH) with multiple spatial scales [32] was used to model the mechanical response and failure in the composite specimens. In the computational homogenization method the constitutive response at the material point of a macroscopic (i.e. specimen) model is provided by numerically evaluating a microscale model of the representative volume or a unit cell of the composite. Spatial

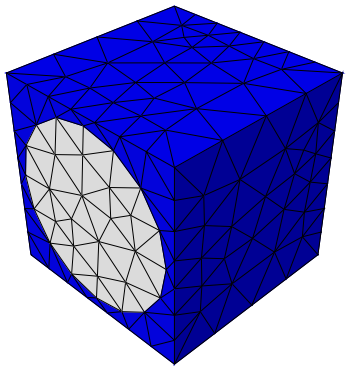

Figure 25: The unit cell for IM7/977-3 with 66% fiber volume fraction.

averaging (i.e. homogenization) of the microscale response yields the constitutive relationship between macroscopic stress and deformation. Therefore, no explicit constitutive form is assumed to describe the composite level response. Since damage is considered directly at the scale of the constituents, damage modes such as fiber cracking, transverse matrix cracking, and delamination are a natural consequence of the microscale response and explicitly evaluated within the multiscale model.

The requirement of evaluating a full microstructure model in CH typically leads to very high computational costs. In this study, we employ the eigendeformation-based reduced order homogenization method with symmetric coefficients (EHM) [17] to efficiently evaluate the response at the scale of the microstructure. The EHM model employs transformation field analysis [19] to reduce the computational complexity, by precomputing certain information (e.g., localization operators, influence functions, and concentration tensors) regarding the microstructure response through evaluating linear elastic unit cell problems before analyzing the macroscale structure.

The unit cell of the CFRP composite material within a single ply is shown in Fig. 25. The unit cell consists of the unidirectional fiber and the epoxy resin. Consider the partitioning of the unit cell domain into n parts within which the strains and damage are assumed to be spatially constant. Let $D^{(\alpha)}$ be a scalar damage variable indicating the state of damage within part α associated with the constitutive law in

Eq. 120.

$$\boldsymbol{\sigma}^{(\alpha)} = (1 - D^{(\alpha)})\mathbf{L}^{(\alpha)} : \boldsymbol{\varepsilon}^{(\alpha)} \tag{120}$$

$\boldsymbol{\varepsilon}^{(\alpha)}$ and $\boldsymbol{\sigma}^{(\alpha)}$ are the average strain and stress within part α, $\mathbf{L}^{(\alpha)}$ is the tensor of elastic moduli of the constituent material occupying part α, and ":" denotes the double inner product of two high order tensors. The evolution of $D^{(\alpha)}$ as a function of loading is modeled as:

$$D^{(\alpha)} = \Phi(\upsilon_{\max}^{(\alpha)}) \tag{121}$$

where $\upsilon_{\max}^{(\alpha)}$ is defined as:

$$\upsilon_{\max}^{(\alpha)}(t) = \max_{0 \leq \tau \leq t} \{\upsilon^{(\alpha)}(\tau)\} \tag{122}$$

in which $\upsilon^{(\alpha)}$ is the damage equivalent strain in part α:

$$\upsilon^{(\alpha)} = \sqrt{\frac{1}{2}\boldsymbol{\varepsilon}^{(\alpha)} : \mathbf{L}^{(\alpha)} : \boldsymbol{\varepsilon}^{(\alpha)}} \tag{123}$$

The phase damage evolution equation function is modeled using a two-parameter arctangent law:

$$\Phi(\upsilon^{(\alpha)}) = \frac{\arctan(a^{(\alpha)}\upsilon^{(\alpha)} - b^{(\alpha)}) + \arctan(b^{(\alpha)})}{\frac{\pi}{2} + \arctan(b^{(\alpha)})} \tag{124}$$

in which $a^{(\alpha)}$ and $b^{(\alpha)}$ are material parameters controlling the brittleness of failure and material strength, respectively. Figure 26 schematically illustrates the effect of parameters $a^{(\alpha)}$ and $b^{(\alpha)}$ on constituent material response. The macroscale stress of the overall fiber reinforced composite ply is expressed in terms of the macroscale strain, $\bar{\boldsymbol{\varepsilon}}$, the phase averaged damage induced inelastic strains (or eigenstrains), $\boldsymbol{\mu}^{(\alpha)}$, and the average phase damage, $D^{(\alpha)}$, as:

$$\bar{\boldsymbol{\sigma}} = \sum_{\Delta=1}^{n} \left\{ \left(1 - D^{(\Delta)}\right) \left(\mathbf{F}^{(\Delta)} : \bar{\boldsymbol{\varepsilon}} + \sum_{\alpha=1}^{n} \mathbf{H}^{(\Delta\alpha)} : \boldsymbol{\mu}^{(\alpha)} \right) \right\} \tag{125}$$

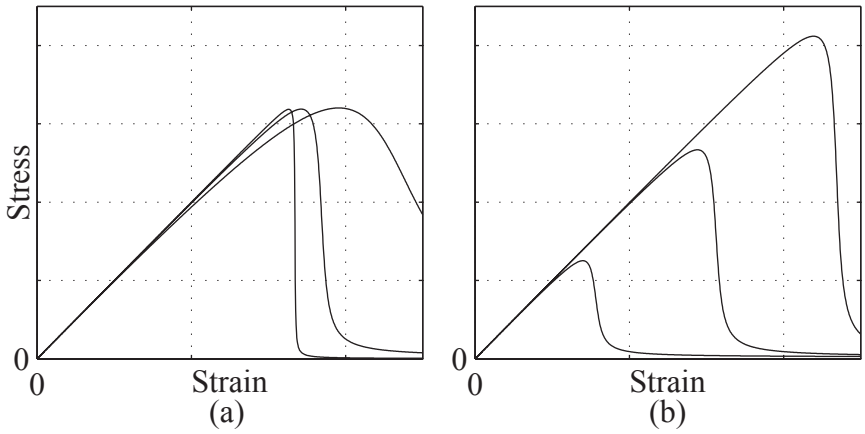

Figure 26: Stress-strain curves produced by the two parameter arctangent law: (a) $a^{(\alpha)}$ is varied while $b^{(\alpha)}$ is set to maintain constant failure stress (b) $b^{(\alpha)}$ was varied while maintaining constant $a^{(\alpha)}$.

The eigenstrains, $\boldsymbol{\mu}^{(\alpha)}$, are obtained by solving the following nonlinear system of equations:

$$\sum_{\Delta=1}^{n} \left\{ \left(1 - D^{(\Delta)}\right) \left(\mathbf{A}^{(\alpha\Delta)} : \bar{\boldsymbol{\varepsilon}} + \sum_{\beta=1}^{n} \mathbf{B}^{(\alpha\Delta\beta)} : \boldsymbol{\mu}^{(\beta)} \right) \right\} = \mathbf{0}, \quad \alpha = 1, ..., n \tag{126}$$

The coefficient tensors $\mathbf{A}^{(\alpha\Delta)}$, $\mathbf{B}^{(\alpha\Delta\beta)}$, $\mathbf{F}^{(\Delta)}$, and $\mathbf{H}^{(\Delta\alpha)}$ are expressed as:

$$\mathbf{A}^{(\eta\Delta)} = \int_{\Theta^{(\Delta)}} \mathbf{P}_{\mathsf{T}}^{(\eta)}(\mathbf{y}) : \mathbf{L}(\mathbf{y}) : (\mathbf{I} + \mathbf{G}(\mathbf{y}))\, d\mathbf{y} \tag{127}$$

$$\mathbf{B}^{(\eta\Delta\gamma)} = \int_{\Theta^{(\Delta)}} \mathbf{P}_{\mathsf{T}}^{(\eta)}(\mathbf{y}) : \mathbf{L}(\mathbf{y}) : \mathbf{P}^{(\gamma)}(\mathbf{y}) d\mathbf{y} \tag{128}$$

$$\mathbf{F}^{(\Delta)} = \frac{1}{|\Theta|} \int_{\Theta^{(\Delta)}} \mathbf{L}(\mathbf{y}) : (\mathbf{I} + \mathbf{G}(\mathbf{y}))\, d\mathbf{y} \tag{129}$$

$$\mathbf{H}^{(\Delta\gamma)} = \frac{1}{|\Theta|} \int_{\Theta^{(\Delta)}} \mathbf{L}(\mathbf{y}) : \mathbf{P}^{(\gamma)}(\mathbf{y}) d\mathbf{y} \tag{130}$$

$$\mathbf{P}^{(\Delta)}(\mathbf{y}) = \int_{\Theta^{(\Delta)}} \mathbf{g}_{\mathrm{ph}}(\mathbf{y}, \hat{\mathbf{y}}) d\hat{\mathbf{y}} \tag{131}$$

where Θ and $\Theta^{(\alpha)}$ are the domains of the RVE and the domain of part α, respectively, and $\mathbf{g}_{\mathrm{ph}}$ and $\mathbf{G}$ are the damage-induced and elastic polarization functions computed

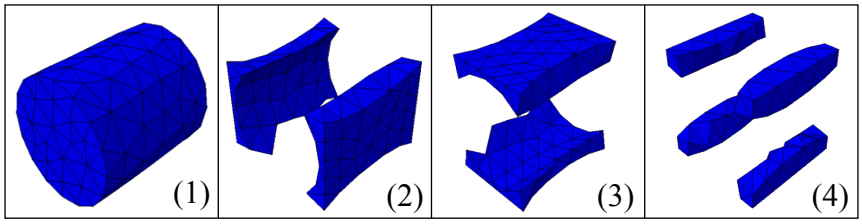

Figure 27: Partitioning of the unidirectionally reinforced composite unit cell.

from particular solutions of the unit cell problem. Subscript $\intercal$ denotes the transpose operator.

The partitioning of the unit cell employed in the present investigation is shown in Fig. 27. The partitioning is achieved to capture the three dominant failure modes of fiber fracture, transverse matrix cracking, and delamination. Parts 1, 2, and 3 in Fig. 27 capture the fiber fracture, transverse matrix cracking, and delamination, respectively. Part 4 is common to transverse matrix cracking and delamination. Introduction of this part is an effective way to treat intersecting failure paths. With this partitioning scheme, the microscale reduced order model incorporates the relevant damage modes.

3.3 Calibration of the Model Parameters

The elastic and damage properties of the constituent materials (i.e. fiber and matrix) were calibrated using experiments conducted on 0° and 90° unidirectionally stacked specimens, as well as experimental data available in the literature. In the model, a uniform distribution of fibers was assumed. The variability seen in the 0° calibration experiments is partially due to nonuniform fiber distribution, but as the primary concern in this work is tensile loading, it is assumed the effect of nonuniform fiber distribution is limited.

The 977-3 resin was taken to be isotropic with elastic modulus, $E^{(\mathrm{m})}$, and Poisson's ratio, $\nu^{(\mathrm{m})}$. The IM7 fiber was assumed to be transversely isotropic with elastic material properties denoted as $E_1^{(\mathrm{f})}$, $E_2^{(\mathrm{f})}$, $G_{12}^{(\mathrm{f})}$, $\nu_{12}^{(\mathrm{f})}$, and $\nu_{23}^{(\mathrm{f})}$. The Poisson's ratios of

the resin and fiber were set as $\nu^{(\mathrm{m})} = 0.35$ [31], $\nu_{12}^{(\mathrm{f})} = 0.32$, and $\nu_{23}^{(\mathrm{f})} = 0.20$ [12]. The constituents' elastic moduli, $E^{(\mathrm{m})}$, $E_1^{(\mathrm{f})}$, $E_2^{(\mathrm{f})}$, and $G_{12}^{(\mathrm{f})}$, were calibrated by minimizing the discrepancy between the composite elastic moduli of 0° and 90° specimens and the simulated elastic moduli of the homogenized composite. The constituent moduli were determined as $E^{(\mathrm{m})} = 3.55$ GPa, $E_1^{(\mathrm{f})} = 263$ GPa, $E_2^{(\mathrm{f})} = 13$ GPa, and $G_{12}^{(\mathrm{f})} = 27.5$ GPa which were in close agreement with previous investigations [12, 31].

The model parameters that define damage accumulation are $a^{(m)}$ and $b^{(m)}$ for the matrix and $a^{(f)}$, and $b^{(f)}$ for the fiber. The damage accumulation parameters are calibrated based on the set of experiments conducted on unidirectional 0° and 90° specimens. The constituent parameters are identified by minimizing the discrepancy between experimentally observed stress-strain response and numerical predictions of the multiscale model in the least squares sense. The calibrated and experimentally observed stress-strain response of the 0° and 90° specimens are displayed in Fig. 28. The 90° layup failure response was dominated by matrix failure whereas the 0° specimens fail by fiber fracture. The matrix and fiber damage accumulation properties were therefore separately calibrated based on 90° and 0° response, respectively. The matrix parameters were calibrated to the maximum observed strength among the experimental scatter since the failure originates at the largest flaw within the resin along the free edge. The fiber parameters were calibrated so that the model response equals the average experimental strength observed in the 0° specimens. The calibrated model parameters were $a^{(m)} = 0.002$, $b^{(m)} = 2.8$, $a^{(f)} = 0.05$, and $b^{(f)} = 340$.

3.4 Results and Discussion

Figure 29 shows the cumulative hit and cumulative energy as a function of applied stress amplitude measured in the AE testing at each load increment. Cumulative energy weighs each recorded hit based on the magnitude of the strain energy re-

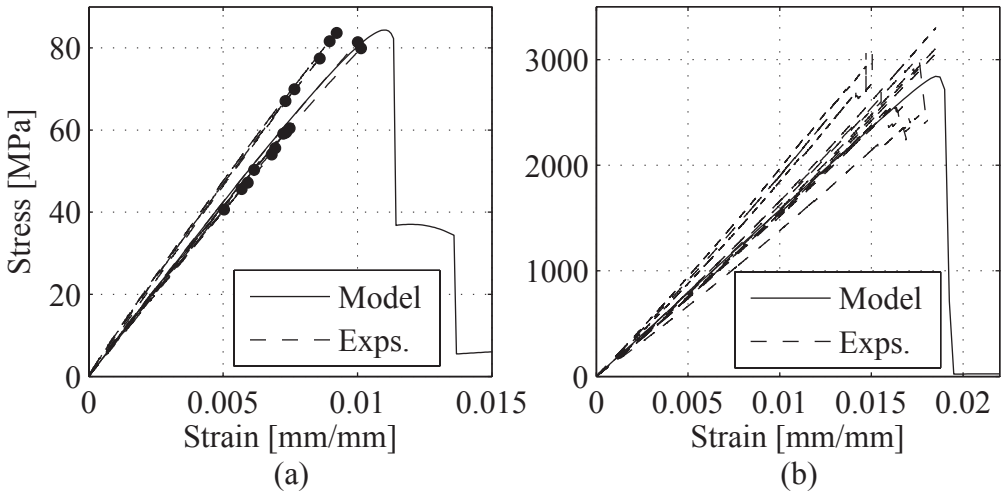

Figure 28: The stress-strain response of the calibrated model compared with experimental data: (a) specimens with 90° layup and (b) specimens with 0° layup.

leased during the damage event. When the specimen is unloaded and reloaded, the cumulative hits and energy remained relatively flat until the past maximum loading magnitude was exceeded indicating insignificant cyclic damage accumulation with an exception between the loadings of 620 MPa and 710 MPa. Damage growth initiated within the specimen indicated by an increase in the AE hits around 400 MPa. Damage within the specimen progressively accumulated with an increasing rate until the ultimate failure by fiber fracture in the 0° plies. In contrast with damage events at lower loading magnitudes, the acoustic emissions at failure were audible without any listening aides.

While AE testing provides qualitative information about the progressive nature of damage accumulation, the type and location of failure associated with an acoustic hit is less clear. The frequency and amplitude of recorded waves does provide some degree of information on the nature of the failure event such as fiber fracture and matrix damage [14], but more detailed information such as damage in individual plies is difficult to gather from AE measurements alone. X-ray radiography and X-ray computed tomography provides a nondestructive snapshot of the location and type of accumulated damage within the specimen. An X-ray radiograph of the pristine

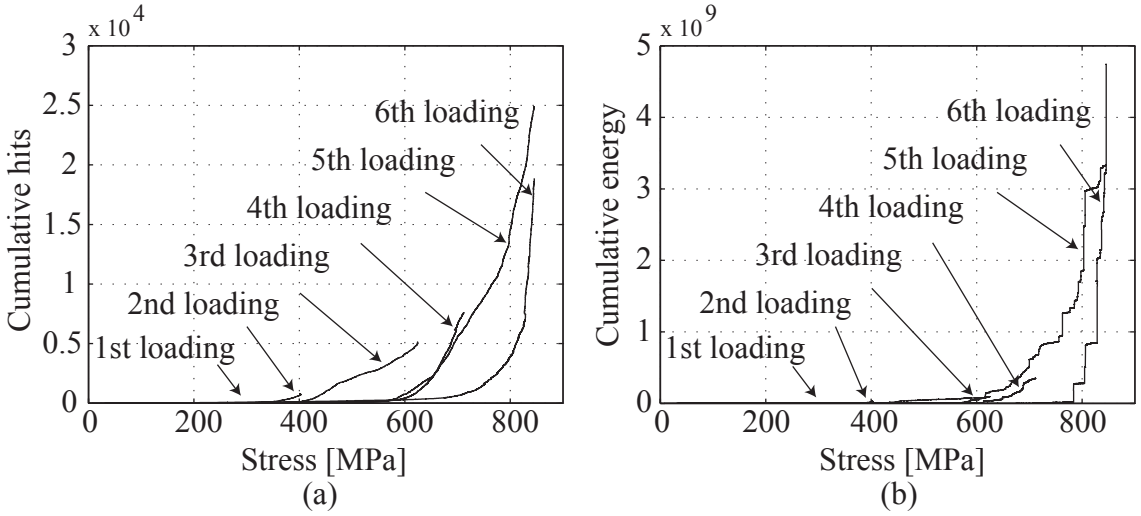

Figure 29: Loading stress versus (a) Cumulative AE hits and (b) Cumulative AE hit energy.

specimen was taken before loading and additional radiographs were taken after each loading (i.e. 300 MPa, 400 MPa, 620 MPa, 710 MPa, and 845 MPa). As illustrated in Figure 30, the cracks were visualized in light color in the X-ray radiographs due to the presence of the dye penetrant. Since the dye-penetrant could diffuse into the specimen through cracks originating at the specimen edges, only edge cracks could be visualized in the radiographs. No substantial cracks were visible for the first two loadings of 300 MPa and 400 MPa other than minor edge flaws. At a loading of 620 MPa, visible cracks appeared with orientations both perpendicular and $\pm 45^\circ$ to the length of the specimen. Between 620 MPa and 710 MPa, the number and length of cracks increased. Just before ultimate failure, a large delamination was clearly observed on the lower left side of the specimen (Fig. 30f). Smaller delaminations were clearly observed on both sides of the specimen.

X-ray computed tomography was employed to obtain a 3-D visualization of the extent and mechanisms of damage within the specimen. Figure 31 illustrates the 3-D tomographic image of the specimen at 710 MPa and 845 MPa. Extensive 45° and 90° cracks are evident as well as delaminations along the length of the specimen

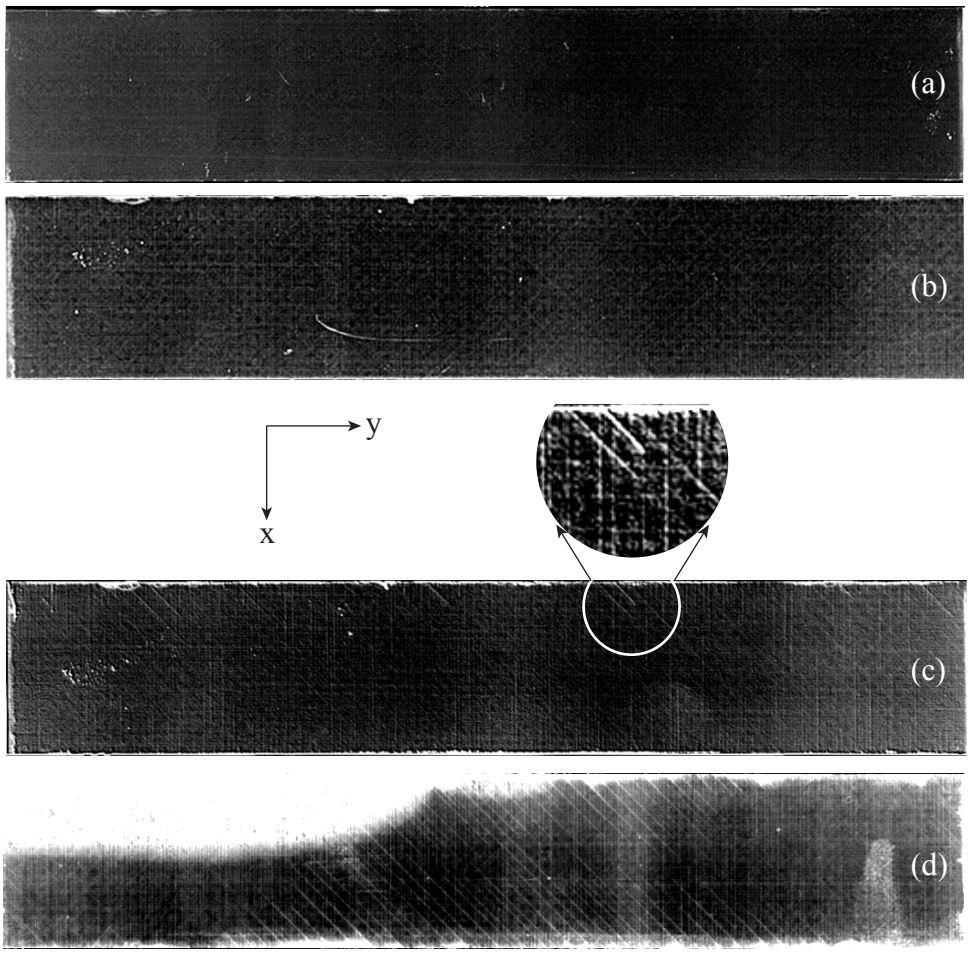

Figure 30: X-ray radiographs after loading to (a) 0 MPa (b) 400 MPa (c) 620 MPa (d) 845 MPa.

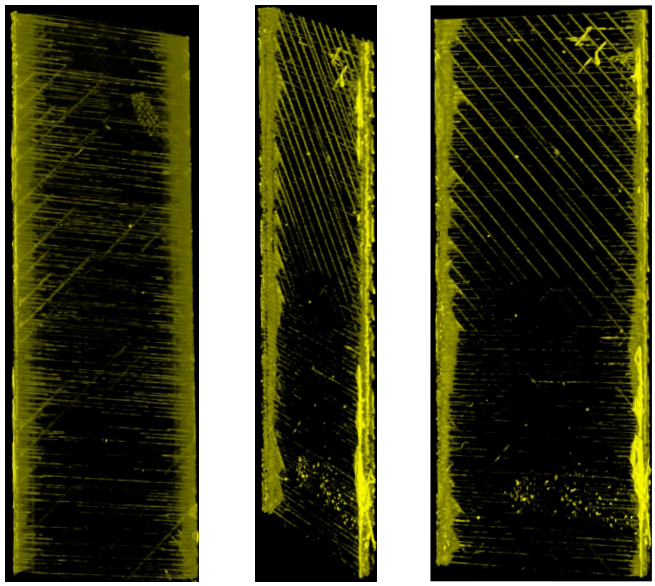

Figure 31: 3D tomographic images of damage in the specimen at a loading of (a) 720 MPa (b) 845 MPa (c) 845 MPa.

edge. Figure 32 illustrates the layer-by-layer damage profile observed using the X-ray computed tomography imaging technique. The 0° ply shown in Fig. 32a exhibited some degree of debonding in the fiber direction. In contrast to the radiography, the tomographic images are able to capture damage zones away from the edges that are not exposed to the dye-penetrant (Fig. 32a). The 90° ply at the center of the specimen developed extensive matrix cracking extending across the specimen's width along with rounded delaminations at the specimen edges. The 45° ply (the top ply of the specimen) shown in Fig. 32c developed extensive cracking across the specimen width along with triangular delaminations developing at the specimen edges. The large delamination shown in the radiograph of Fig. 30d cannot be seen in Fig. 32 since the tomographic images were taken over a smaller region of the specimen outside of the large-scale delamination.

The calibrated computational model described in Section 3.1 was employed to gain further understanding of the progressive damage accumulation in the composite specimen. The model provides a more complete picture of the damage response than

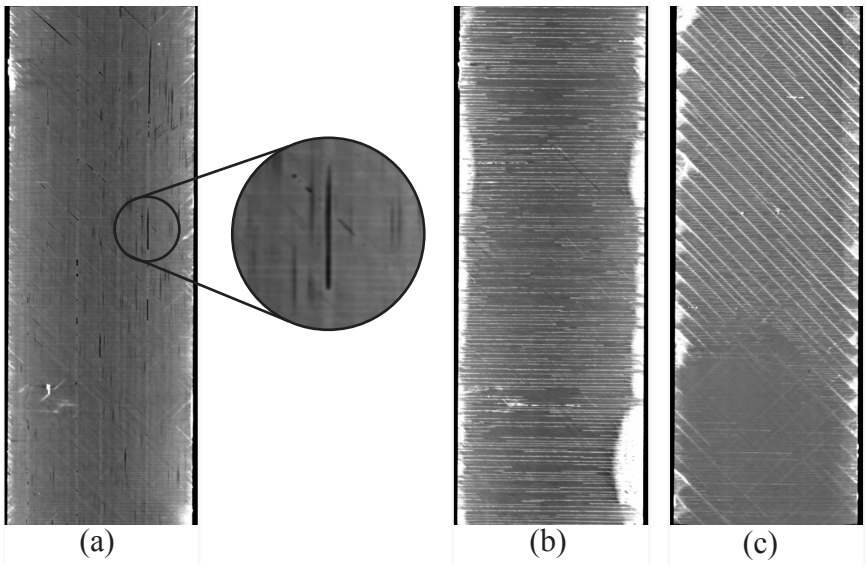

Figure 32: Computed tomography scans after loading to 845 MPa: (a) 0° ply (ply 11) (b) central 90° ply (c) top 45° ply.

the experiments alone. Figure 33a shows the stress-strain response of the virtual specimen under monotonic tensile loading. The predicted stress-strain response of the overall composite is displayed alongside the cumulative hit versus stress curve recorded by the AE system seen in Fig. 33b (the hits were summed over all loadings). The ultimate strength of the specimen predicted by the model was 855 MPa which was in excellent agreement with the experimentally observed strength of 872 MPa with a standard deviation of 30 MPa. The strength of the particular specimen probed by the NDI techniques was 846 MPa. The ultimate failure was caused by fiber fracture in the 0° plies in the numerical investigation.

The first major compliance change takes place at approximately 380 MPa when matrix cracking initiates in the ±45° plies. The compliance change in the virtual specimen coincides with the initiation of acoustic emission hits illustrated in Fig. 29, which occurs at approximately 400 MPa. The X-ray radiograph (Fig. 30b) taken at 400 MPa displays insignificant damage within the specimen confirming the damage initiation prediction of the model. The matrix cracks that initiated at the ±45° plies rapidly propagate across the length of the specimen. Figure 34 demonstrates the initi-

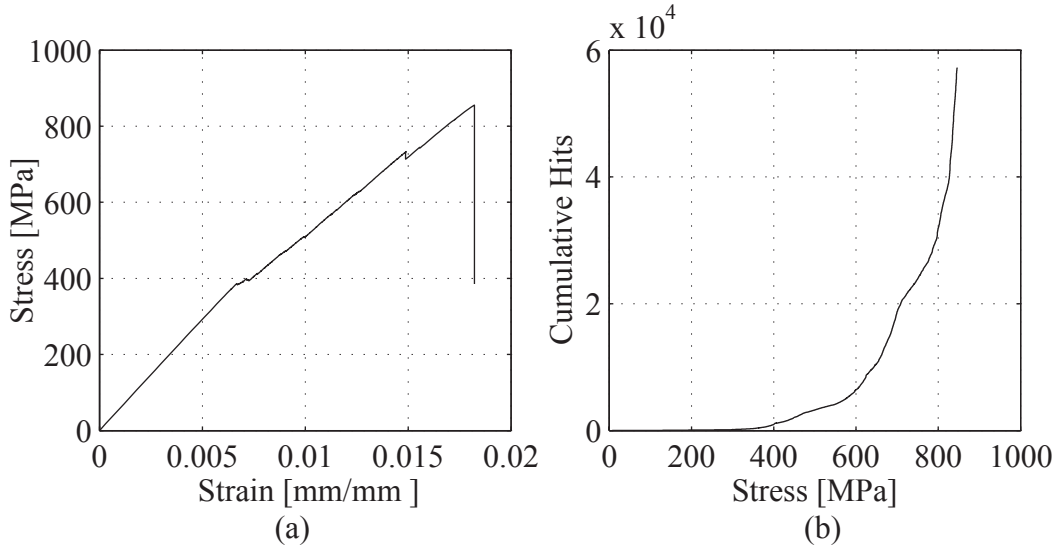

Figure 33: (a) Strain vs. stress for the virtual quasi-isotropic specimen (b) Stress vs. cumulative hits for the experimental specimen.

ation and propagation of matrix cracks in the top 45° ply. The progression of damage in the inner ±45° plies occurs less rapidly with cracking across the entire width of the specimen forming when the loading reached 475 MPa. The difference in speed of damage progression is due to the confinement of the inner ±45° plies compared to the top ply, which retards crack growth when compared to the top layer. Matrix cracking within the ±45° plies is followed by the initiation of damage within the 90° plies between 395 MPa (when damage first initiates in the 90° ply) and 409 MPa (when damage initiates in all 90° plies). Cracking extended across the entire width of the virtual specimen within the 90° plies between 472 MPa and 514 MPa. Figure 35 shows the progression of cracking in the 90° ply at the middle of the specimen. The 90° cracks clearly initiate from the specimen edges. Matrix cracking in the 0° plies remains negligible until the loading reaches close to the ultimate failure strength of the specimen. The predicted matrix cracking in the ±45° and 90° plies develops more rapidly in comparison to the matrix cracking in the experimental specimen as illustrated in Fig. 30b. This is partly attributed to the errors in the calibration of the matrix properties which was conducted based on 90° unidirectionally reinforced spec-

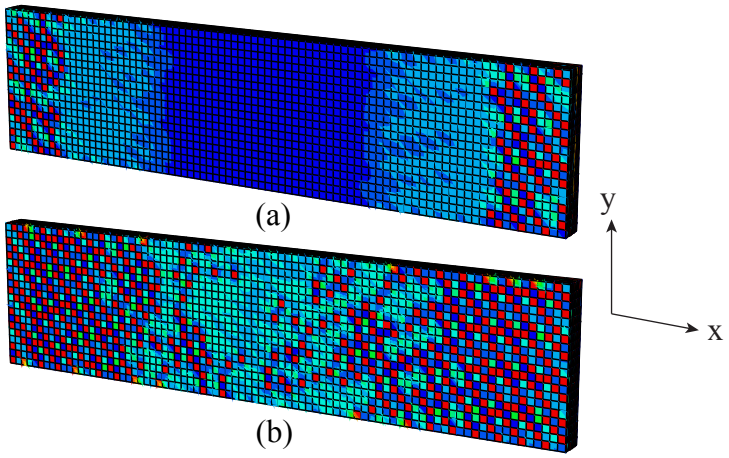

Figure 34: The damage contours corresponding to transverse matrix cracking at the top ply of the specimen (45°) at the applied stress level of (a) 388 MPa and (b) 394 MPa.

imen response. The failure in the calibration experiments initiated and propagated at the most critical flaw (i.e. the weakest link) within the resin. The statistics generated by the calibration experiments therefore capture the lower end of the strength and ductility spectrum of the resin material. Nevertheless, the overall matrix cracking pattern is in reasonable agreement with the experimental observations.

The initiation of delamination within the specimens occurs slightly after the initiation of matrix cracking. Small edge delaminations initiate between 385-416 MPa. The edge delaminations continue to grow slowly until the loading reaches close to the ultimate strength of the specimen. The rate of growth increases significantly as the magnitude of the loading approaches the ultimate strength. This observation is in close agreement with the high rate of increase in the AE hits at the later stages of loading to the progression of delaminations as shown in Fig. 33b. X-ray radiographs and tomographs confirm this observation. Figure 36 illustrates edge delamination propagation in the 7th ply around the ultimate strength of the specimen. The failure patterns predicted by the model shown in Figs. 34-36 are in good agreement with the patterns observed in the tomographic images in Fig. 32.

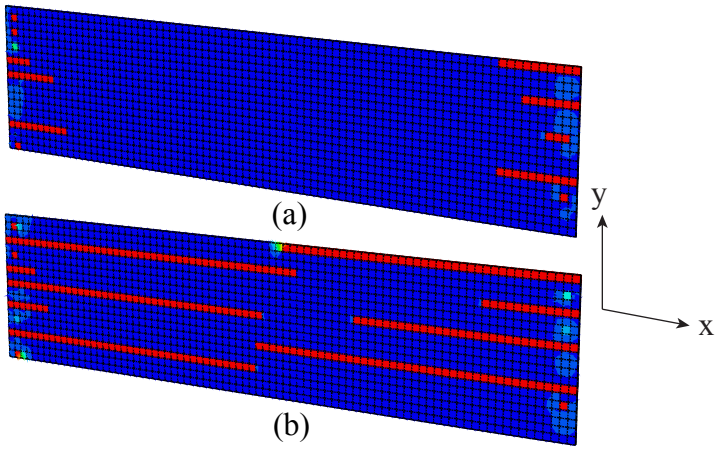

Figure 35: The damage contours corresponding to transverse matrix cracking at the center of the specimen (90° ply) at the applied stress level of (a) 412 MPa and (b) 470 MPa.

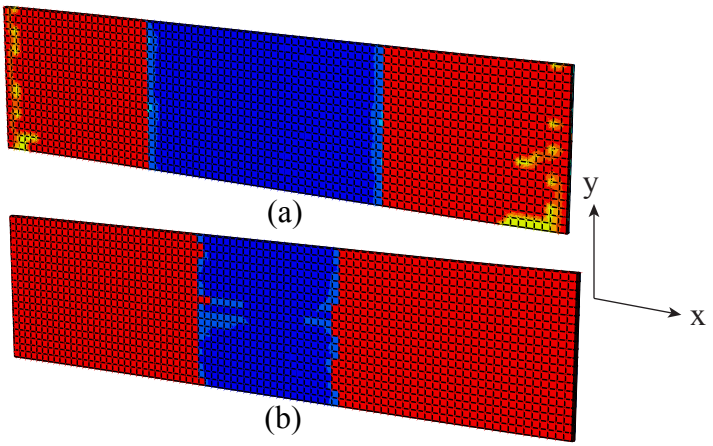

Figure 36: The damage contours corresponding to delamination near the middle of the specimen (−45° ply) at the applied stress level of (a) 730 MPa and (b) 855 MPa.

4 Investigation of CFRP Composites Under Fatigue Loadings

4.1 Computational Model

The geometry and finite element discretization considered in the macroscale specimen model are the same as the model for monotonic loads discussed in Sec. 3.1 and illustrated in Fig. 24. The length, width, and thickness of the numerical model were 6 mm, 25 mm, and 1 mm, respectively. The discretization of the model consisted of 26,560 trilinear hexahedral elements. Each ply was explicitly modeled along the thickness direction with 16 elements discretizing the thickness of the specimen layup. Only the top half of the specimen was discretized due to symmetry of the specimen. A small part of the specimen along the length (L=6 mm) was modeled to reduce the computational cost of the failure simulation. Periodic boundary conditions were imposed along the y-direction to eliminate spurious boundary effects due to submodeling. The numerical specimen was chosen long enough to avoid the interaction of damage effects between the top and bottom edges. The magnitude of the applied stress was taken to be the total constraint force required to maintain the specified average distance between the specimen ends divided by the cross sectional area of the specimen. The constraint force was oscillated to produce a fatigue loading with an r-ratio of 0.1 and a maximum stress amplitude of 143 MPa.

4.2 Multiscale Failure Modeling

In this study, we employ the multiple spatio-temporal scale methodology discussed in chapter 3 to evaluate the damage accumulation and response of the CFRP quasi-isotropic specimens. The unit cell of the CFRP composite material within a single ply is taken to be the same as in Sec. 3.2. Consider the partitioning of the unit cell domain into n parts within which the strains and damage are assumed to be spatially constant. Let $D^{(\alpha)}$ be a scalar damage variable indicating the state of damage within

part α associated with the constitutive law in Eq. 132.

$$\boldsymbol{\sigma}^{(\alpha)} = (1 - D^{(\alpha)})\mathbf{L}^{(\alpha)} : \boldsymbol{\varepsilon}^{(\alpha)} \tag{132}$$

$\boldsymbol{\varepsilon}^{(\alpha)}$ and $\boldsymbol{\sigma}^{(\alpha)}$ are the average strain and stress within part α, $\mathbf{L}^{(\alpha)}$ is the tensor of elastic moduli of the constituent material occupying part α, and ":" denotes the double inner product of two high order tensors. The evolution of $D^{(\alpha)}$ as a function of the fatigue loading is modeled as:

$$D^{(\alpha)} = g^p \frac{d\Phi(\upsilon^{(\alpha)})}{d\upsilon^{(\alpha)}} \langle \dot{\upsilon}^{(\alpha)} \rangle_+ \quad \text{where} \quad 0 \leq g = \frac{\Phi(\upsilon^{(\alpha)})}{D^{(\alpha)}} \leq 1 \tag{133}$$

where p is the cyclic sensitivity parameter, $\langle \cdot \rangle_+$ denotes the MacCauley brackets, Φ is the damage evolution law for monotonic loading, and $\upsilon^{(\alpha)}$ is the damage equivalent strain defined as

$$\upsilon^{(\alpha)} = \sqrt{\frac{1}{2}\boldsymbol{\varepsilon}^{(\alpha)} : \mathbf{L}^{(\alpha)} : \boldsymbol{\varepsilon}^{(\alpha)}} \tag{134}$$

The monotonic damage evolution law is taken to be the arctangent law used for the monotonically loaded specimens.

$$\Phi(\upsilon^{(\alpha)}) = \frac{\arctan(a^{(\alpha)}\upsilon^{(\alpha)} - b^{(\alpha)}) + \arctan(b^{(\alpha)})}{\frac{\pi}{2} + \arctan(b^{(\alpha)})} \tag{135}$$

The cyclic sensitivity parameter p is taken to be:

$$p^{(\alpha)} = c_0^{(\alpha)} + c_1^{(\alpha)}\upsilon_{\max}^{(\alpha)} + c_2^{(\alpha)}(\upsilon_{\max}^{(\alpha)})^2 \tag{136}$$

where $c_0^{(\alpha)}$, $c_1^{(\alpha)}$, and $c_2^{(\alpha)}$ are parameters controlling the fatigue response of the material. $\upsilon_{\max}^{(\alpha)}$ is defined as:

$$\upsilon_{\max}^{(\alpha)}(t) = \max_{0 \leq \tau \leq t} \{\upsilon^{(\alpha)}(\tau)\} \tag{137}$$

The expressions for the macroscale stress and the reduced order microscale prob-

lem are identical to those in Sec. 3.2 with the exception of the change in the damage evolution law to capture damage accumulation associated with fatigue loading. The adaptive macrochronological time stepping method in Sec. 4.1 of chapter 3 is utilized with a $\Delta D_{\max} = 1\%$. The partitioning of the unit cell employed in the present investigation is the same as that used for the monotonic loadings. With this partitioning, we can distinguish between transverse matrix cracking, delamination, and fiber failure.

4.3 Calibration of Model Parameters

The elastic parameters and the monotonic arctangent damage law parameters $a^{(\alpha)}$ and $b^{(\alpha)}$ were chosen to be equal to their values from the monotonic loading calibrations. The only remaining parameters are $c_0^{(\alpha)}$, $c_1^{(\alpha)}$, and $c_2^{(\alpha)}$ which control the fatigue response of the constituent materials. A least squares nonlinear optimization algorithm was used to minimize the discrepancy between the mean stress life curve in Fig. 37 and the calibrated model to determine the fatigue parameters for the matrix. The mean stress life curve was determined from tension tests with fatigue loadings on 90° unidirectional specimens. This is the same mean stress life curve from Sec. 6.2 of chapter 3 which should be referenced for further information regarding its determination. The fatigue parameters for the matrix parts were determined to be $c_0^{(\alpha)} = 8.033$, $c_1^{(\alpha)} = -6.232 \times 10^{-3}$, and $c_2^{(\alpha)} = -4.35 \times 10^{-6}$. The fiber was assumed to accumulate no damage due to fatigue loadings.

4.4 Results and Discussion

X-ray radiography provides a nondestructive image of the type and location damage accumulating in the specimen. X-ray radiographs of the quasi-isotropic specimens were taken after 1500, 37500, 72500, and 100000 loading cycles. Figures 38 and 39 show the radiographs from two of the three specimens. The two chosen specimens are representative of the third. As illustrated in Figs. 38-39, cracks were visualized in light

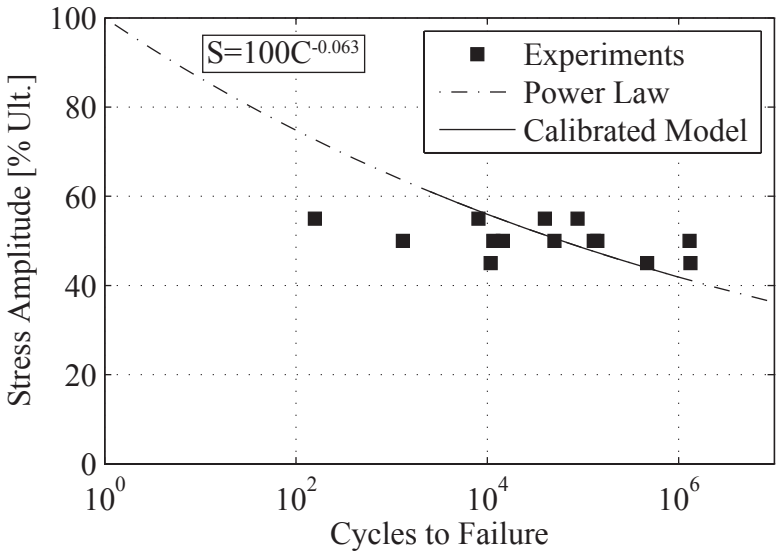

Figure 37: The calibrated fatigue response of unidirectional 90° specimens is compared with a statistical curve fit of the experimental determined fatigue response.

color in the radiographs due to the presence of dye penetrant applied to the specimen before the radiographs were taken. The dye-penetrant diffuses into the specimen through cracks originating at the specimen edges, and hence, only edge cracks are visualized in the radiographs. Few cracks were visible after the first 1500 loading cycles as indicated in Figs. 38a and 39a. It is possible that the cracks that are visible are manufacturing flaws as opposed to cracks that have developed during the first 1500 loading cycles. However, it is impossible to definitively draw this conclusion from the given data. After 37500 cycles, new cracks have developed at the edges of both $\pm 45°$ and 90° plies. By 72500 loading cycles, new cracks have initiated at the specimen edges along with lengthening of some of the cracks that were visible at 37500 cycles. With few exceptions the cracks do not extend very far across the specimen with almost no cracks reaching half of the specimens' width. At 100000 cycles, the length and density of the cracks are nearly the same as at 72500 cycles. No delaminations were seen in any of the specimens during the 100000 loading cycles.

The calibrated computational model described in Section 4.1 was used to gain

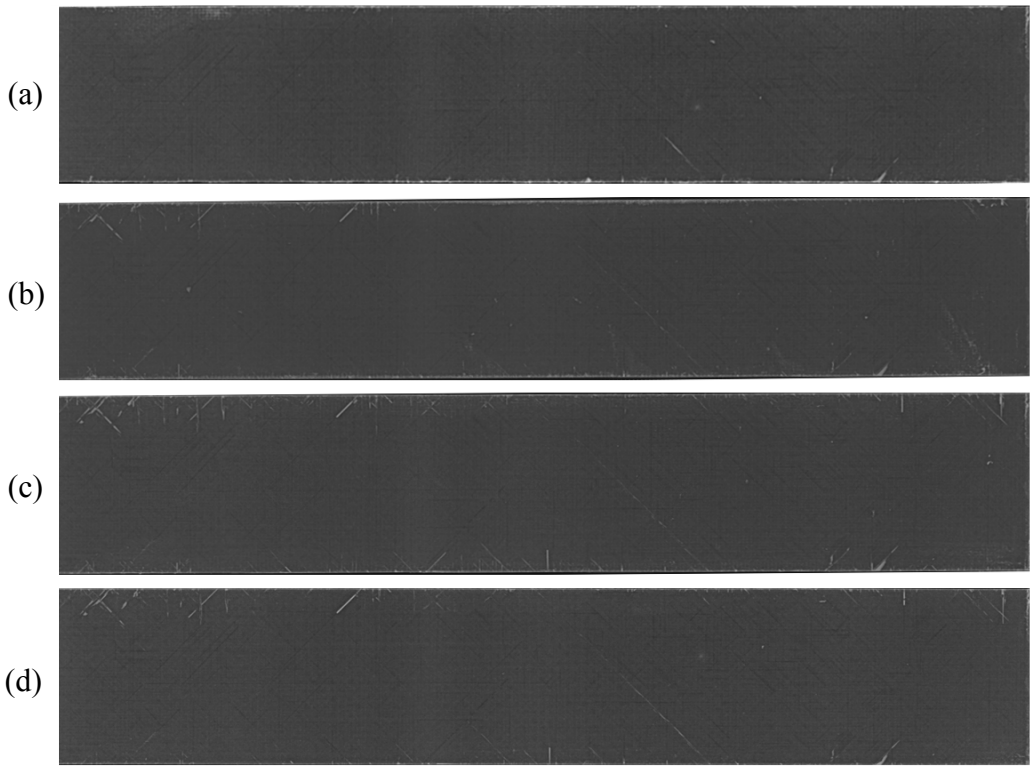

Figure 38: X-ray radiographs of a fatigue specimen after (a) 1500 loading cycles (b) 37500 loading cycles (c) 72500 loading cycles (d) 100000 loading cycles.

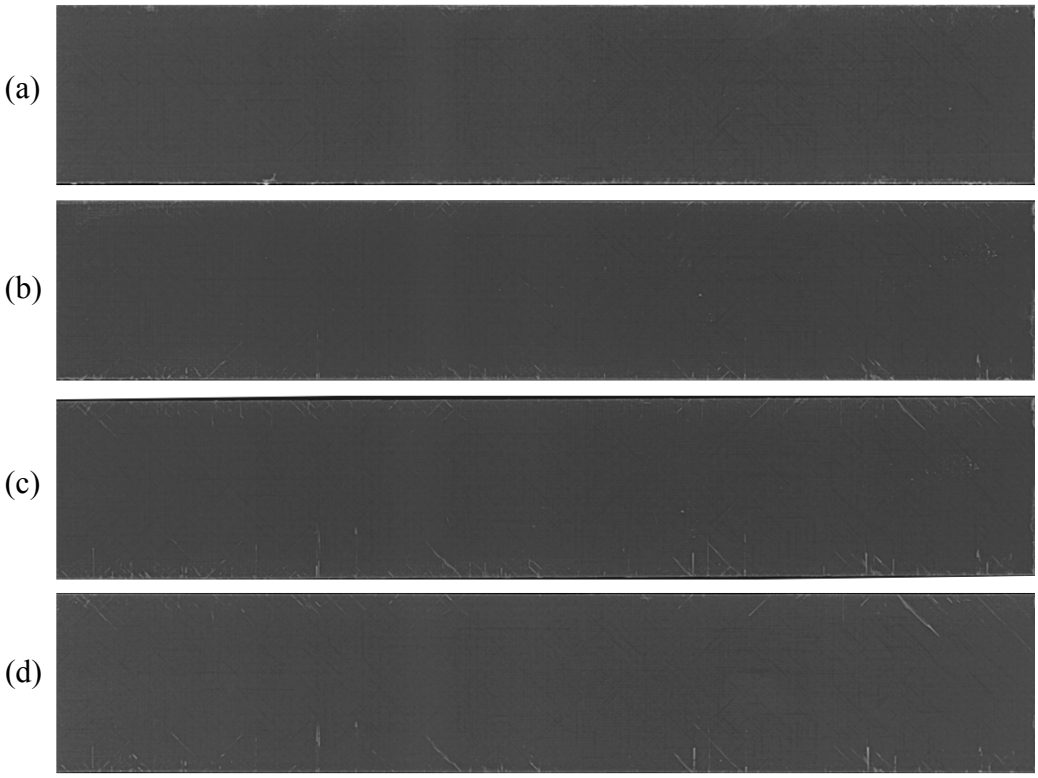

Figure 39: X-ray radiographs of another fatigue specimen after (a) 1500 loading cycles (b) 37500 loading cycles (c) 72500 loading cycles (d) 100000 loading cycles.

additional understanding of damage accumulation in CFRP quasi-isotropic specimens subjected to fatigue loadings. We define a transverse matrix crack to be present at a material point when the damage scalars $D^{(2)}$ and $D^{(4)}$, associated with parts 2 and 4 of the partitioned unit cell seen in Fig. 27, are greater than 0.99. A delamination is defined as when $D^{(3)}$ and $D^{(4)}$ are greater than 0.99. A fiber failure is indicated by $D^{(1)} > 0.99$. Figs. 40 and 41 show the value of the damage scalar $D^{(4)}$. Blue indicates a value close to zero and red indicates a value close to 1. At every material point within this simulation $D^{(4)}$ goes to one after $D^{(2)}$, and hence, in Figs. 40 and 41 red indicates the presence of transverse matrix cracking. Figure 40 shows transverse matrix cracking within the third ply from the top of the specimen which has an orientation of $-45°$, and Fig. 40 shows transverse matrix cracking within the seventh ply from the top of the specimen which also has an orientation of $-45°$. The cracking within these plies was representative of that in the fifth ply which has an orientation of $45°$. The top $45°$ ply showed less transverse matrix cracking than the internal plies. At 1500 loading cycles, there was no cracking within the specimen mirroring the behavior of the experimental specimens. After 37500 loading cycles, there was transverse matrix cracking within the seventh ply, but no cracking had initiated within any other ply. By 72500 cycles, transverse matrix cracking had initiated in all $\pm 45°$ plies with the exception of the top ply. At 100000 cycles, matrix cracking had initiated in all $\pm 45°$ plies. As in the radiographs, cracking was limited to the area in close proximity to the edges of the specimen even after 100000 loading cycles. At 100000 cycles, the simulation predicted no transverse matrix cracking in the $90°$ plies counter to the experimental observations. There was no delamination or fiber failure present in the simulation agreeing with the damage types seen in the X-ray radiographs.

The computational performance of the adaptive time stepping algorithm is shown in Fig. 42. The x-axis is the number of resolved loading cycles and the y-axis is the total number of loading cycles. As indicated in the figure, only 966 of the 100000

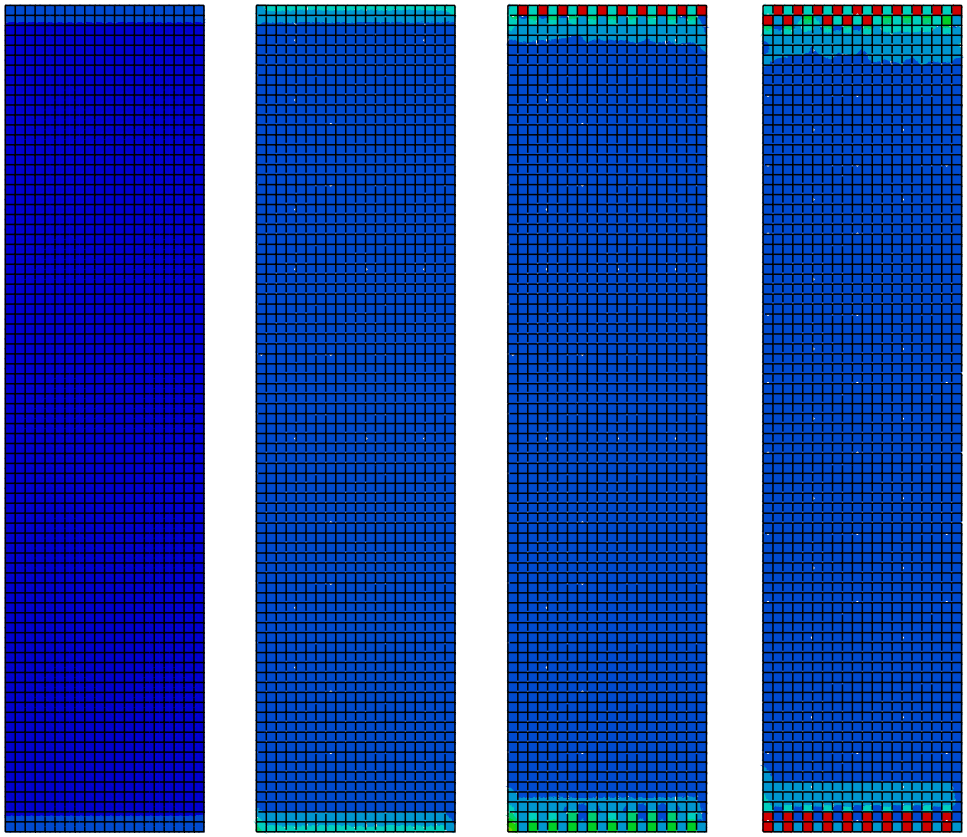

Figure 40: Transverse cracking in third ply ($-45°$) of the virtual specimen after (a) 1500 loading cycles (b) 37500 loading cycles (c) 72500 loading cycles (d) 100000 loading cycles.

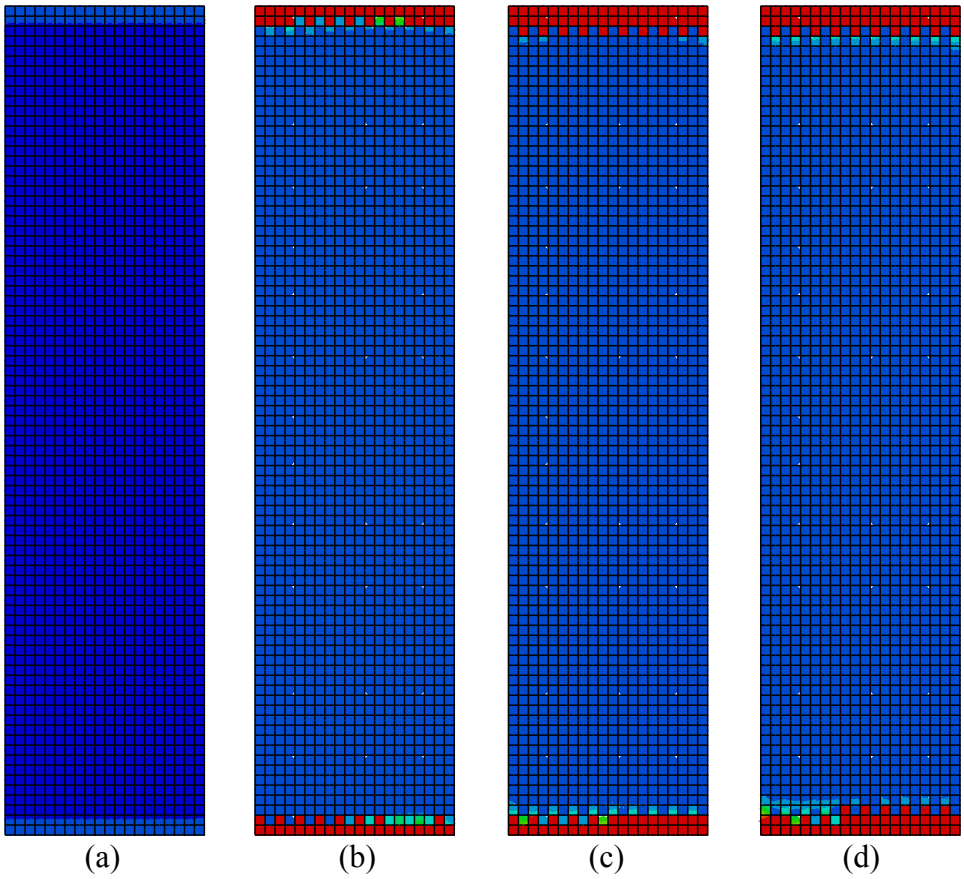

Figure 41: Transverse cracking in seventh ply ($-45°$) of the virtual specimen after (a) 1500 loading cycles (b) 37500 loading cycles (c) 72500 loading cycles (d) 100000 loading cycles.

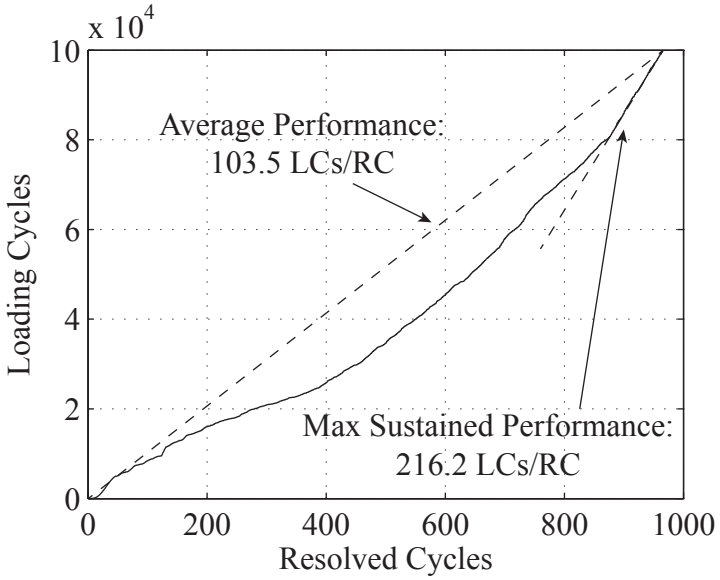

Figure 42: The performance of the adaptive macrochronological time stepping algorithm over 100000 loading cycles.

loading cycles were resolved. This leads to an average performance of 103.5 loading cycles per resolved cycle. This is a substantial savings in computational effort. For the final 20000 loading cycles (cycles 80000-100000), the performance of the algorithm increased to 216.2 loading cycles per resolved cycle. Without the adaptive time stepping algorithm, it would be required to resolve all 100000 cycles of a nonlinear multiscale finite element model with 26,560 elements. This would present a difficult computational barrier. The adaptive macrochonological time stepping algorithm allowed this simulation to be run on a single processor in three weeks.

CHAPTER 5

CONCLUSIONS AND FUTURE WORK

1 Conclusions

This dissertation proposed a multiscale framework for modeling failure in brittle composites subjected monotonic and fatigue loadings. Numerical testing verified the framework which was subsequently validated with experimental testing on carbon fiber reinforced polymers. More detailed conclusions regarding the multiscale framework are presented below.

Chapter 2 presented a reduced order multiscale computational methodology for failure analysis of heterogeneous materials. The proposed approach provides a novel model development strategy for creating reduced-order models capable of efficiently and accurately representing the failure modes within the microstructure without recourse to a detailed finite element model of the RVE. A two-order modeling approach was devised to eliminate spurious residual stresses upon failure allowing accurate stress-redistribution within a macroscopic component. The resulting reduced-order model possesses symmetry allowing efficient numerical evaluation of the microscale problem. The reduced order model was verified against direct numerical simulations. The proposed model captures the failure modes within the microstructure obtaining good accuracy.

In Chapter 3, a multiscale computational framework for prediction of failure in composite materials subjected to fatigue loadings was proposed. The reduced-order multiple spatial scale approach in combination with the multiple temporal scale time

stepping approach provides a high level of computational efficiency without a significant loss in accuracy. This is critical to determining fatigue life in large-scale composite structures. The experimentally calibrated model predicted the observed early life failure events in carbon-fiber reinforced polymer specimens.

In Chapter 4, a comprehensive experimental/computational investigation was undertaken to determine the nature of progressive damage accumulation in CFRP composites subjected to monotonic loading. Acoustic emission, X-ray radiography, and X-ray computed tomography inspection methods obtained a clear picture of the evolution of transverse matrix cracking and delamination within experimentally tested composite specimens as a function of the applied loading. The multiscale computational model was employed to gain further insight into the interaction and sequencing of damage mechanisms which were difficult to capture using any of the experimental techniques. The response mechanisms captured by the model predictions reasonably agreed with the experimental observations.

An experimental and computational investigation was also conducted on CFRP composites subjected to fatigue loadings in Chapter 4. X-ray radiography visualized the evolution of transverse matrix cracking within the tested specimens as a function of the number of loading cycles. A multiple spatial and temporal scale model was employed to simulate the accumulation of matrix damage within the CFRP specimens. Considering the high level of scatter in the fatigue calibration data, the response of the model showed reasonable qualitative agreement with the experimental study. The adaptive time stepping algorithm significantly reduced the effort required in simulating fatigue loadings.

2 Future Work

Within the multiple spatial scale framework, the challenge remains that the resulting homogenized macroscale problem shows spurious mesh dependency. The method-

ologies proposed in this dissertation eliminate mesh-dependency in the microscopic domain, but the homogenized macroscale problem remains local. For homogeneous materials, the computational mechanics literature has extensively investigated localization limiters that absolve spurious mesh dependency [8]. However, straightforward application of nonlocal damage theory is impractical due to the significant associated mesh refinement. Future research will investigate enrichment-based nonlocal formulations that eliminate mesh dependency without requiring a high level of mesh resolution in the macroscale domain.

An aircraft experiences a wide range of temperature conditions throughout its life and even within a single flight. The properties of a composite's constituent materials can vary significantly with temperature. These effects can be taken into account within the microscale domain where constitutive laws sensitive to temperature effects would replace the microscale constitutive laws presently utilized in the multiple spatial scale algorithm. Also, the multiple temporal scale methodology would need extension to account for temperature changes in macrochronological time.

The applicability of these methodologies should be extended from the specimen scale to the structural scale. Several possibilities show promise in this effort including the development of improved cycle stepping techniques that require fewer resolved cycles as evidenced by the improved cycle stepping criterion in Chapter 3, Section 5.1. Also, the extension of the proposed multiscale methods to shell elements would allow more efficient representation of structures whose thickness is small compared to its planar directions. In particular, this could be utilized for modeling laminated composite aircraft skin. Another path involves utilization of parallel computing since the reduced order microscale problems at the gauss points of the macroscale structure can be solved simultaneously within a single time increment.

Statistical variation is an important consideration when trying to model fatigue failure in composite materials. Both the constituent material parameters and the un-

derlying microstructural geometry vary from specimen to specimen and even from one part of a specimen to another. The scatter in the calibration experiments revealed this statistical variability especially for fatigue loadings. In the future, the multi-scale methodologies can be placed within a probabilistic framework that rigorously addresses and predicts the statistical variation.

Appendix A

PERIODIC MESHING OF REPRESENTATIVE VOLUME ELEMENTS

1 Introduction

In the EHM framework, a reduced order microscale problem determines the homogenized macroscale material response. The reduced order microscale problem is determined by solving for the elastic and inelastic influence functions seen in Eqs. 17 and 18. These influence functions are created from particular solutions of a fully resolved microscale problem. Periodic boundary conditions are applied to the representative volume element of the material when obtaining the particular solutions. The simplest method for applying periodic boundary conditions is to obtain a periodic mesh of the RVE. A mesh is periodic if for every node on one side of the RVE, there is a corresponding node on the other side. Periodic boundary conditions are enforced upon the RVE by requiring the response of both nodes to be equal. The creation of periodic meshes is not an automated process within the commercial finite element software Abaqus, hence complicated RVE geometries render the task of creating a periodic mesh difficult. A freely available tetrahedral mesher, Tetgen, is used alongside a new surface mesh creation program to allow easy periodic meshing of complicated RVE geometries. Section 2 presents the capabilities of Tetgen. Section 3 explains the creation of periodic surface meshes used for Tetgen input.

2 Tetgen

Tetgen is a tetrahedral meshing program created by the numerical mathematics and scientific computing group at the Weierstrass Institute for Applied Analysis and Stochastics in Berlin, Germany. Tetgen takes as its input a two dimensional surface mesh of a three dimensional solid region. The interior of the surface mesh is meshed with tetrahedrals using Delaunay tetrahedralization. In its default setting, Tetgen will change the connectivity and add additional nodes to the input surface mesh in order to produce a high quality mesh. However, if the surface mesh already has good quality, there is little need to add nodes or change connectivity to produce a high quality tetrahedral mesh. Tetgen has a setting that prevents any changes to the input surface mesh, so assuming a high quality periodic surface mesh of triangles can be produced of an RVE, Tetgen will produce the required periodic mesh of tetrahedrals.

3 Surface Mesh Creation Program

A surface mesh creation program (SMCP) was written to aid in the process of creating a periodic surface mesh of an RVE needed for Tetgen input. SMCP was written in Python due to the python scripting interface provided by Abaqus. SMCP provides the following functions pertaining to surface meshes.

Extract This function extracts surface meshes from Abaqus models according to the name given to a surface in Abaqus. This function allows the user of SMCP to draw the RVE geometry in Abaqus, mesh the geometry, extract pieces of the surface mesh created by Abaqus, and finally, build a periodic surface mesh out the of these pieces using other SMCP functions.

Move This function translates a surface mesh from one position to another. A translation vector must be provided to the function indicating the magnitude

and direction of the translation.

Copy This function makes a copy of a surface mesh.

Union This function allows two surface meshes to be combined into a single surface mesh. A distance, d, must be provided to this routine. If the distance from a node on one mesh to a node on the other mesh is less than d, then the two nodes are merged into a single node in the combined mesh.

Mirror This function reflects a surface mesh through a plane. It takes as its input a point in the plane along with a vector normal to the plane.

Output This function outputs a surface mesh to a Tetgen input file. After creating a periodic surface mesh, this function is called so that Tetgen can mesh the surface mesh's interior with tetrahedrals.

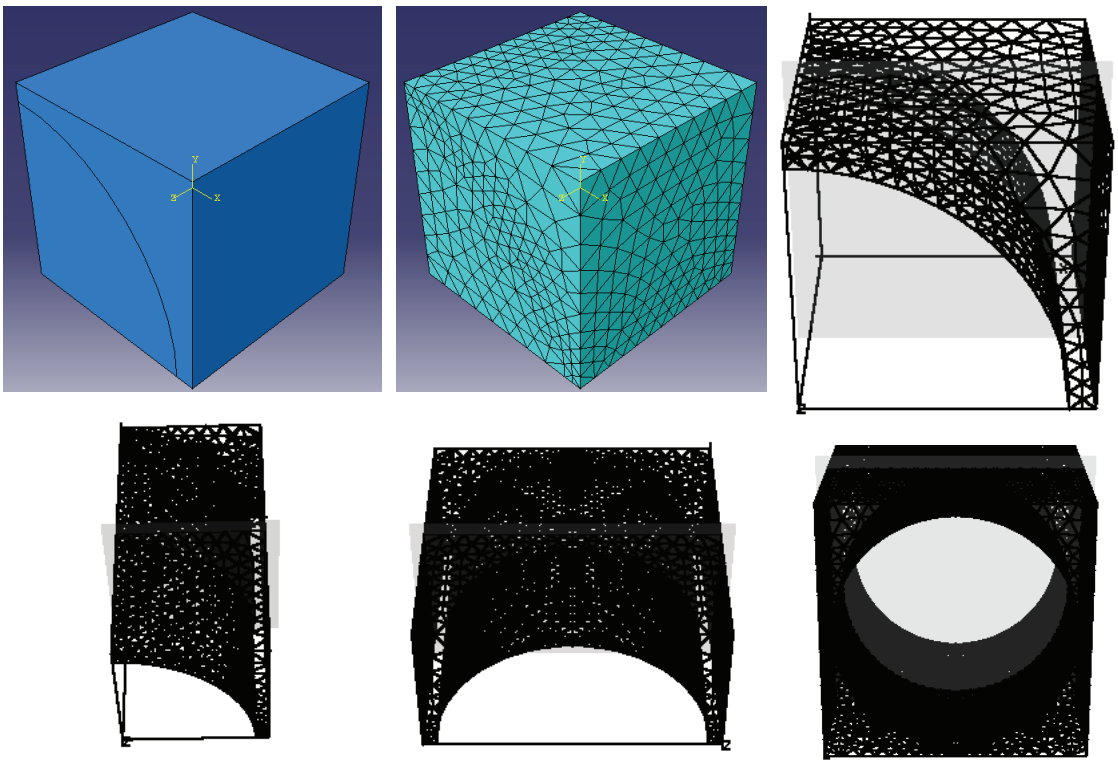

Figure 43: Creation of periodic surface mesh using SMCP

These functions can be easily combined to create a periodic surface mesh of an RVE. This is done by first drawing and meshing the RVE geometry in Abaqus. The Abaqus mesh will not be periodic, but this is of no concern. SMCP is then used to extract surface meshes from the Abaqus mesh. After extraction, these meshes will be modified and combined by the SMCP functions. It is usually a simple matter to obtain a periodic surface mesh. Figure 43 shows a graphical representation where surface mesh manipulations are used to obtain a periodic surface mesh of the matrix region of a simple RVE. The upper-right-frontal section of the RVE was drawn in Abaqus and meshed. The front, right, top, and interface surface meshes were then extracted and unionized. Next, the combined mesh was copied and mirrored three times to create a periodic surface mesh of the matrix region of the RVE. SMCP was also used to create a periodic mesh of the more complicated RVE seen in Figure 44.

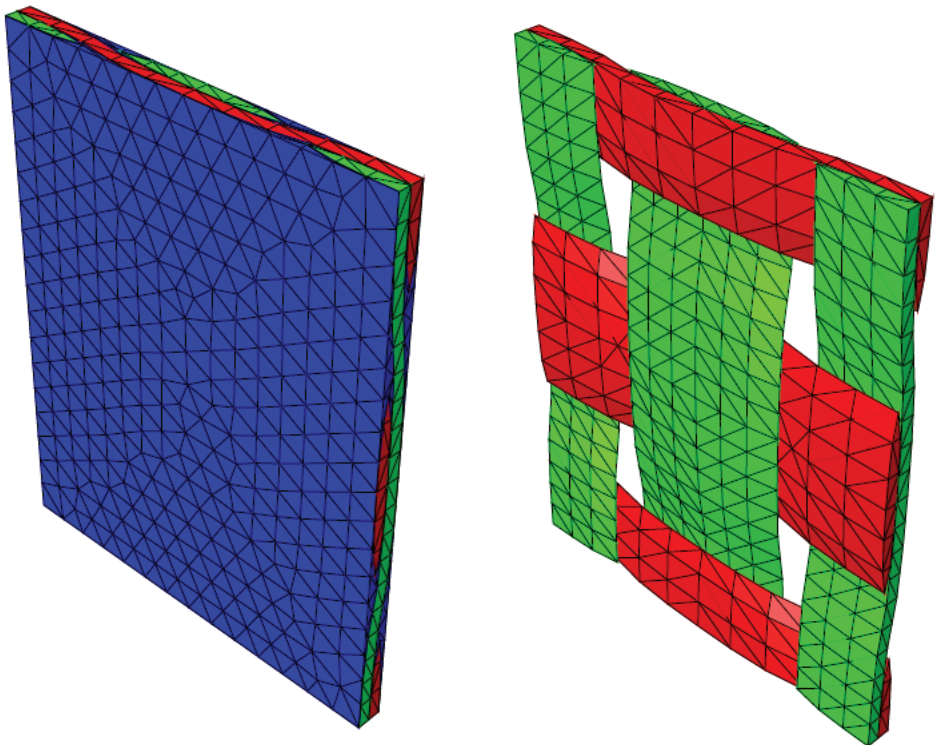

Figure 44: Periodic mesh of a RVE of a woven composite

BIBLIOGRAPHY

[1] J. Aboudi. A continuum theory for fiber-reinforced elastic-viscoplastic composites. *J. Eng. Sci.*, 20(55):605–621, 1982.

[2] N. V. Akshantala and R. Talreja. A micromechanics based model for predicting fatigue life of composite laminates. *Mat. Sci. Eng. A-Struct.*, 285:303–313, 2000.

[3] ASTM Standard D3039M-08. Standard test method for tensile properties of polymer matrix composite materials. *Annual Book of ASTM Standards*, 2008.

[4] ASTM Standard D3479M-96. Standard test method for tension-tension fatigue of polymer matrix composite materials. *Annual Book of ASTM Standards*, 2007.

[5] ASTM Standard D3518M-94. Standard test method for in-plane shear response of polymer matrix composite materials by tensile test of a +/-45° laminate. *Annual Book of ASTM Standards*, 2007.

[6] I. Babuska. Homogenization and application. mathematical and computational problems. In B. Hubbard, editor, *Numerical Solution of Partial Differential Equations - III, SYNSPADE*. Academic Press, 1975.

[7] Y. A. Bahei-El-Din, A. M. Rajendran, and M. A. Zikry. A micromechanical model for damage progression in woven composite systems. *Int. J. Solids Structures*, 41:2307–2330, 2004.

[8] Z. P. Bazant and M. Jirasek. Nonlocal integral formulations of plasticity and damage: Survey of progress. *J. Eng. Mech.*, 128:1119–1149, 2002.

[9] T. Belytschko, S. Loehnert, and J.-H. Song. Multiscale aggregating discontinuities: A method for circumventing loss of material stability. *Int. J. Numer. Meth. Engng.*, 73:869–894, 2008.

[10] A. Benssousan, J. L. Lions, and G. Papanicolaou. *Asymptotic Analysis for Periodic Structures*. North-Holland, Amsterdam, 1978.

[11] L. V. Berlyand and A. G. Kolpakov. Network approximation in the limit of small interparticle distance of the effective properties of a high-contrast random dispersed composite. *Arch. Rational Mech. Anal.*, 159:179–227, 2001.

[12] T. Breitzman, R. Lipton, and E. Iarve. Local field assessment inside multiscale composite architectures. *Multiscale Model. Simul.*, pages 937–962, 2007.

[13] R. L. Burden and J. D. Faires. *Numerical Analysis*. Brooks/Cole, Pacific Grove, CA, 6th edition, 1997.

[14] A. Bussiba, M. Kupiec, S. Ifergane, R. Piat, and T. Bohlke. Damage evolution and fracture events sequence in various composites by acoustic emission technique. *Compos. Sci. Technol.*, 68:1144–1155, 2008.

[15] J. L. Chaboche, S. Kruch, J. F. Maire, and T. Pottier. Towards a micromechanics based inelastic and damage modeling of composites. *Int. J. Plasticity*, 17:411–439, 2001.

[16] R. A. A. Couillard and P. Schwartz. Bending fatigue of carbon-fiber-reinforced epoxy composite strands. *Compos. Sci. Technol.*, 57:229–235, 1997.

[17] R. Crouch and C. Oskay. Symmetric mesomechanical model for failure analysis of heterogeneous materials. *Int. J. Multiscale Com.*, 8:447–461, 2010.

[18] J. P. Dunkers, D. P. Sanders, D. L. Hunston, M. J. Everett, and W. H. Green. Comparison of optical coherence tomography, x-ray computed tomography, and confocal microscopy results from an impact damaged epoxy/e-glass composite. *J. Adhes.*, 78:129–154, 2002.

[19] G. J. Dvorak. Transformation field analysis of inelastic composite materials. *Proc. R. Soc. Lond. A*, 437:311–327, 1992.

[20] F. Feyel and J.-L. Chaboche. Fe2 multiscale approach for modelling the elastoviscoplastic behavior of long fiber sic/ti composite materials. *Comput. Meth. Appl. Mech. Engng.*, 183:309–330, 2000.

[21] J. Fish and R. Fan. Mathematical homogenization of nonperiodic heterogeneous media subjected to large deformation transient loading. *Int. J. Numer. Meth. Engng.*, 76:1044–1064, 2008.

[22] J. Fish and C. Oskay. A nonlocal multiscale fatigue model. *Mech. Adv. Materials and Structures*, 12:485–500, 2005.

[23] J. Fish, K. L. Shek, M. Pandheeradi, and M. S. Shephard. Computational plasticity for composite structures based on mathematical homogenization: Theory and practice. *Comput. Meth. Appl. Mech. Engng.*, 148:53–73, 1997.

[24] J. Fish and Q. Yu. Computational mechanics of fatigue and life predictions for composite materials and structures. *Comput. Meth. Appl. Mech. Engng.*, 191:4827–4849, 2002.

[25] J. Fish, Q. Yu, and K. L. Shek. Computational damage mechanics for composite materials based on mathematical homogenization. *Int. J. Numer. Meth. Engng.*, 45:1657–1679, 1999.

[26] E. Gal, Z. Yuan, W. Wu, and J. Fish. A multiscale design system for fatigue life prediction. *Int. J. Multiscale Com.*, 5:435–446, 2007.

[27] M. G. D. Geers, V. Kouznetsova, and W. A. M. Brekelmans. Gradient-enhanced computational homogenization for the micro-macro scale transition. *J. Phys. IV*, 11:145–152, 2001.

[28] S. Ghosh, K. Lee, and P. Raghavan. A multi-level computational model for multi-scale damage analysis in composite and porous materials. *Int. J. Solids Structures*, 38:2335–2385, 2001.

[29] S. Ghosh and S. Moorthy. Elastic-plastic analysis of arbitrary heterogeneous materials with the voronoi cell finite element method. *Comput. Methods Appl. Mech. Engng.*, 121(1-4):373–409, 1995.

[30] M. Gosz, B. Moran, and J. D. Achenbach. Matrix cracking in transversely loaded fiber composites with compliant interphases. In AMD-150/AD-32, editor, *Damage Mechanics in Composites*. ASME, 1992.

[31] J. R. Gregory and S. M. Spearing. Constituent and composite quasi-static and fatigue fracture experiments. *Compos. Part. A-Appl. S.*, 36:665–674, 2005.

[32] J. M. Guedes and N. Kikuchi. Preprocessing and postprocessing for materials based on the homogenization method with adaptive finite element methods. *Comput. Meth. Appl. Mech. Engng.*, 83:143–198, 1990.

[33] B. Harris. *Fatigue in Composites*. CRC Press, 2003.

[34] C. J. Hellier. *Handbook of Nondestructive Evaluation*. McGraw-Hill, 2001.

[35] J. D. Hochhalter, D. J. Littlewood, R. J. Christ, Jr., M. G. Veilleux, J. E. Bozek, A. R. Ingraffea, and A. M. Maniatty. A geometric approach to modeling microstructurally small fatigue crack formation: II. physically based modeling of microstructure-dependent slip localization and actuation of the crack nucleation mechanism in AA 7075-T651. *Model. Simul. Mater. Sc.*, 18, 2010.

[36] D. B. P. Huynh and T. Belytschko. The extended finite element method for fracture in composite materials. *Int. J. Numer. Meth. Eng.*, 77:214–239, 2009.

[37] R. Krueger and T. K. O'Brien. A shell/3d modeling technique for the analysis of delaminated composite laminates. *Compos. Part. A-Appl. S.*, 32:25–44, 2001.

[38] S. Li, M. D. Thouless, A. M. Waas, J. A. Schroeder, and P. D. Zavattieri. Use of mode-I cohesive-zone models to describe the fracture of an adhesively-bonded polymer-matrix composite. *Compos. Sci. Technol.*, 65:281–293, 2005.

[39] J. C. Michel and P. Suquet. Computational analysis of nonlinear composite structures using the nonuniform transformation field analysis. *Comput. Meth. Appl. Mech. Engng*, 193:5477–5502, 2004.

[40] H. Moulinec and P. Suquet. A fast numerical method for computing the linear and nonlinear properties of composites. *C. R. Acad. Sc. Paris II*, 318:1417–1423, 1994.

[41] V. P. Nguyen, O. Lloberas-Valls, M. Stroeven, and L. J. Sluys. Computational homogenization for multiscale crack modeling implementational and computational aspects. *Int. J. Numer. Meth. Eng.*, 2011.

[42] J. Nocedal and S. Wright. *Numerical Optimization*. Springer Verlag, 2nd edition, 2006.

[43] J. T. Oden and S. Prudhomme. Goal-oriented error estimation and adaptivity for the finite element method. *Computers & Mathematics With Applications*, 41:735–756, 2001.

[44] C. Oskay and J. Fish. Fatigue life prediction using 2-scale temporal asymptotic homogenization. *Int. J. Numer. Meth. Engng.*, 61:329–359, 2004.

[45] C. Oskay and J. Fish. Multiscale modeling of fatigue for ductile materials. *Int. J. Comp. Multiscale Engng.*, 2, 2004.

[46] C. Oskay and J. Fish. Eigendeformation-based reduced order homogenization for failure analysis of heterogeneous materials. *Comp. Meth. Appl. Mech. Engng.*, 196(7):1216–1243, 2007.

[47] C. Oskay and J. Fish. On calibration and validation of eigendeformation-based multiscale models for failure analysis of heterogeneous systems. *Comp. Mech.*, 42:181–195, 2008.

[48] M. H. J. W. Paas, P. J. G. Schreurs, and W. A. M. Brekelmans. A continuum approach to brittle and fatigue damage: Theory and numerical procedures. *Int. J. Solids. Struct.*, 30:579–599, 1993.

[49] A. A. Pollock. Loading and stress in acoustic emission testing. *Mater. Eval.*, 2004.

[50] P. Raghavan and S. Ghosh. A continuum damage mechanics model for unidirectional composites undergoing interfacial debonding. *Mech. Mater.*, 37:955–979, 2005.

[51] K. L. Reifsnider. The critical element model - a modeling philosophy. *Eng. Fract. Mech.*, 25:739–749, 1986.

[52] E. Sanchez-Palencia. *Non-homogeneous media and vibration theory*, volume 127 of *Lecture notes in physics*. Springer-Verlag, Berlin, 1980.

[53] M. M. Shokrieh and L. B. Lessard. Progressive fatigue damage modeling of composite materials, part I: Modeling. *J. Compos. Mater.*, 34:1056–1080, 2000.

[54] F. Sket, R. Seltzer, J. M. Molina-Aldareguia, C. Gonzalez, and J. Llorca. Determination of damage micromechanisms and fracture resistance of glass fiber/epoxy cross-ply laminate by means of x-ray computed microtomography. *Compos. Sci. Technol.*, 2012.

[55] S. M. Spearing, P. W. R. Beaumont, and M. F. Ashby. Fatigue damage mechanics of composite-materials .2. a damage growth-model. *Compos. Sci. Technol.*, 44:169–177, 1992.

[56] W.W. Stinchcomb. Nondestructive evaluation of damage accumulation processes in composite laminates. *Compos. Sci. Technol.*, 25:103–118, 1986.

[57] S. R. Stock. X-ray microtomography of materials. *Int. Mater. Rev.*, 44:141–164, 1999.

[58] P. M. Suquet. Elements of homogenization for inelastic solid mechanics. In E. Sanchez-Palencia and A. Zaoui, editors, *Homogenization Techniques for Composite Media*. Springer-Verlag, 1987.

[59] D.D. Symons. Characterisation of indentation damage in 0/90 layup t300/914 cfrp. *Compos. Sci. Technol.*, 60:391–401, 2000.

[60] V. Tamuzs, K. Dzelzitis, and K. Reifsnider. Prediction of the cyclic durability of woven composite laminates. *Compos. Sci. Technol.*, 68:2717–2721, 2008.

[61] K. T. Tan, N. Watanabe, and Y. Iwahori. X-ray radiography and micro-computed tomography examination of damage characteristics in stitched composites subjected to impact loading. *Compos. Part B-Eng.*, 42:874–884, 2011.

[62] K. Terada and N. Kikuchi. Nonlinear homogenization method for practical applications. In S. Ghosh and M. Ostoja-Starzewski, editors, *Computational Methods in Micromechanics*, volume AMD-212/MD-62, pages 1–16. ASME, 1995.

[63] O. van der Sluis, P.J.G. Schreurs, W. A. M.AM Brekelmans, and H.E.H. Meijer. Overall behaviour of heterogeneous elastoviscoplastic materials: effect of microstructural modelling. *Mech. Mater.*, 32:449–462, 2000.

[64] J. Yvonnet and Q. C. He. The reduced model multiscale method (R3M) for the non-linear homogenization of hyperelastic media at finite strains. *J. Comput. Physics*, 223:341–368, 2007.